

UCSF

UC San Francisco Electronic Theses and Dissertations

Title

Investigating the mechanism of action of ribosome-targeting antibiotics and resistance by RNA methylation

Permalink

<https://escholarship.org/uc/item/9t110989>

Author

Tsai, Mary Kaitlyn

Publication Date

2021

Peer reviewed|Thesis/dissertation

Investigating the mechanism of action of ribosome-targeting antibiotics and resistance by RNA methylation

by
Mary Kaitlyn Tsai

DISSERTATION

Submitted in partial satisfaction of the requirements for degree of
DOCTOR OF PHILOSOPHY

in

Chemistry and Chemical Biology

in the

GRADUATE DIVISION

of the

UNIVERSITY OF CALIFORNIA, SAN FRANCISCO

Approved:

DocuSigned by:

Danica Galonic Fujimori

Danica Galonic Fujimori

82967A5AE18B4D6...

Chair

DocuSigned by:

Michelle Arkin

Michelle Arkin

DocuSigned by:

John Gross

John Gross

C876331A93DC4B1...

Committee Members

Dedication

I would like to dedicate this work to my loving parents, who have always encouraged me to walk through this life with a thirst for knowledge and, first and foremost, kindness towards others.

Acknowledgements

This would not have been possible without the support of my mentors, family, and friends. First and foremost, I would like to thank my thesis advisor, Danica Galonić Fujimori for her attentive, enthusiastic, and constant mentorship over the past five and a half years. Completing a Ph.D. is a challenging task, let alone during a global pandemic, and I am forever grateful for your support and encouragement through it all. Thank you for recruiting me to UCSF over a critical phone call and igniting my passion for chemical biology. Thank you for creating an environment that gives your students the courage to embrace the unknown and inspires them to learn gracefully with each failure. And thank you for teaching me, through your actions every day, that scientific excellence and compassion for others go hand in hand.

I would like to thank every individual in the Fujimori lab, both past and present, for being amazing scientists and friends. To Vanja Stojković, who had immense patience with my lack of bench skills at the beginning of graduate school, thank you for teaching me every basic skill in biochemistry, for laying the foundation for every project I worked on, and reminding me to not stress the small stuff. To Fatima Ugur and Letitia Sarah, my desk buddies, thank you for the laughs, scientific conversations, and candid feedback. To James Longbotham and Meng Yao Zhang, my same-aisle bench mate and across-the-way bench mate, thank you for the venting sessions and random chats about nonsense. Jordan, thank you for being a great teammate on RNA projects; I have learned so much from you.

To my thesis committee members, John Gross and Michelle Arkin, thank you for your thoughtful advice and constant support over the years. So many small conversations that took place during my thesis committee meetings hugely impacted the way I thought about my science. Thank

you, Jaime Fraser, Stephen Floor, Adam Frost, Ian Seiple, and Alex Myaskinov, for your contributions and guidance on various aspects of the ribosome projects. Thank you to my CCB cohort; it has been an honor to work alongside such an amazing group of people. I am constantly blown away by the caliber of work produced by you all, and I know the future of chemical biology research is bright. A special thank you to Beatrice Ary, Taylor Arhar, Gracie Gordon, and Lisa Kirkemo for being a tribe of women I can always rely on during tough times.

Thank you to my family in North Carolina, who have been a huge source of emotional support over the years. A special thank you to my little sister EmmaLi, for the many many phone calls where we commiserate over our struggles with perfectionism and lift each other up. And of course, a very special thank you to my partner Andy Chiu, who is a constant source of light in my life and inspires me every day to live for the small moments.

Contributions

Several chapters of this thesis contain material from previously published work. They do not represent the final published forms and have been edited slightly.

Chapter 2 of this dissertation is a reprint of a previous publication:

Tsai, K., Stojković, V., Noda-Garcia, L., Young, I.D., Myasnikov, A.G., Kleinman, J., Palla, A., Floor S.N., Frost, A., Fraser, J.S., Tawfik, D.S., Fujimori, D.G. Directed evolution of the rRNA methylating enzyme Cfr reveals molecular basis of antibiotic resistance. *bioRxiv* (2021) doi:10.1101/2021.03.12.435202.

K.T. conceived the research, designed and performed experiments, analyzed data, and wrote the manuscript. V.S. performed directed evolution, assisted in data interpretation, model refinement, and manuscript editing. L.N.-G. performed evolution experiments and manuscript editing. I.D.Y. and A.G.M. performed structural analysis. J.K. and A.P. assisted in data acquisition and analysis. S.N.F., A.F., J.S.F., and D.S.T. assisted in experimental design, data interpretation, and manuscript editing. D.G.F. conceived and supervised the research, assisted in data interpretation, and edited the manuscript.

Chapter 3 of this dissertation is a reprint of a previous publication:

Tsai, K.*, Stojković, V.*, Lee, J.D.*, Young, I.D., Szal, T., Klepacki, D., Vazquez-Laslop, N., Mankin, A.S., Fraser, J.S., Fujimori, D.G. Structural basis for context-specific inhibition of translation by oxazolidinone antibiotics. *bioRxiv* (2021) doi: 10.1101/2021.08.10.455846. *Authors contributed equally to this work.

K.T. performed antibiotic resistance experiments and structural analysis, assisted with model refinement, prepared figures, and wrote the manuscript. V.S. prepared ribosome samples, performed model refinement, and edited the manuscript. D.J.L. performed cryo-EM analysis, performed model refinement, prepared figures, and edited the manuscript. I.D.Y. performed structural analysis, performed model refinement, prepared figures, and edited the manuscript. T.S. and D.K. performed *in vitro* translation experiments. N.V.-L. and A.S.M. provided data interpretation and edited the manuscript. J.S.F. and D.G.F. conceived and supervised the research, assisted in data interpretation, and edited the manuscript.

“Failure is the Mother of Success”

-Random fortune cookie

**Investigating the mechanism of action of ribosome-targeting antibiotics
and resistance by RNA methylation**

by

Mary Kaitlyn Tsai

Abstract

The ribosome is a major antibiotics target, and a large portion of transitional inhibitors bind to the peptidyl transferase center (PTC). A prominent form of resistance to PTC-targeting antibiotics, including the “last-resort” antibiotic linezolid, is through acquisition the Cfr enzyme which methylates a PTC nucleotide to form m⁸A2503. To understand how bacteria adapt Cfr resistance under antibiotic pressure, we performed directed evolution of Cfr to generate variants with increased resistance via improved Cfr expression and stability. We used an evolved variant with superior methylation activity to obtain a 2.2 Å cryo-EM structure of a Cfr-methylated ribosome, revealing that the Cfr modification directly interferes with antibiotic binding. Building upon this knowledge, we sought to understand how the linezolid derivative, radezolid, overcomes Cfr-mediated resistance. We discover that linezolid and radezolid have similar context-specificity, preferring to inhibit translation with a penultimate alanine in the nascent peptide. The obtained high resolution cryo-EM structures of the antibiotic-stalled ribosome complexes reveal that the alanine forms a favorable interaction with the antibiotic. Furthermore, the determined structure of radezolid in complex with a Cfr-modified ribosome indicates that radezolid overcomes resistance through interactions with its extra ring system, forcing m⁸A2503 to tilt away to accommodate the antibiotic. Together, these findings identify strategies that boost Cfr methylation and provide molecular rationale for how second-generation antibiotics can overcome Cfr-mediated resistance.

Table of Contents

Chapter 1	1
Linezolid inhibition of bacterial ribosomes and emerging mechanisms of resistance	1
The bacterial ribosome is a major antibiotic target	2
Context-specific inhibition by the oxazolidinone antibiotic linezolid	3
Mechanisms of resistance to linezolid.....	4
<i>Mutations in ribosomal RNA and proteins</i>	4
<i>Ribosome protection by ABC-F proteins</i>	6
<i>Altered modification state of A2503</i>	6
Second-generation oxazolidinone antibiotics	9
Scope of thesis work.....	10
References	14
Chapter 2	23
Directed evolution of the rRNA methylating enzyme Cfr reveals the molecular basis of antibiotic resistance	23
Abstract.....	24
Introduction	24
Results	26
<i>Evolved Cfr variants confer enhanced antibiotic resistance</i>	26
<i>Variants exhibit increased rRNA methylation and Cfr protein levels</i>	28
<i>Promoter and second position mutations drive Cfr resistance</i>	29
<i>Mutations impact Cfr translation and degradation</i>	30

<i>Evolved Cfr enables understanding of the structural basis of resistance</i>	32
Discussion.....	35
Materials and Methods	40
References	76
Chapter 3	88
Structural basis for context-specific inhibition of translation by oxazolidinone antibiotics	88
Abstract.....	89
Introduction	89
Results	91
<i>LZD and RZD have similar ribosome stalling behavior</i>	91
<i>Formation of stalled ribosome complexes and cryo-EM analysis</i>	92
<i>The penultimate alanine facilitates antibiotic binding</i>	93
<i>Additional interactions with rRNA nucleotides</i>	96
<i>Cfr methylation perturbs the stalled ribosome complex</i>	98
Discussion.....	101
Materials and Methods	102
References	129

List of Figures

Figure 1.1 Antibiotics that target the PTC	11
Figure 1.2 Mechanisms of resistance to linezolid	12
Figure 1.3 Second generation oxazolidinone antibiotics	13
Figure 2.1 Evolved variants of Cfr confer increased antibiotic resistance	56
Figure 2.2 Cfr variants cause increased methylation of 23S rRNA at A2503.....	57
Figure 2.3 In vitro characterization of Cfr ^{WT} and Cfr ^{V4}	58
Figure 2.4 N-terminally truncated Cfr products do not contribute to resistance	59
Figure 2.5 Mutations to the second amino acid and promoter are the largest contributors to Cfr expression and resistance	60
Figure 2.6 Cfr modification of the ribosome does not impact expression of Cfr ^{N2K}	61
Figure 2.7 Directed evolution mutations impact Cfr translation and degradation	62
Figure 2.8 Impact of 2nd codon identity on Cfr expression	63
Figure 2.9 Near-stoichiometric ribosome methylation by Cfr ^{V7} enables structural determination of Cfr-mediated resistance to antibiotics.....	64
Figure 2.10 Cross-validation of methylations on C8 of A2503 and 2'O of C2498 from the cryoEM density map.....	65
Figure 2.11 Cfr-mediated resistance to PhLOPS _A antibiotics	66
Figure 2.12 Cfr-mediated resistance to hygromycin A, A201A, and 16-membered macrolide antibiotics	67
Figure 2.13 RNA secondary structure predictions near the Cfr start codon.....	68
Figure 2.14 Start codon selection as a proposed mechanism of Cfr inducibility	69
Figure 2.15 Protein sequence alignment of Cfr and Cfr homologues	70

Figure 3.1 Radezolid induces ribosome stalling with alanine in the penultimate position	110
Figure 3.2 Cryo-EM structures of linezolid and radezolid-stalled ribosome complexes	111
Figure 3.3 Processing workflow, classification tree, FSC curves, and local resolution estimation for each map.....	112
Figure 3.4 Oxazolidinone-induced ribosome stalling at the Phe5 codon	113
Figure 3.5 Nascent peptide with penultimate alanine stabilizes oxazolidinone binding	114
Figure 3.6 Overview of linezolid and radezolid binding modes within the PTC	115
Figure 3.7 Oxazolidinone binding modes in antibiotic-only and stalled complexes.....	116
Figure 3.8 Linezolid and chloramphenicol use the same interaction for context-specificity	117
Figure 3.9 In silico analysis of residues at the penultimate position	118
Figure 3.10 Additional stabilization via interactions with rRNA nucleotides.....	119
Figure 3.11 Stabilization of PTC nucleotides.....	120
Figure 3.12 Steric occlusion of A-site tRNA binding by oxazolidinone antibiotics	121
Figure 3.13 LZD and RZD activity against Cfr-modified ribosomes	122
Figure 3.14 The Cfr modification reduces radezolid-dependent ribosome stalling	123
Figure 3.15 Density for the nascent chain in RZD-stalled ribosome complexes	124
Figure 3.16 A2062 conformations in the RZD-bound ribosome structures	125
Figure 3.17 Model for oxazolidinone context-specific inhibition of translation.....	126

List of Tables

Table 2.1 Cfr sequence variants from the first enrichment round	71
Table 2.2 Cfr sequence variants from the second enrichment round	72
Table 2.3 Promoter architecture of Cfr variants from final enrichment rounds with promoter alterations	73
Table 2.4 Cryo-EM data collection, refinement, and validation statistics.....	74
Table 2.5 Primer sequences used in this study	75
Table 3.1 Cryo-EM data collection and statistics	127
Table 3.2 Primer sequences used in this study	128

Chapter 1

Linezolid inhibition of bacterial ribosomes and emerging mechanisms of resistance

Introduction

The bacterial ribosome is a major antibiotic target

The ribosome is a large macromolecular machine that carries out the essential process of protein synthesis. Ribosomes are largely made up of ribosomal RNA (rRNA) and contain two subunits that work together to translate messenger RNA (mRNA) into protein. In bacteria, the large 50S ribosomal subunit, which includes 23S rRNA and 5S rRNA, and the small 30S ribosomal subunit, which contains 16S rRNA, join to form the full 70S ribosome (**Figure 1.1**). Due to its critical role in cell viability, protein synthesis is a highly regulated process and requires the participation of several translation factors to coordinate movement through the four steps of the translation cycle: initiation, elongation, termination, and recycling¹.

Translation is initiated by binding of the 30S subunit to mRNA at the start codon and recruitment, with the help of initiation factors, of the initiator tRNA (typically fMet-tRNA_{ifMet})². Joining of the 50S ribosomal subunit forms the 70S initiation complex, which is primed to begin the elongation step of protein synthesis. The 70S initiation complex contains three primary tRNA binding sites: the A-site for aminoacylated tRNAs (aa-tRNA), the P-site for peptidyl-tRNAs carrying the growing peptide chain, and the E-site for deacylated tRNAs to exit the ribosome. At the beginning of elongation, the initiator tRNA is bound to the P-site. Then, tRNAs charged with amino acids (aa-tRNAs) in complex with elongation factor Tu (EF-Tu) and GTP are delivered to the open ribosomal A-site. Upon formation of the correct base pair between the mRNA and aa-tRNA, GTP is hydrolyzed to release the aa-tRNA into the A-site and allow accommodation of the tRNA into the peptidyl transferase center (PTC). Peptide bond formation, arguably the most critical step of translation, then occurs between the peptidyl-tRNA and the aa-tRNA by transferring

the growing peptide chain from the P-site to the A-site. To vacate the A-site and facilitate the next round of elongation, elongation factor G (EF-G) catalyzes translocation of tRNAs to the adjacent sites, namely A- to P-site and P- to E-site. The elongation process continues iteratively to extend the polypeptide chain one amino acid at a time until a stop codon reaches the A-site. The stop codon is recognized by release factors which hydrolyze the peptidyl-tRNA to release the newly synthesized protein. The translation components are then disassembled through ribosome recycling to enable another round of protein synthesis.

Approximately half of clinically used antibiotics target the bacterial ribosome³. Ribosome-targeting antibiotics typically bind to key functional regions to disrupt almost every process of protein synthesis⁴. Of these key functional regions, a disproportionately large number of clinically important antibiotics bind to the 50S ribosomal subunit within the PTC⁵ (**Figure 1.1**) Existing crystal and cryo-EM structures of ribosome complexes reveal that these antibiotics occupy overlapping but non-identical binding sites within the PTC. Several PTC-targeting antibiotics bind within the A-site and capitalize on interactions with the splayed-out bases of U2504, A2451, and C2452 within 23S rRNA that make up what is known as the A-site cleft⁶. These antibiotics include chloramphenicol, oxazolidinones (linezolid), lincosamides (clindamycin), puromycin, and sparsomycin. Other PTC antibiotics bind to the P-site (blasticidin S) or both A- and P-sites (pleuromutilins and streptogramin A antibiotics).

Context-specific inhibition by the oxazolidinone antibiotic linezolid

Despite their overlapping binding sites, structural and biochemical data indicate that PTC antibiotics have nuanced mechanisms by which they inhibit protein synthesis. Of particular interest in this regard is the oxazolidinone antibiotic linezolid, the first member of the oxazolidinone class

which was FDA-approved in 2000 (Zyvox)⁷ (**Figure 1.1**). Due to its ability to treat drug-resistant gram-positive pathogens such as methicillin-resistant *Staphylococcus aureus* (MRSA), vancomycin-resistant *Enterococcus faecium*, and penicillin-resistant *Streptococcus pneumoniae*⁸, it has been categorized by the World Health Organization as a reserve group antibiotic that should only be used as a treatment of “last resort”⁹.

Linezolid consists of a core oxazolidinone ring substituted with fluorinated aryl group at position 3 and an acetamide moiety at position 5 (C5-group), in addition to a morpholine ring (**Figure 1.1**). Original crosslinking studies identified the PTC as the linezolid binding site¹⁰. Structures of linezolid-ribosome complexes revealed that the aryl ring is wedged within the A-site cleft and the oxazolidinone ring engages in an off-set π -stacking interaction with U2504^{11–13}. Due to its binding mode, it was hypothesized that the morpholine ring of linezolid would sterically prevent accommodation of incoming aa-tRNAs and thus inhibit all peptidyl transfer events. However, more recent studies have demonstrated that linezolid does not, in fact, inhibit peptide bond formation indiscriminately but only when the amino acid alanine occupies the penultimate position within the nascent chain^{14,15}. The PTC-targeting antibiotic chloramphenicol, which also binds to the A-site cleft via its aryl ring, has a context-specific mode of action similar to that of linezolid^{14–16} (**Figure 1.1**).

Mechanisms of resistance to linezolid

Mutations in ribosomal RNA and proteins

Since the binding site of linezolid is composed entirely of rRNA, a common form of resistance involves mutation of one or more copies of the rRNA (*rrn*) genes. While mutation of rRNA nucleotides that directly interact with linezolid can confer resistance, the most prominent

mutation observed in clinical isolates (G2576U, *E. coli* numbering) is located distal from the antibiotic binding site (7.9 Å, **Figure 1.2**)¹⁷. The G2576U mutation confers strong resistance in both *Staphylococcus* and *Enterococcus* species, with a clear correlation between the number of G2576 alleles mutated, levels of linezolid resistance, and severity of fitness defect¹⁸. Despite the evidence of fitness cost associated with this 23S rRNA mutation, highly linezolid-resistant strains containing the G2576U mutation in all *rrn* alleles have been recovered clinically^{19–21}. The exact mechanism by which G2576U alters the linezolid binding site within the PTC remains elusive, but it has been postulated that G2576U alters the conformation of nucleotides G2505 and U2506 which interact directly with the antibiotic¹³ (**Figure 1.2**).

Single point mutations, deletions, or insertions in rProteins L3, L4, and L22 have also been documented as mechanisms of resistance²² (**Figure 1.2**). The structure of a linezolid-resistant MRSA ribosome containing a single residue deletion in L3 (Δ S145, >20 Å away) revealed compaction of the linezolid binding site through rearrangement of G2505 via long-range allosteric effects²³. Molecular rationale for how alteration of the other distal rProteins (L4>14 Å away, L22>19 Å away) cause resistance to linezolid has not been elucidated. Notably, the extended regions of L4 and L22 line the exit tunnel and reach towards the PTC to form the nascent peptide constriction site. Since the mechanism of linezolid inhibition is dependent on components of the nascent chain, it is possible that changes to L4 and L22 result in an altered nascent peptide path to indirectly cause resistance. Notably, mutations within L4 and L22 have also been implicated in disrupting macrolide-dependent ribosome stalling²⁴.

Ribosome protection by ABC-F proteins

Resistance genes *optrA* and *poxtA* encode ABC-F ribosome protection proteins and, due to their association with mobile genetic elements, are a transferrable form of resistance to linezolid (**Figure 1.2**). The *optrA* gene was first identified in a patient-derived *E. faecalis* isolate in 2015²⁵ and confers resistance to linezolid, phenicols, and to a lesser extent the second generation oxazolidinone tedizolid. The *poxtA* gene was detected in a patient-derived MRSA isolate in 2018 and confers low-level resistance to phenicols, oxazolidinones, and tetracyclines²⁶. A recent cryo-EM structure of PoxTA in complex with an *E. faecalis* ribosome reveals that the antibiotic resistance domain of PoxTA extends towards the PTC to shift the register of the nascent peptide by one amino acid²⁷. As a result, positioning of the penultimate alanine, which is important for the activity of linezolid and chloramphenicol, is perturbed and thus confers resistance.

Altered modification state of A2503

Post-transcriptional rRNA modifications are distributed within functional regions of the ribosome²⁸. Of the 35 naturally occurring rRNA modifications, only one involves methylation of an *sp*²-hybridized carbon atom. Adenosine at position 2503 (A2503) within 23S rRNA is a highly conserved nucleotide. The rRNA-modifying enzyme RlmN methylates the C2 atom of A2503, resulting in m²A2503 (*E. coli* numbering throughout)^{29,30} (**Figure 1.2b**). RlmN is a member of the Radical-SAM enzyme superfamily and employs a complex radical mechanism to install this unusual modification mark^{31,32}. While RlmN appears highly conserved throughout all bacteria³³, the purpose of this energetically costly m²A modification remains cryptic. Nucleotide A2503 is located within the PTC and neighbors nucleotides in the nascent peptide exit tunnel. Inactivation of RlmN results in minor growth defects²⁹ and ribosomes lacking the A2053 modification exhibit

disrupted macrolide-dependent induction of the *ermC* gene³⁴. RlmN inactivation also increases stop codon readthrough in a LacZ reporter system³⁰. Together, these results suggest a functional role of the m²A2503 modification in translation regulatory mechanisms, perhaps by stabilizing the *syn*- conformation of the base as previously hypothesized³⁴. This model is somewhat supported by the fact that ribosomes containing unmodified A2503 have slightly increased resistance to linezolid, the pleuromutilin antibiotic tiamulin, and the streptogramin A antibiotic virginiamycin M1^{35,36}. As postulated, loss of C2 methylation could result in changes in the antibiotic binding site due to A2503 isomerization to the *anti*- conformation. Clinical reports of linezolid resistance mediated by inactivation of RlmN remain low; however, this may be due to general lack of surveillance for this resistance mechanism.

In addition to the endogenous modification, nucleotide A2503 can become further modified in bacteria that acquire the rRNA-methylating enzyme Cfr, which is encoded by the *chloramphenicol-florfenicol resistance (cfr)* gene³⁷. Like RlmN, Cfr is also a Radical SAM enzyme but methylates the C8 atom of A2503, resulting in the doubly modified m²m⁸A2503³⁸ (**Figure 1.2b**). In contrast to RlmN inactivation, Cfr modification of A2503 results in robust resistance to linezolid, in addition to seven other classes of PTC-targeting drugs including the phenicols, lincosamides, pleuromutilins, streptogramin As, 16-membered macrolides, the aminocyclitol antibiotic hygromycin A, and the nucleoside antibiotic A201A³⁹⁻⁴¹. Since the C8 atom of A2503 faces towards the PTC, methylation at this position would theoretically occlude antibiotic binding (**Figure 1.2c**). However, direct structural evidence for a steric occlusion model is lacking.

The first report of *cfr* of clinical origin was in 2007 from a patient-derived MRSA isolate^{42,43}. Since then, *cfr* has been identified worldwide in a variety of gram-positive and gram-

negative clinical pathogens, including *E. faecium* and *S. aureus*, *S. epidermidis*, and *E. coli* among others⁴⁴⁻⁵⁰. The vast distribution of the *cfr* gene is attributed to its association with mobile genetic elements, such as plasmids and transposable elements.⁴⁵ Furthermore, ribosome methylation by Cfr imparts negligible fitness impacts in *S. aureus*, indicating that *cfr* can be easily disseminated and maintained within bacterial populations⁵¹. Notably, Cfr has been implicated in a number of linezolid-resistant outbreaks at medical centers across the globe, including the United States, and are often associated with prior and/or extensive linezolid treatment⁵²⁻⁵⁸. Cfr is often present with other linezolid resistance determinants, such as mutations in 23S rRNA genes and L3/L4 ribosomal proteins, and ABC-F proteins^{17,18,47,48,57,59-62}.

More recently, variants of Cfr with less than 80% sequence identity have been identified in clinical isolates, referred to as Cfr(B), Cfr(C), Cfr(D), and Cfr(E)⁶³. Cfr(B) has been detected in *Clostridioides* and *Enterococcus* species^{64,65}, and it was demonstrated that Cfr(B) confers resistance to linezolid and other PTC-targeting antibiotics through a mechanism akin to canonical Cfr⁶⁶. Patient-derived Cfr(C) has been identified in *C. difficile* and *Clostridium bolteae*^{67,68}, while Cfr(D) has been identified in *E. faecium* and *E. faecalis* and co-occurs with *optrA* in all isolates to date^{69,70}. The most recently discovered Cfr homologue, Cfr(E) has only been reported in one patient-derived *C. difficile* isolate⁶⁸ but was demonstrated to perform C8-methylation of A2503 in *in vitro* assays. Like Cfr, the more distantly related homologues also appear to be associated with mobile genetic elements, likely facilitating their distribution throughout the bacterial population.

Second-generation oxazolidinone antibiotics

In response to emerging resistance mechanisms, second-generation derivatives of linezolid were developed, most notable being radezolid and tedizolid (**Figure 1.3**). Radezolid is currently in clinical development for bacterial acne and community-acquired pneumonia⁷¹, and tedizolid is approved for the treatment of acute bacterial skin and soft tissue infections⁷². Radezolid and tedizolid contain an additional ring system (D-ring) which makes interactions with rRNA nucleotides located higher up within the A-site of the PTC⁷³. Furthermore, the C5-acetamide, conserved between linezolid and radezolid, is replaced by a hydroxyl group in tedizolid.

Both radezolid and tedizolid exhibit improved efficacy against linezolid-resistant pathogens containing the G2576U mutation in 23S rRNA, OptrA/PoxA, or Cfr^{72,74}. However, molecular rationale for how second generation oxazolidinones overcome these resistance mechanisms is unclear. For example, OptrA/PoxA disrupt the context specific action of linezolid by perturbing placement of the alanine within the nascent peptide. Since it has not been evaluated if context-specificity is a conserved feature of all oxazolidinone antibiotics, exactly how these antibiotics may overcome resistance by ABC-F ribosome protection proteins requires further study. An additional example involves resistance caused by the rRNA methylating enzyme Cfr. The shortened C5 group of tedizolid likely explains its ability to overcome Cfr-mediated resistance, as C8-methylated A2503 has been proposed to sterically clash with the larger C5 acetamide of linezolid (**Figure 1.3**). However, the C5 acetamide is also present in radezolid and, while it has been proposed that compensatory interactions with the D-ring improve affinity for the ribosome, it is unclear how radezolid binds to Cfr-modified ribosomes. Thus, to further the development of antibiotics that can overcome resistance, it will be important to not only obtain

structural information on resistant ribosomes, but also resistant ribosomes in complex with next-generation molecules.

Scope of thesis work

Due to the rising threat of antimicrobial resistance, there is a critical need to understand how resistance mechanisms function and evolve under antibiotic pressure. My thesis works outlined in Chapter 2 involves directed evolution of the rRNA methylating enzyme Cfr, which yielded Cfr variants that provide increased antibiotic resistance, mediated by higher extent of rRNA methylation in cells. We were able to capitalize on the superior methylating capabilities of the evolved Cfr variants to generate a high-resolution structure of a Cfr-modified, resistant ribosome. To bolster the arsenal of antibiotics further, it is also important to understand how antibiotics inhibit their targets, especially critical antibiotics such as linezolid and its derivatives. In Chapter 3, we discover that radezolid has a context-specific mechanism of action similar to linezolid and use this information to generate high resolution cryo-EM structures of linezolid- and radezolid-stalled ribosome complexes. We also obtain a structure of radezolid-stalled with a Cfr-modified ribosome to explain how the second generation oxazolidinone overcomes Cfr-mediated resistance.

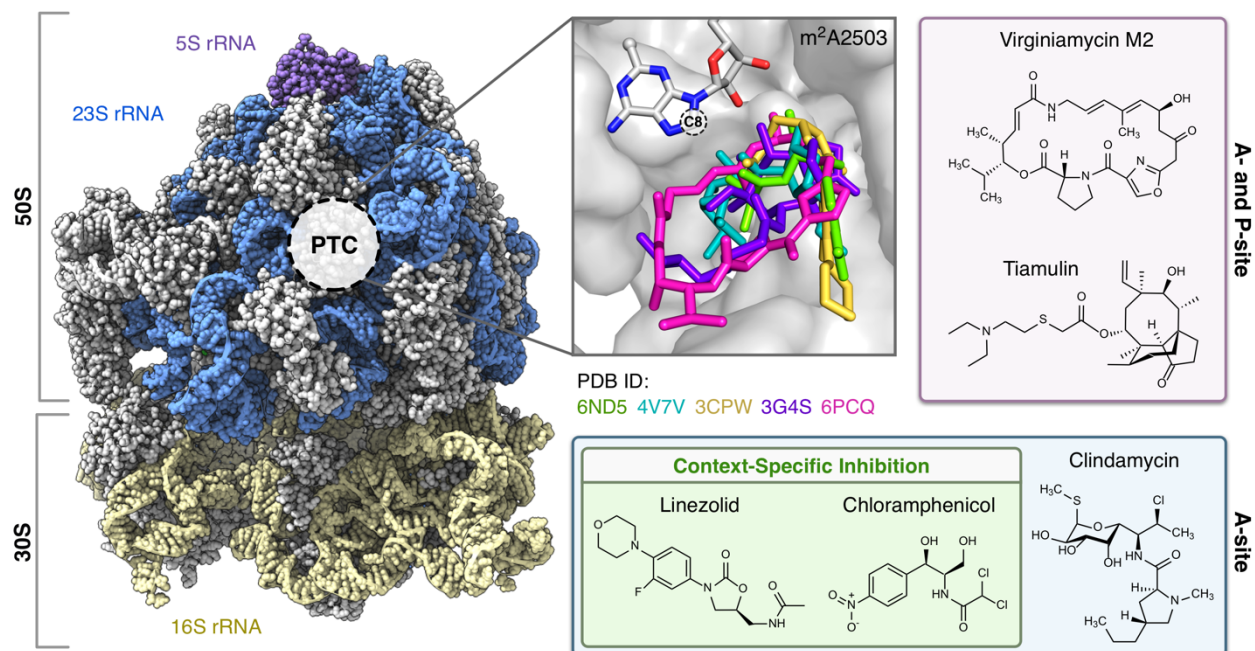


Figure 1.1 | Antibiotics that target the PTC. Structure of the *E. coli* ribosome, highlighting 23S rRNA (blue) and 5S rRNA (purple) within the large 50S ribosomal subunit and 16S rRNA (yellow) within the 30S small ribosomal unit. The peptidyl transferase center (PTC) within the 50S subunit is marked. Overview of the binding mode of select PTC-targeting antibiotics, namely linezolid (oxazolidinone, yellow), chloramphenicol (phenicol, green), clindamycin (lincosamide, teal), virginiamycin M2 (streptogramin A, pink), and tiamulin (pleuromutilin, purple). Antibiotic chemical structures are grouped by binding site, either the A-site alone or both A- and P-site. Linezolid and chloramphenicol, which bind the A-site, have a context-specific mechanism of action.

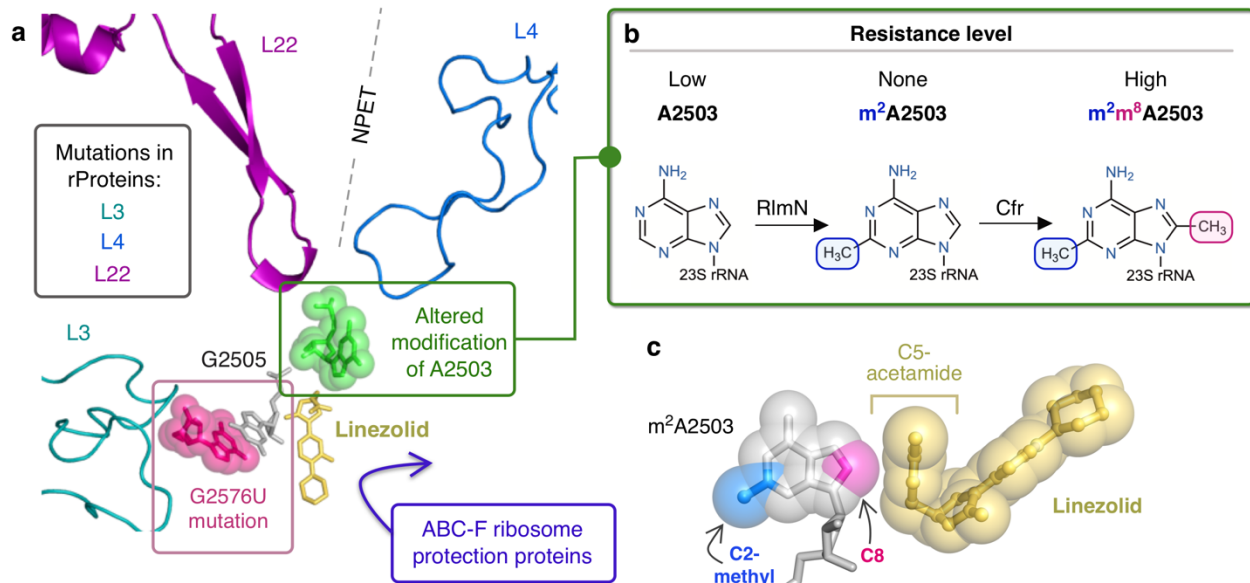


Figure 1.2 | Mechanisms of resistance to linezolid. (a) Emerging resistance mechanisms include mutation of rProteins (L3, L4, and L22) and 23S rRNA nucleotide G2576U (pink), among others, in addition to ABC-F ribosome protection proteins OptrA and PoxTA, and alteration of the post-transcriptional modification state of A2503 (green). The rProteins L4 and L22 line the nascent peptide exit tunnel (NPET). (b) Modification of A2503 within 23S rRNA by the Radical-SAM methylating enzymes RlmN and Cfr. Unmodified A2503 confers low-level resistance, while the Cfr modification results in high levels of resistance. (c) Cfr resistance is presumably due to steric collision between the installed methyl group at the C8 atom and C5-acetamide group of linezolid.

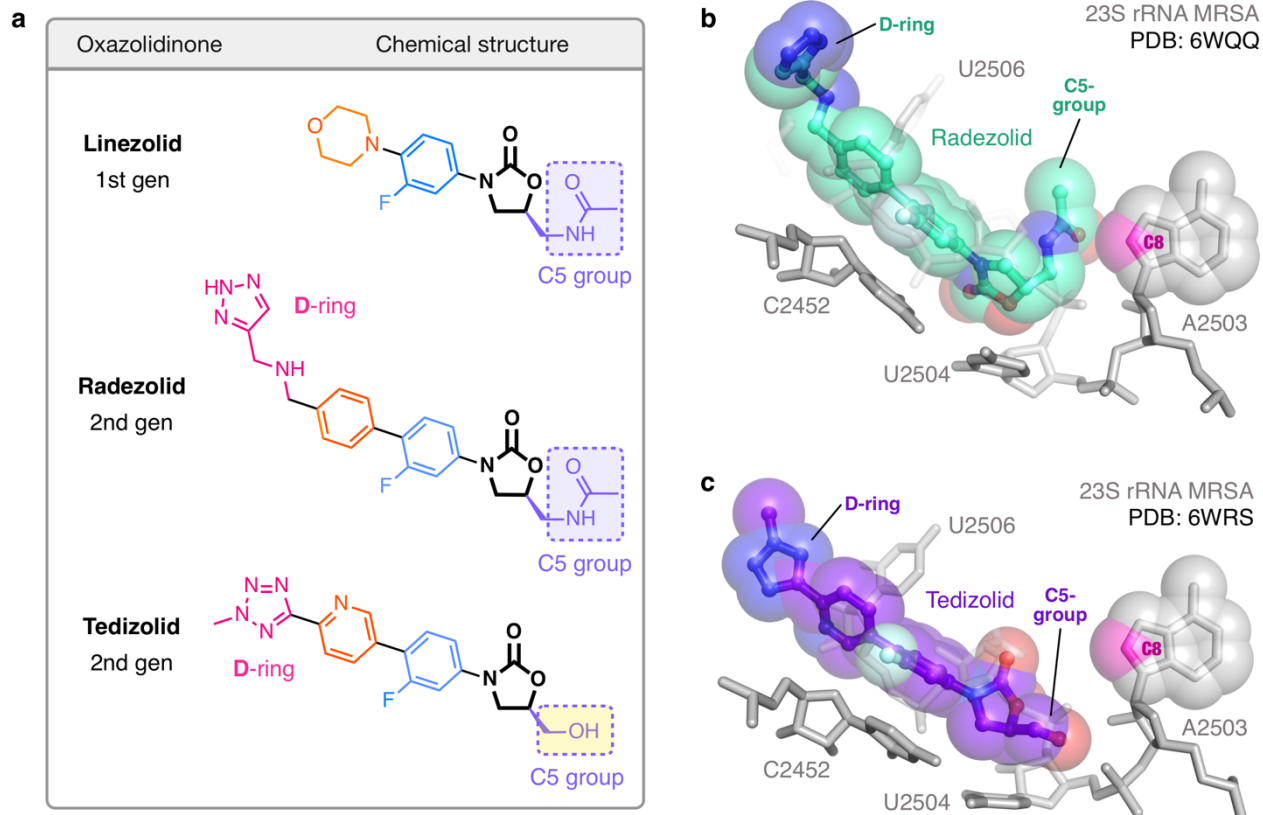


Figure 1.3 | Second generation oxazolidinone antibiotics. (a) Chemical structures of linezolid and its derivatives, radezolid and tedizolid, highlighting the C5-groups additional D-ring system in the second generation oxazolidinone molecules. (b) The binding mode of radezolid within the PTC of a MRSA ribosome. (c) The binding mode of tedizolid within the PTC of a MRSA ribosome. For panels (b) and (c), the C8 carbon of A2503 that is methylated by Cfr is in pink.

References

1. Ramakrishnan, V. Ribosome structure and the mechanism of translation. *Cell* **108**, 557–572 (2002).
2. Arenz, S. & Wilson, D. N. Bacterial Protein Synthesis as a Target for Antibiotic Inhibition. *Cold Spring Harb. Perspect. Med.* **6**, (2016).
3. Wilson, D. N. The A–Z of bacterial translation inhibitors. *Critical Reviews in Biochemistry and Molecular Biology* vol. 44 393–433 (2009).
4. Lin, J., Zhou, D., Steitz, T. A., Polikanov, Y. S. & Gagnon, M. G. Ribosome-Targeting Antibiotics: Modes of Action, Mechanisms of Resistance, and Implications for Drug Design. *Annu. Rev. Biochem.* **87**, 451–478 (2018).
5. Wilson, D. N. Ribosome-targeting antibiotics and mechanisms of bacterial resistance. *Nat. Rev. Microbiol.* **12**, 35–48 (2014).
6. Nissen, P., Hansen, J., Ban, N., Moore, P. B. & Steitz, T. A. The structural basis of ribosome activity in peptide bond synthesis. *Science* **289**, 920–930 (2000).
7. Brickner, S. J., Barbachyn, M. R., Hutchinson, D. K. & Manninen, P. R. Linezolid (ZYVOX), the first member of a completely new class of antibacterial agents for treatment of serious gram-positive infections. *J. Med. Chem.* **51**, 1981–1990 (2008).
8. Hashemian, S. M. R., Farhadi, T. & Ganjparvar, M. Linezolid: a review of its properties, function, and use in critical care. *Drug Des. Devel. Ther.* **12**, 1759–1767 (2018).
9. Geneva: World Health Organization. *World Health Organization Model List of Essential Medicines – 22nd List.* (2021).
10. Colca, J. R. *et al.* Cross-linking in the living cell locates the site of action of oxazolidinone antibiotics. *J. Biol. Chem.* **278**, 21972–21979 (2003).

11. Ippolito, J. A. *et al.* Crystal structure of the oxazolidinone antibiotic linezolid bound to the 50S ribosomal subunit. *J. Med. Chem.* **51**, 3353–3356 (2008).
12. Wilson, D. N. *et al.* The oxazolidinone antibiotics perturb the ribosomal peptidyl-transferase center and effect tRNA positioning. *Proc. Natl. Acad. Sci. U. S. A.* **105**, 13339–13344 (2008).
13. Eyal, Z. *et al.* Structural insights into species-specific features of the ribosome from the pathogen *Staphylococcus aureus*. *Proc. Natl. Acad. Sci. U. S. A.* **112**, E5805–14 (2015).
14. Marks, J. *et al.* Context-specific inhibition of translation by ribosomal antibiotics targeting the peptidyl transferase center. *Proc. Natl. Acad. Sci. U. S. A.* **113**, 12150–12155 (2016).
15. Choi, J. *et al.* Dynamics of the context-specific translation arrest by chloramphenicol and linezolid. *Nat. Chem. Biol.* **16**, 310–317 (2020).
16. Svetlov, M. S. *et al.* High-resolution crystal structures of ribosome-bound chloramphenicol and erythromycin provide the ultimate basis for their competition. *RNA* **25**, 600–606 (2019).
17. Long, K. S. & Vester, B. Resistance to linezolid caused by modifications at its binding site on the ribosome. *Antimicrob. Agents Chemother.* **56**, 603–612 (2012).
18. Besier, S., Ludwig, A., Zander, J., Brade, V. & Wichelhaus, T. A. Linezolid resistance in *Staphylococcus aureus*: gene dosage effect, stability, fitness costs, and cross-resistances. *Antimicrob. Agents Chemother.* **52**, 1570–1572 (2008).
19. Trevino, M. *et al.* Endemic linezolid-resistant *Staphylococcus epidermidis* in a critical care unit. *Eur. J. Clin. Microbiol. Infect. Dis.* **28**, 527–533 (2009).
20. Ruggero, K. A., Schroeder, L. K., Schreckenberger, P. C., Mankin, A. S. & Quinn, J. P. Nosocomial superinfections due to linezolid-resistant *Enterococcus faecalis*: evidence for a gene dosage effect on linezolid MICs. *Diagn. Microbiol. Infect. Dis.* **47**, 511–513 (2003).

21. Tsiodras, S. *et al.* Linezolid resistance in a clinical isolate of *Staphylococcus aureus*. *The Lancet* vol. 358 207–208 (2001).
22. Turner, A. M., Lee, J. Y. H., Gorrie, C. L., Howden, B. P. & Carter, G. P. Genomic Insights Into Last-Line Antimicrobial Resistance in Multidrug-Resistant *Staphylococcus* and Vancomycin-Resistant *Enterococcus*. *Front. Microbiol.* **12**, 637656 (2021).
23. Belousoff, M. J. *et al.* Structural Basis for Linezolid Binding Site Rearrangement in the *Staphylococcus aureus* Ribosome. *MBio* **8**, (2017).
24. Halfon, Y. *et al.* Exit tunnel modulation as resistance mechanism of *S. aureus* erythromycin resistant mutant. *Sci. Rep.* **9**, 11460 (2019).
25. Wang, Y. *et al.* A novel gene, *optrA*, that confers transferable resistance to oxazolidinones and phenicols and its presence in *Enterococcus faecalis* and *Enterococcus faecium* of human and animal origin. *J. Antimicrob. Chemother.* **70**, 2182–2190 (2015).
26. Antonelli, A. *et al.* Characterization of *poxtA*, a novel phenicol–oxazolidinone–tetracycline resistance gene from an MRSA of clinical origin. *J. Antimicrob. Chemother.* **73**, 1763–1769 (2018).
27. Crowe-McAuliffe, C., Murina, V., Kasari, M. & Takada, H. Structural basis for PoxTA-mediated resistance to Phenicol and Oxazolidinone antibiotics. *bioRxiv* (2021).
28. Golovina, A. Y. *et al.* The last rRNA methyltransferase of *E. coli* revealed: the *yhiR* gene encodes adenine-N6 methyltransferase specific for modification of A2030 of 23S ribosomal RNA. *RNA* **18**, 1725–1734 (2012).
29. Toh, S.-M., Xiong, L., Bae, T. & Mankin, A. S. The methyltransferase YfgB/RlmN is responsible for modification of adenosine 2503 in 23S rRNA. *RNA* **14**, 98–106 (2008).

30. Benítez-Páez, A., Villarroya, M. & Armengod, M.-E. The Escherichia coli RlmN methyltransferase is a dual-specificity enzyme that modifies both rRNA and tRNA and controls translational accuracy. *RNA* **18**, 1783–1795 (2012).
31. Yan, F. *et al.* RlmN and Cfr are radical SAM enzymes involved in methylation of ribosomal RNA. *J. Am. Chem. Soc.* **132**, 3953–3964 (2010).
32. Grove, T. L. *et al.* A Radically Different Mechanism for S-Adenosylmethionine-Dependent Methyltransferases. *Science* (2011) doi:10.1126/science.1200877.
33. Atkinson, G. C. *et al.* Distinction between the Cfr methyltransferase conferring antibiotic resistance and the housekeeping RlmN methyltransferase. *Antimicrob. Agents Chemother.* **57**, 4019–4026 (2013).
34. Vázquez-Laslop, N., Ramu, H., Klepacki, D., Kannan, K. & Mankin, A. S. The key function of a conserved and modified rRNA residue in the ribosomal response to the nascent peptide. *EMBO J.* **29**, 3108–3117 (2010).
35. Stojković, V., Noda-Garcia, L., Tawfik, D. S. & Fujimori, D. G. Antibiotic resistance evolved via inactivation of a ribosomal RNA methylating enzyme. *Nucleic Acids Res.* **44**, 8897–8907 (2016).
36. LaMarre, J. M., Howden, B. P. & Mankin, A. S. Inactivation of the indigenous methyltransferase RlmN in Staphylococcus aureus increases linezolid resistance. *Antimicrob. Agents Chemother.* **55**, 2989–2991 (2011).
37. Kehrenberg, C., Schwarz, S., Jacobsen, L., Hansen, L. H. & Vester, B. A new mechanism for chloramphenicol, florfenicol and clindamycin resistance: methylation of 23S ribosomal RNA at A2503. *Molecular Microbiology* vol. 57 1064–1073 (2005).

38. Giessing, A. M. B. *et al.* Identification of 8-methyladenosine as the modification catalyzed by the radical SAM methyltransferase Cfr that confers antibiotic resistance in bacteria. *RNA* **15**, 327–336 (2009).
39. Long, K. S., Poehlsgaard, J., Kehrenberg, C., Schwarz, S. & Vester, B. The Cfr rRNA methyltransferase confers resistance to Phenicol, Lincosamides, Oxazolidinones, Pleuromutilins, and Streptogramin A antibiotics. *Antimicrob. Agents Chemother.* **50**, 2500–2505 (2006).
40. Smith, L. K. & Mankin, A. S. Transcriptional and translational control of the mlr operon, which confers resistance to seven classes of protein synthesis inhibitors. *Antimicrob. Agents Chemother.* **52**, 1703–1712 (2008).
41. Polikanov, Y. S. *et al.* Distinct tRNA Accommodation Intermediates Observed on the Ribosome with the Antibiotics Hygromycin A and A201A. *Mol. Cell* **58**, 832–844 (2015).
42. Toh, S.-M. *et al.* Acquisition of a natural resistance gene renders a clinical strain of methicillin-resistant *Staphylococcus aureus* resistant to the synthetic antibiotic linezolid. *Mol. Microbiol.* **64**, 1506–1514 (2007).
43. Arias, C. A. *et al.* Clinical and microbiological aspects of linezolid resistance mediated by the cfr gene encoding a 23S rRNA methyltransferase. *J. Clin. Microbiol.* **46**, 892–896 (2008).
44. Vester, B. The cfr and cfr-like multiple resistance genes. *Res. Microbiol.* **169**, 61–66 (2018).
45. Shen, J., Wang, Y. & Schwarz, S. Presence and dissemination of the multiresistance gene cfr in Gram-positive and Gram-negative bacteria. *J. Antimicrob. Chemother.* **68**, 1697–1706 (2013).
46. Patel, S. N. *et al.* Linezolid resistance in *Enterococcus faecium* isolated in Ontario, Canada. *Diagn. Microbiol. Infect. Dis.* **77**, 350–353 (2013).

47. Tewhey, R. *et al.* Mechanisms of Linezolid Resistance among Coagulase-Negative Staphylococci Determined by Whole-Genome Sequencing. *mBio* vol. 5 (2014).
48. Zhang, Y. *et al.* A high incidence and coexistence of multiresistance genes *cfr* and *optrA* among linezolid-resistant enterococci isolated from a teaching hospital in Wenzhou, China. *Eur. J. Clin. Microbiol. Infect. Dis.* **37**, 1441–1448 (2018).
49. Morroni, G. *et al.* Characterization of a Multiresistance Plasmid Carrying the *optrA* and *cfr* Resistance Genes From an *Enterococcus faecium* Clinical Isolate. *Front. Microbiol.* **9**, 2189 (2018).
50. Locke, J. B., Rahawi, S., Lamarre, J., Mankin, A. S. & Shaw, K. J. Genetic environment and stability of *cfr* in methicillin-resistant *Staphylococcus aureus* CM05. *Antimicrob. Agents Chemother.* **56**, 332–340 (2012).
51. LaMarre, J. M., Locke, J. B., Shaw, K. J. & Mankin, A. S. Low fitness cost of the multidrug resistance gene *cfr*. *Antimicrob. Agents Chemother.* **55**, 3714–3719 (2011).
52. Bonilla, H. *et al.* Multicity outbreak of linezolid-resistant *Staphylococcus epidermidis* associated with clonal spread of a *cfr*-containing strain. *Clin. Infect. Dis.* **51**, 796–800 (2010).
53. Morales, G. *et al.* Resistance to linezolid is mediated by the *cfr* gene in the first report of an outbreak of linezolid-resistant *Staphylococcus aureus*. *Clin. Infect. Dis.* **50**, 821–825 (2010).
54. Baos, E., Candel, F. J., Merino, P., Pena, I. & Picazo, J. J. Characterization and monitoring of linezolid-resistant clinical isolates of *Staphylococcus epidermidis* in an intensive care unit 4 years after an outbreak of infection by *cfr*-mediated linezolid-resistant *Staphylococcus aureus*. *Diagn. Microbiol. Infect. Dis.* **76**, 325–329 (2013).

55. Cai, J. C., Hu, Y. Y., Zhou, H. W., Chen, G.-X. & Zhang, R. Dissemination of the same cfr-carrying plasmid among methicillin-resistant *Staphylococcus aureus* and coagulase-negative staphylococcal isolates in China. *Antimicrob. Agents Chemother.* **59**, 3669–3671 (2015).
56. Layer, F. *et al.* Dissemination of linezolid-dependent, linezolid-resistant *Staphylococcus epidermidis* clinical isolates belonging to CC5 in German hospitals. *J. Antimicrob. Chemother.* **73**, 1181–1184 (2018).
57. Lazaris, A. *et al.* Novel multiresistance cfr plasmids in linezolid-resistant methicillin-resistant *Staphylococcus epidermidis* and vancomycin-resistant *Enterococcus faecium* (VRE) from a hospital outbreak: co-location of cfr and *optrA* in VRE. *J. Antimicrob. Chemother.* **72**, 3252–3257 (2017).
58. Weßels, C. *et al.* Emergence and control of linezolid-resistant *Staphylococcus epidermidis* in an ICU of a German hospital. *J. Antimicrob. Chemother.* **73**, 1185–1193 (2018).
59. Locke, J. B. *et al.* Elevated linezolid resistance in clinical cfr-positive *Staphylococcus aureus* isolates is associated with co-occurring mutations in ribosomal protein L3. *Antimicrob. Agents Chemother.* **54**, 5352–5355 (2010).
60. Gao, W. *et al.* Two novel point mutations in clinical *Staphylococcus aureus* reduce linezolid susceptibility and switch on the stringent response to promote persistent infection. *PLoS Pathog.* **6**, e1000944 (2010).
61. Gu, B., Kelesidis, T., Tsiodras, S., Hindler, J. & Humphries, R. M. The emerging problem of linezolid-resistant *Staphylococcus*. *J. Antimicrob. Chemother.* **68**, 4–11 (2013).
62. Mendes, R. E. *et al.* First report of cfr-mediated resistance to linezolid in human staphylococcal clinical isolates recovered in the United States. *Antimicrob. Agents Chemother.* **52**, 2244–2246 (2008).

63. Schwarz, S. *et al.* Mobile Oxazolidinone Resistance Genes in Gram-Positive and Gram-Negative Bacteria. *Clin. Microbiol. Rev.* **34**, e0018820 (2021).
64. Deshpande, L. M. *et al.* Detection of a New cfr-Like Gene, cfr(B), in *Enterococcus faecium* Isolates Recovered from Human Specimens in the United States as Part of the SENTRY Antimicrobial Surveillance Program. *Antimicrob. Agents Chemother.* **59**, 6256–6261 (2015).
65. Marín, M. *et al.* *Clostridium difficile* isolates with high linezolid MICs harbor the multiresistance gene cfr. *Antimicrob. Agents Chemother.* **59**, 586–589 (2015).
66. Hansen, L. H. & Vester, B. A cfr-like gene from *Clostridium difficile* confers multiple antibiotic resistance by the same mechanism as the cfr gene. *Antimicrob. Agents Chemother.* **59**, 5841–5843 (2015).
67. Candela, T., Marvaud, J.-C., Nguyen, T. K. & Lambert, T. A cfr-like gene cfr(C) conferring linezolid resistance is common in *Clostridium difficile*. *Int. J. Antimicrob. Agents* **50**, 496–500 (2017).
68. Stojković, V. *et al.* cfr(B), cfr(C), and a New cfr-Like Gene, cfr(E), in *Clostridium difficile* Strains Recovered across Latin America. *Antimicrob. Agents Chemother.* **64**, (2019).
69. Pang, S. *et al.* Linezolid-resistant ST872 *Enterococcus faecium* harbouring *optrA* and cfr (D) oxazolidinone resistance genes. *Int. J. Antimicrob. Agents* **55**, 105831 (2020).
70. Ruiz-Ripa, L. *et al.* Mechanisms of Linezolid Resistance Among Enterococci of Clinical Origin in Spain—Detection of *optrA*- and cfr(D)-Carrying *E. faecalis*. *Microorganisms* vol. 8 1155 (2020).
71. Shaw, K. J. & Barbachyn, M. R. The oxazolidinones: past, present, and future. *Ann. N. Y. Acad. Sci.* **1241**, 48–70 (2011).

72. Moellering, R. C., Jr. Tedizolid: a novel oxazolidinone for Gram-positive infections. *Clin. Infect. Dis.* **58 Suppl 1**, S1–3 (2014).
73. Wright, A. *et al.* Characterization of the Core Ribosomal Binding Region for the Oxazolidone Family of Antibiotics Using Cryo-EM. *ACS Pharmacol Transl Sci* **3**, 425–432 (2020).
74. Skripkin, E. *et al.* R chi-01, a new family of oxazolidinones that overcome ribosome-based linezolid resistance. *Antimicrob. Agents Chemother.* **52**, 3550–3557 (2008).x

Chapter 2

Directed evolution of the rRNA methylating enzyme Cfr reveals the molecular basis of antibiotic resistance

Abstract

Alteration of antibiotic binding sites through modification of ribosomal RNA (rRNA) is a common form of resistance to ribosome-targeting antibiotics. The rRNA-modifying enzyme Cfr methylates an adenosine nucleotide within the peptidyl transferase center, resulting in the C-8 methylation of A2503 (m⁸A2503) and resistance to eight classes of ribosome-targeting antibiotics. Despite the prevalence of this resistance mechanism, it is poorly understood how bacteria may modulate Cfr methylation to adapt to antibiotic pressure. Moreover, direct evidence for how m⁸A2503 alters antibiotic binding sites within the ribosome is lacking. In this study, we performed directed evolution of Cfr under antibiotic selection to generate Cfr variants that confer increased resistance by enhancing methylation of A2503 in cells. Increased rRNA methylation is achieved by improved expression and stability of Cfr, which may be exploited by pathogens under antibiotic stress as suggested by natural isolates. Using a variant which achieves near-stoichiometric methylation of rRNA, we determined a 2.2 Å cryo-EM structure of the Cfr-modified ribosome. Our structure reveals the molecular basis for broad resistance to antibiotics and will inform the design of new antibiotics that overcome resistance mediated by Cfr.

Introduction

A large portion of clinically relevant antibiotics halt bacterial growth by binding to the ribosome and inhibiting protein synthesis¹⁻³. Since antibiotic binding sites are primarily composed of ribosomal RNA (rRNA), rRNA-modifying enzymes that alter antibiotic binding pockets are central to evolved resistance^{4,5}. The rRNA-methylating enzyme Cfr modifies an adenosine nucleotide located within the peptidyl transferase center (PTC), a region of the ribosome essential for catalyzing peptide bond formation and consequently, a common target for antibiotics^{6,7}. Cfr is

a radical SAM enzyme that methylates the C8 carbon of adenosine at position 2503 (m⁸A2503, *E. coli* numbering)⁸⁻¹². Due to the proximal location of A2503 to many antibiotic binding sites, introduction of a single methyl group is sufficient to cause resistance to eight classes of antibiotics simultaneously: **p**henicols, **l**incosamides, **o**xazolidinones, **p**leuromutilins, **s**treptogramin **A** (PhLOPS_A), in addition to nucleoside analog A201A, hygromycin A, and 16-membered macrolides¹³⁻¹⁵. Among rRNA modifying enzymes, this extensive cross-resistance phenotype is unique to Cfr and presents a major clinical problem.

Cfr emergence in human pathogens appears to be a recent event, with the first case reported in 2007 from a patient-derived *Staphylococcus aureus* isolate^{16,17}. Since then, the *cfr* gene has been identified across the globe in both gram-positive and gram-negative bacteria, including *E. coli*^{18,19}, and has been associated with several clinical resistance outbreaks to the oxazolidinone antibiotic, linezolid²⁰⁻²⁷. The vast spread of Cfr is attributed to its association with mobile genetic elements and relatively low impact on bacterial fitness, suggesting that *cfr* can be rapidly disseminated within bacterial populations^{28,29}.

Due to the ability of Cfr to confer resistance to several antibiotics simultaneously, it is critical to understand how bacteria may adapt under antibiotic pressure to enhance Cfr activity and bolster protection against ribosome-targeting molecules. Identification of Cfr mutations that improve resistance will also be critical for informing clinical surveillance and designing strategies to counteract resistance. A major limitation in our current understanding of Cfr-mediated resistance is the lack of structural insight into changes in the ribosome because of Cfr modification. Steric occlusion of antibiotic binding has been proposed as a model to rationalize altered antibiotic susceptibility¹⁵. Additionally, the observation that A2503 can adopt both *syn* and *anti*-conformations in previously reported ribosome structures suggests that methylation may regulate

conformation of the base, as previously proposed^{30–33}. However, direct evidence for how m⁸A2053 alters antibiotic binding sites to inform the design of next-generation molecules that can overcome Cfr resistance is lacking.

In this study, we identified mechanisms that enhance antibiotic resistance by performing directed evolution of a *cfr* found in a clinical MRSA isolate under antibiotic selection³⁴. The obtained highly resistant Cfr variants show increased rRNA methylation, driven primarily by robust improvements in Cfr cellular levels, achieved either by higher transcription or increased translation and improved cellular stability. In particular, mutation of the second Cfr amino acid to lysine strongly enhances translation and resistance. Lastly, we used an evolved variant which achieves near-stoichiometric rRNA methylation to generate a high-resolution cryo-EM structure of the Cfr-modified *E. coli* ribosome. The obtained structural insights provide a rationale for how m⁸A2503 causes resistance to ribosome antibiotics.

Results

Evolved Cfr variants confer enhanced antibiotic resistance

To perform directed evolution of Cfr, we used error-prone PCR (EP-PCR) to randomly introduce 1-3 mutations into the *cfr* gene obtained from a clinical MRSA isolate¹⁶, herein referred to as CfrWT (**Figure 2.1a**). Mutagenized *cfr* sequences were then cloned into a pZA vector where Cfr was expressed under tetracycline-inducible promoter P_{tet} introduced to enable precise control of Cfr expression³⁵. The resulting library of ~10⁷ *E. coli* transformants was selected for growth in the presence of increasing amounts of tiamulin, a pleuromutilin antibiotic to which Cfr confers resistance. During each round, a subset of the surviving colonies was sequenced to identify new mutations. After two rounds of evolution, wild-type Cfr was no longer detected, indicating that the

introduced mutations provide enhanced survivability in the presence of tiamulin. After five rounds of mutation and selection, we performed two rounds of selection without mutagenesis, and with high tiamulin concentrations, thus leading to fixation of mutations that provide robust resistance.

Analysis of surviving *cfr* sequences from the final rounds of selection revealed notable trends (**Table 2.1**, **Table 2.2**). Three positions were primarily mutated: N2, I26, and S39. By homology modeling, these mutational hotspots appear distal from the enzyme active site (>12 Å; **Figure 2.1b**). In fact, these mutations reside in what has been predicted to be an N-terminal accessory domain separate from the radical-SAM catalytic domain⁹. Secondly, ~28% of sequences contained alterations to the promoter. These alterations consist of either P_{tet} duplication, or insertion of a partial P_{tet} sequence (**Table 2.3**).

We selected 7 evolved Cfr variants, referred herein as CfrV1-V7, as representative mutational combinations for further characterization (**Figure 2.1c**). All selected Cfr variants contain mutations in the *cfr* open reading frame while CfrV6 and CfrV7 also harbor P_{tet} alterations (**Figure 2.1d**). Compared to CfrWT, these variants confer ~2 to ~16-fold enhanced resistance to PhLOPS_A antibiotics, yet with no changes in susceptibility to trimethoprim, an antibiotic that does not inhibit the ribosome (**Figure 2.1e**). The robustness of resistance, and the absence of active-site mutations, suggests Cfr variants do not act as dominant-negative enzymes that inhibit C-2 methylation of A2503, as observed in a previous directed evolution experiment³⁶. Furthermore, the specificity of resistance to PhLOPS_A antibiotics suggests that these Cfr variants elicit their effects through PTC modification rather than triggering a stress response that confers global resistance.

Variants exhibit increased rRNA methylation and Cfr protein levels

To test the hypothesis that Cfr variants mediate higher resistance by increasing the fraction of ribosomes with m⁸A2503, we evaluated the methylation status of A2503 by mass spectrometry. Specifically, we expressed Cfr in *E. coli* and used oligonucleotide protection to isolate a 40-nt fragment of 23S rRNA containing A2503^{37,38}. The isolated fragment was then enzymatically digested and analyzed by MALDI-TOF mass spectrometry (**Figure 2.2a**). As expected, an empty vector produces a 1013 m/z fragment corresponding to the mono-methylated m²A2503, modification installed by the endogenous enzyme RlmN. Upon expression of Cfr, we observe a reduction in the 1013 m/z peak and the emergence of a new peak at 1027 m/z, corresponding to m²A2503 conversion into hypermethylated m²m⁸A2503. CfrWT can convert less than ~40% of m²A2503 into the hypermethylated m²m⁸A2503 product. In contrast, the evolved variants achieve ~50-90% methylation of A2503, indicating that variants are more active than CfrWT *in vivo*.

The ability of evolved Cfr variants to achieve enhanced ribosome methylation *in vivo* could be attributed to enhanced enzymatic activity and/or higher levels of functional enzyme. To test the hypothesis that Cfr variants achieve higher turnover number, we anaerobically purified and reconstituted CfrWT and a representative evolved variant, CfrV4. We then evaluated the ability of CfrWT and CfrV4 to methylate a 23S rRNA fragment (2447-2625) *in vitro* by monitoring the incorporation of radioactivity from [³H-methyl] S-adenosylmethionine (SAM) into RNA substrate under saturating conditions³⁹. However, no significant difference in k_{cat} between CfrWT ($3.45 \times 10^{-2} \pm 3.2 \times 10^{-3} \text{ min}^{-1}$) and CfrV4 ($2.25 \times 10^{-2} \pm 1.3 \times 10^{-3} \text{ min}^{-1}$) was observed (**Figure 2.3**).

Given these findings, we hypothesized that the variants might alter protein levels. To monitor Cfr protein levels, we inserted a flexible linker followed by a C-terminal FLAG tag, which does not alter resistance. Interestingly, immunoblotting against FLAG revealed that in addition to

full-length Cfr, N-terminally truncated Cfr proteins are also produced (**Figure 2.2b**). The truncations result from translation initiation at internal methionine residues but do not contribute to resistance (**Figure 2.4**), indicating that they are non-functional enzymes unable to methylate A2503. Interestingly the larger molecular weight truncation is present only in CfrV1/V4/V6 and is generated by the I26M mutation introduced during directed evolution. Quantification of resistance-causative, full-length Cfr proteins alone revealed that the evolved variants achieve ~20-100-fold higher steady-state protein levels than CfrWT (**Figure 2.2b**).

We measured transcript levels for all variants to assess the contribution of altered transcription to increased protein levels. For Cfr variants with promoter alterations, enhanced production of the Cfr transcript is a large contributor to Cfr protein expression, as CfrV6 and CfrV7 exhibit ~6 and ~10-fold enhancement in Cfr mRNA levels compared to CfrWT, respectively (**Figure 2.2c**). We also observe a ~2 to 3-fold increase in mRNA levels for CfrV1-5. Despite the observed increase in mRNA levels for CfrV-15, this alone cannot explain the multi-fold improvement in protein expression and indicates that these variants also boost protein levels through a post-transcriptional process. This is further supported by the expression profiles for CfrV1-5, which are dominated by the full-length protein (**Figure 2.2d**). Interestingly, enhanced production of Cfr protein correlates with larger fitness defects in *E. coli*, with an increase in doubling time of ~4 min for CfrV7 compared to empty vector in the absence of antibiotics (**Figure 2.2e**).

Promoter and second position mutations drive Cfr resistance

Given that the evolved variants achieve robust enhancement in Cfr expression we sought to elucidate the mechanism(s) by which this occurs. To evaluate the importance of promoter

alterations, we generated a construct where the P_{tet}* promoter sequence from CfrV6 was inserted upstream of CfrWT open reading frame, herein referred to as P_{tet}*V6. The insertion of P_{tet}* alone was sufficient to elicit improvement in Cfr expression (**Figure 2.5a**). Furthermore, *E. coli* expressing P_{tet}*V6 resembled CfrV6 in its ability to survive in the presence of chloramphenicol (**Figure 2.5b**). Together, these results suggest the altered promoter drives expression and resistance for CfrV6.

To investigate the contributions of mutations within the Cfr protein, we generated constructs containing Cfr mutations N2K/I, I26M, and S39G in isolation. Interestingly, we observe that mutations at the second position, N2K and N2I, display the largest enhancements in expression, ~27-fold and ~12-fold respectively (**Figure 2.5a**). The dominance of the second position mutants in driving antibiotic resistance is further manifested by *E. coli* expressing CfrN2K, but not I26M or S39G, exhibiting survival similar to that of the triple mutant, CfrV3, in the presence of chloramphenicol (**Figure 2.5c**). Together, these results suggest that the second position mutations drive the robust expression and resistance observed for CfrV1-5. Of note, ribosome methylation by the produced Cfr does not impact the translation of CfrN2K, as this mutant and its corresponding catalytically inactive double mutant protein CfrN2K_C338A are similarly highly expressed (**Figure 2.6**).

Mutations impact Cfr translation and degradation

The Cfr coding mutations drive enhanced steady-state protein levels of Cfr protein through a post-transcriptional process. However, because levels at steady-state reflect the net effect of protein synthesis and degradation, we sought to evaluate how Cfr mutations impact both processes,

especially since the nature of N-terminal amino acids and codons can greatly influence both translation and degradation in bacteria^{40–51}.

To test the hypothesis that second position mutations enhance translation of mutants, we used polysome profiling to evaluate the relative abundance of Cfr mRNA in polysome fractions. Polysome profiles derived from 10–55% sucrose gradients appear similar across biological conditions, suggesting expression of Cfr^{WT} and its evolved mutants do not affect global translation (**Figure 2.7a**). Cfr^{WT} transcripts migrate with low polysomes (fractions 10, 11) (**Figure 2.7c**). In contrast, Cfr^{V4} transcripts are strongly shifted toward high polysomes (fractions 16, 17), which indicate that Cfr^{V4} mRNA is associated with a large quantity of ribosomes and is better translated than Cfr^{WT} (**Figure 2.7d**). Further support that Cfr^{V4} is well-translated is the observation that Cfr^{V4} mRNA co-migrates with mRNA of the well-translated housekeeping gene, *recA*⁵². At least in part, this is due to the N2K mutation which shifts transcripts to higher polysome fractions (fractions 12, 13) (**Figure 2.7c**). The *recA* control mRNA shows excellent reproducibility across biological samples, indicating that the observed shift of mutant Cfr transcripts towards higher polysomes is due to introduced mutations (**Figure 2.7b**). Taken together, these results suggest that enhanced translation is a cumulative effect of N2K and other ORF mutations obtained by directed evolution.

To further interrogate the role of second position mutations in Cfr translation, we determined the second codon identity for all sequenced variants from the final rounds of evolution (**Table 2.1, Table 2.2**). Interestingly, all N2K mutations were encoded by an AAA codon, while AUU encoded all N2I mutations. In *E. coli*, the tRNA molecules that decode K(AAA) and I(AUU) are slightly more abundant than the wild-type N(AAU), accounting for 3.0% and 5.4% of the tRNA pool compared to 1.9%, respectively⁵³. To test if tRNA abundance and codon sequence contribute

to enhanced translation, we evaluated the impact of synonymous codons on protein expression. Lysine codons AAA and AAG are decoded by the same tRNA^{Lys} in *E. coli*. Interestingly, mutating CfrN2K from AAA to AAG, which increases G/C content, did not significantly impact expression (**Figure 2.8**). The isoleucine AUA codon is decoded by the low-abundant tRNA^{Ile2} 54,55. Mutation of N2I from AUU to the AUA rare codon resulted in a ~2-fold decrease in Cfr expression, supporting tRNA abundance as a contributing factor (**Figure 2.8**).

To evaluate the impact of mutations introduced during directed evolution on protein half-life, we monitored changes in protein abundance over time after halting expression with rifampicin (**Figure 2.7e**). While CfrWT is rapidly degraded with a half-life of ~20 min, CfrN2K/I exhibit increased half-lives of ~60 min. These results suggest that mutation of the second amino acid to lysine or isoleucine contributes to improved steady-state expression both by enhancing translation and stability of Cfr in the cell. CfrS39G also exhibits an increased half-life of ~60 min. The half-life increase is the most pronounced for the I26M single point mutant and similar to that of the triple-mutant, CfrV3 (>100 min for both proteins). Together, these results suggest that evolved variants achieve higher expression through mutations that both enhance translation and decrease degradation of mutant Cfr proteins.

Evolved Cfr enables understanding of the structural basis of resistance

Molecular understanding of Cfr-mediated resistance to antibiotics necessitates structural insights into methylated ribosomes. However, obtaining the structure of a Cfr-modified ribosome has been so far hampered by moderate methylation efficiency of *S. aureus* Cfr, a challenge that can be addressed by the improved methylation ability of directed evolution variants. Of all characterized evolved variants, CfrV7 achieves the highest levels of antibiotic resistance and

methylation of rRNA, providing a unique tool for structural determination. Relative peak quantification of the MALDI spectra revealed that CfrV7 achieved near-stoichiometric (~90%) m⁸A2503 methylation (**Figure 2.2**).

Ribosomes were purified from *E. coli* expressing CfrV7 to obtain a 2.2 Å cryo-EM structure of the Cfr-modified 50S ribosomal subunit (**Figure 2.9, Table 2.4**). The high resolution cryo-EM density map enabled modeling all known modified nucleotides including the novel C8 methylation of A2503 (**Figure 2.9b**). Furthermore, comparison of the Cfr-modified ribosome with the high resolution cryo-EM structure of unmodified, wild-type *E. coli* ribosome we published previously³³ allowed us to identify with high confidence any structural changes due to the presence of m⁸A2503. Importantly, modification of A2503 by Cfr does not affect the conformation or position of the A2503 nucleotide. The adenine ring remains in the *syn*-conformation and places the newly installed C8-methyl group directly into the PTC to sterically obstruct antibiotic binding (**Figure 2.9c-d**).

Strikingly, beyond the addition of a single methyl group to the substrate nucleotide, presence of m⁸A2503 does not result in any additional structural changes to the PTC region of the ribosome (**Figure 2.9c**). Furthermore, the increased resistance provided by CfrV7 appears to be mediated specifically by improved methylation of A2503. No off-target activity of the evolved variant was observed as manual inspection did not reveal density that could correspond to additional C8-methyl adenosines within the high-resolution regions of the 50S ribosomal subunit. This result was cross-validated using our qPTxM tool³³, which identified only A2503 and A556 as possible C8-methyl adenosines. Closer examination of A556 reveals it registered as a false positive (**Figure 2.10a-d**).

Contrary to previous reports, we do not observe changes to methylation of C2498, a distal PTC nucleotide whose endogenous 2'-O-ribose modification has previously been reported to be suppressed by Cfr methylation of A2503 and hypothesized to alter the PTC through long-range effects^{7,8,56}. Although it is unclear what percentage of C2498 retains the native modification in our structure, we observe clear density for the methyl group and the nucleotide conformation is unaltered. The density for the methyl group is slightly off of the rotameric position, but the dropoff in density along the methyl bond matches the expected shape (**Figure 2.10e-g**). Together, the results do not indicate that conformational changes to C2498 are involved in Cfr-mediated resistance.

Structural superposition of the Cfr-modified ribosome with ribosomes in complex with PhLOPS_A antibiotics, hygromycin A, nucleoside analog A201A, and 16-membered macrolides enables direct identification of chemical moieties responsible for steric collision with m⁸A2503 for these eight antibiotic drug classes (**Figure 2.11, Figure 2.12**). For example, overlay of a bacterial ribosome in complex with the pleuromutilin derivative tiamulin, the selection antibiotic used during directed evolution, reveals steric clashes between the C10 and C11 substituents of the antibiotic with the Cfr-introduced methyl group (**Figure 2.9d**). The pleuromutilin class of antibiotics have recently regained interest for their applications as antimicrobial agents in humans but existing molecules remain ineffective against pathogens with Cfr⁵⁷. Given recent synthetic advances that enable more extensive modification of the pleuromutilin scaffold^{58,59}, the structural insights we obtained will inform the design of next-generation antibiotics that can overcome Cfr-mediated resistance.

Discussion

By relying on directed evolution under antibiotic selection, we identified strategies that increase the ability of a multi-antibiotic resistance determinant Cfr to cause resistance. Enhanced resistance is associated with improved *in vivo* methylation of rRNA at the C8 position of A2503. The positive correlation between extent of rRNA modification and resistance aligns with previous studies that investigated linezolid resistance caused by mutation of rRNA, where the severity of linezolid resistance was proportional to the number of 23S rRNA alleles harboring the resistance mutation⁶⁰⁻⁶². While alteration of the antibiotic binding site through mutations and enzymatic modification of 23S rRNA are functionally distinct, dependence on the extent of rRNA modification provides parallels between the two mechanisms. The results of our evolution experiment indicate that increasing the intracellular concentrations of Cfr, rather than improving catalysis of an enzyme with a complex radical mechanism^{11,39,63,64} is the preferred strategy to increase the proportion of ribosomes with the protective m⁸A2503 modification.

Investigations into expression levels of Cfr^{WT} and its respective mutants revealed that, in addition to full-length protein, a smaller Cfr isoform of ~30 kDa is also produced (**Figure 2.2b**, **Figure 2.5a**). The smaller product likely results from translation initiation at an internal start codon, as mutation of Met at position 95 abolishes its production. The sequence upstream of M95 is A-rich, which has been demonstrated to promote translation initiation⁶⁵. However, why an internal region of the Cfr ORF would be recognized as an initiation signal is unclear. Truncation of the first 38 residues of Cfr would eliminate a significant portion of the protein, including the N-terminal accessory domain which is likely involved in substrate recognition^{66,67}. Elimination of this domain provides rationale for why the smaller Cfr isoform does not contribute to resistance, as the protein would likely exhibit perturbed binding to rRNA. Thus, while the truncated product

does not contribute to resistance, the potential function of the smaller protein remains elusive and requires further study.

The evolved variants improve expression of resistance-causative, full-length Cfr using two mechanisms. Improved Cfr expression for CfrV6/7 is driven by increased transcription due to alterations to the P_{tet} promoter likely introduced by primer slippage during the error-prone PCR step of directed evolution. CfrV6 contains a full duplication of P_{tet} , providing two sites for transcription initiation, likely responsible for enhanced *cfr* transcript levels. Interestingly, this result parallels a clinical instance of high Cfr resistance discovered in a *S. epidermidis* isolate where transcription of *cfr* was driven by two promoters⁶⁸ and highlights transcriptional regulation as an important mechanism for modulating the *in vivo* activity of Cfr.

Improved expression for evolved variants CfrV1-5 is mediated by mutations that improve both translational efficiency and protein stability *in vivo*. Of the tested mutations, I26M provides the largest improvement in stability. Of note, the N-terminally truncated Cfr derived from translation initiation at I26M is rapidly degraded, as no detectable protein is observed after 60 min (**Figure 2.7e**). However, these results indicate that the costly production and clearance of this nonfunctional protein is offset by the improved cellular stability of the full-length Cfr carrying the I26M mutation. We also observe modest improvements in protein stability with N2K/I mutants. In bacteria, the identity of the N-terminal residues are important determinants of degradation through N-degron pathways^{69,70}. During protein synthesis the N-terminus is co-translationally processed by two enzymes, peptide deformylase to remove the formyl group from Met (fM) and methionine aminopeptidase⁷¹. Based on previous biochemical work, it is unlikely that CfrWT and CfrN2K/I would have differential N-termi, since fMN... and fMK/I... are likely to be efficiently de-formylated⁷² and resistant to methionine excision⁷³⁻⁷⁵. Although the precise

mechanism by which N2K/I improve Cfr stability remains elusive, these mutations may alter recognition by other enzymes important for degradation, such as endopeptidases or L/F-tRNA-protein transferase^{76,77}.

Of the mutations investigated, N2K is the largest contributor to enhanced Cfr expression and resistance. Although N2K contributes to cellular stability, our results suggest that improved Cfr translation is the dominant role of this mutation. The effect of N-terminal residues (and thus codons near the start site) on early stages of translation have been well documented. Previous work has demonstrated that minimal secondary structure near the start codon^{41,42,45,46,78} and presence of A/U-rich elements downstream of the translation start site^{65,79} are important factors for efficient translation initiation. RNA secondary structure predictions of the region proximal to the start codon suggests that the N2K mutation (AAU to AAA) could disrupt base pairing between the N2 (AAU) codon and the downstream T7 (ACA) codon. (**Figure 2.13**). However, the base pair between the 2nd and 7th codon is predicted to be retained when K2 is encoded by the AAG isocodon (**Figure 2.13**), which was also able to increase Cfr expression levels and suggests that alternative mechanisms may be responsible for improved translation. While initiation is a major rate-limiting step in protein synthesis, rates of elongation have also been demonstrated to impact translation efficiency, with several proposed models on how the interconnected factors of codon bias, mRNA structure/sequence, and interactions between the ribosome and nascent chain are involved in modulating protein synthesis⁸⁰⁻⁸². For example, recent work investigating the role of codons 3-5 identified that both mRNA sequence and amino acid composition are key determinants of proper elongation at the N-terminus⁴⁴. Although the mechanism is poorly understood, previous studies have discovered that presence of a AAA lysine codon after the start site is associated with improved translation efficiency in certain contexts⁴⁷⁻⁵¹. Our results indicate that the effect of N2K

on early steps of translation elongation may be mediated, at least in part, by tRNA abundance, but the exact impact of Lys2 on translation requires further study. Interestingly, the observed internal translation start sites (I26M, M95) that are responsible for producing Cfr truncations (**Figure 2.2b**, **Figure 2.4**) contain a lysine immediately after methionine, further highlighting the putative role for lysine codons in early steps of translation.

To date, only a few *S. aureus* Cfr variants have been reported and no mutations matching those obtained from directed evolution have been found in clinical isolates. However, enhanced expression through positioning of Lys as the second amino acid of Cfr can be recapitulated by accessing an upstream translational start site found in a native sequence context of *cfr* (**Figure 2.14**). In the specific case of the pSCFS1 resistance plasmid, the sequence upstream of the annotated start codon contains regulatory elements that have been proposed to modulate Cfr expression^{6,83}. It is plausible that in response to antibiotics, the upstream start codon is used to add three amino acids (MKE) to the N-terminus of Cfr and thus placement of a lysine (K) at position two of the newly expressed protein, analogous to the N2K mutation. Although start codon selection requires further investigation, N-terminal addition of MKE to Cfr expressed under non-native P_{tet} promoter phenocopies the N2K directed evolution mutation, resulting in increased expression and resistance compared to CfrWT (**Figure 2.14**). Since our assessment of the evolved variants indicates that an increase in Cfr expression is accompanied by a decrease in fitness (**Figure 2.2e**), start site selection in response to antibiotic pressure would mitigate detrimental impact on fitness while enabling higher resistance when acutely needed.

Interestingly, mutations obtained through directed evolution have been observed in Cfr homologues that share less than 80% sequence identity with Cfr. Specifically, methionine (M) at position 26 is observed for the functionally characterized Cfr homologues Cfr(B)⁸⁴⁻⁸⁶ and Cfr(D)⁸⁷,

which have been recovered from human-derived isolates and share 74% and 64% amino acid identity with Cfr, respectively⁸⁸ (**Figure 2.15**). We also observe lysine (K) at position 2, methionine (M) at position 26, and glycine (G) at position 39, akin to N2K, I26M, and S39G mutations, for a number of Cfr homologues that clade with functional Cfr or Cfr-like genes⁸⁹. While the precise roles of these residues within less-well characterized and more distantly related Cfr proteins requires further study, these observations indicate that directed evolution accessed sequence space that is already being exploited by proteins that are, or are hypothesized to be, functional Cfr resistance enzymes.

In addition to identifying mechanisms that increase Cfr-mediated resistance, directed evolution of Cfr also provided an indispensable reagent that enabled structural determination of the Cfr-modified ribosome. The high-resolution cryo-EM structure revealed that broad resistance is due to steric effects of the judiciously positioned methyl group within the shared binding site of PTC-targeting antibiotics. Lack of notable changes in position or orientation of A2503 or surrounding PTC nucleotides upon Cfr methylation suggests that the resulting modification does not obstruct the translation capabilities of the ribosome. This absence of PTC disruption is consistent with the observation that the fitness cost of Cfr acquisition is not due to ribosome modification, but rather results from expression of the exogenous protein²⁸. Importantly, overlay with existing structures containing PTC-targeting antibiotics provides direct visualization of chemical moieties that are sterically impacted by m⁸A2503 and will inform design of antibiotic derivatives that can overcome resistance mediated by Cfr.

Materials and Methods

E. coli strains and plasmids

E. coli ER2267 expressing Cfr from a pZA vector^{35,36} was used in directed evolution experiments. Antibiotic resistance, fitness, *in vivo* RNA methylation, and protein/transcript expression, polysome analysis, and protein degradation experiments were conducted with *E. coli* BW25113 expressing Cfr protein from a pZA vector under the P_{tet} promoter (or P_{cfr} promoter where noted). *E. coli* BW25113 *acrB::kan*, where the efflux pump *acrB* was replaced with a kanamycin cassette, was used for antibiotic susceptibility testing of the oxazolidinone antibiotic linezolid and hygromycin A. For experiments for which tagless versions of evolved Cfr variants were used, comparisons were made to the *wildtype* Cfr protein to which the original C-terminal His tag had been removed. *E. coli* Rosetta2 BL21(DE3) pLysS was used for overexpression of N-His₆-SUMO-tagged Cfrs from a pET28a vector. *E. coli* MRE600 was used for preparation of Cfr-modified ribosomes for structural studies.

Cfr mutagenesis and selection scheme

The wild-type *cfr* gene (accession: EF450709.1) with a C-terminal His₆-tag, or pooled *cfr* genes from the previous round of evolution, were randomly mutagenized by error-prone polymerase chain reaction as described previously³⁶. The mutagenized *cfr* gene pool was then recloned into a pZA vector and transformed into *E. coli* ER2267. The frequency of mutations was determined by sequencing randomly selected library variants and was on average 1-3 mutations per gene. *E. coli* transformants were then subjected to selection by plating cells on LB agar containing tiamulin (Wako Chemicals USA), in addition to 100 µg/mL ampicillin for plasmid maintenance and 20 ng/mL anhydrotetracycline (AHT, Sigma) for induction of Cfr expression. For each round of

evolution, the *E. coli* transformants were divided equally and plated on 4-5 plates of LB agar containing different concentrations of tiamulin and grown at 37°C for up to 48 h. The tiamulin concentration was increased in 50-100 µg/ml increments. For example, in the first round of evolution the transformation was plated on the 150, 200, 250 and 300 µg/ml tiamulin plates, in the last round we selected on 250, 350, 450 and 550 µg/ml tiamulin plates. Two microliters were plated on tiamulin deficient plates to determine transformation efficiency. In general, colonies isolated from tiamulin plates in which the ≤10% of the transformants grew were taken for the next round. After 5 rounds of mutagenesis and selection, 2 rounds of enrichment (selection without mutagenesis) using high tiamulin concentrations (400-1500 µg/mL) was conducted. After each round of selection or enrichment, 5-10 randomly selected colonies were sequenced from each plate.

Determination of antibiotic resistance

Antibiotic resistance experiments by broth microdilution followed established protocols⁹⁰. In brief, 2 mL of LB media with selection antibiotic was inoculated with a freshly transformed colony containing either empty plasmid, Cfr^{WT}, or Cfr mutants. Cultures were grown at 37°C with shaking for approximately 2.5 h. After measuring the OD₆₀₀ value, cultures were diluted to 10⁶ cells and 50µL of this dilution was dispensed into 96-well plates containing 50 µL of LB media with antibiotic of interest, ampicillin (100 µg/mL), and AHT (30 ng/mL). Antibiotic resistance of evolved Cfr variants were evaluated using 2-fold serial dilution of antibiotic with the following concentration ranges: tiamulin (50-6400 µg/mL, Wako Chemicals); clindamycin (50-6400 µg/mL, TCI America), chloramphenicol (0.5-64 µg/mL, AllStar Scientific), linezolid (1-256 µg/mL, Acros), hygromycin A (2-1024 µg/mL, gifted from Dr. Kim Lewis), and trimethoprim (0.125 –

0.2 µg/mL, Sigma). Chloramphenicol resistance of single Cfr mutations were evaluated using concentrations of 1, 2-12 µg/mL (in 2 µg/mL-step increments), followed by 16-64 µg/mL (2-fold dilution). The minimum inhibitory concentration (MIC) required to inhibit visible bacterial growth was determined after incubating plates at 37°C with shaking for 18 h. Plate OD₆₀₀ values were also recorded with a microtiter plate reader (SpectraMax M5, Molecular Devices). Antibiotic resistance determination on LB agar plates was conducted as described previously^{36,90}. In brief, 3 µL of 10⁸, 10⁶, and 10⁴ dilutions *E. coli* harboring Cfr were spotted on LB agar plates containing various concentrations of tiamulin. LB agar plates also contained ampicillin (100 µg/mL) and AHT (30 ng/mL). LB agar plates were incubated at 37°C for 24–48 h.

Oligo-protection of rRNA and MALDI-TOF analysis

E. coli expressing empty plasmid or Cfr were grown at 37°C to an OD₆₀₀ of 0.4-0.6 with shaking by diluting an overnight culture 1:100 into LB media containing ampicillin (100 µg/mL) and AHT inducer (30 ng/mL). Total RNA purification, oligo-protection of the 23S rRNA fragment C2480-C2520, and RNaseT1 digestion was performed as described previously^{37,38}. Mass spectra were acquired in positive ion, reflectron mode on an AXIMA Performance MALDI TOF/TOF Mass Spectrometer (Shimadzu). Relative peak intensity values were calculated using the Shimadzu Biotech MALDI-MS software.

Expression and purification of Cfr

CfrWT and CfrV4 were expressed, purified, and reconstituted using modified published protocols^{10,38}. In brief, N-His₆-SUMO-tagged CfrWT/V4 were overexpressed in minimal media conditions with 800 µM IPTG and 1,10-phenanthroline to obtain enzyme lacking a [4Fe-4S] iron-

sulfur cluster. Minimal media also contained selection antibiotics kanamycin (50 $\mu\text{g}/\text{mL}$) and chloramphenicol (34 $\mu\text{g}/\text{mL}$). All purification steps were performed in a glovebox (MBraun, oxygen content below 1.8 ppm) that was cooled to 10°C. Cfr was purified by Talon chromatography (Clontech) from clarified lysates. Following chemical reconstitution of the [4Fe-4S], the N-His₆-SUMO-tag was cleaved by incubating the fusion protein with SenP1 protease (prepared in-house, 1 mg SenP1:100 mg Cfr) for 1 h at 10°C in buffer containing 50 mM EPPS (pH 8.5), 300 mM KCl 15% glycerol, and 5 mM DTT. The cleaved protein was purified away from SenP1 and the N-His₆-SUMO-tag by FPLC on a Mono Q 10/100 GL anion exchange column (GE Healthcare Life Sciences) using buffers containing 50 mM EPPS (pH 8.5), 50 mM or 1M KCl (low-salt or high-salt), 15% glycerol, and 5 mM DTT. Protein was eluted using a linear gradient of 100% low-salt to 100% high-salt buffer over 8 column volumes. Fractions containing apo-reconstituted, tag-less Cfr were combined, concentrated using a concentrator cell (Amicon Ultra-0.5 mL, 30 MWCO), and stored at -80°C. Protein concentration was determined by Bradford assay (Bio-Rad).

Preparation of rRNA substrate

The *E. coli* 23S rRNA fragment 2447-2624 used for *in vitro* experiments was prepared using modified published protocols³⁸. The desired DNA fragment was amplified from plasmid pKK3535 using previously established primers¹⁰ and used as the template in the *in vitro* transcription reaction. Following DNase treatment and purification, RNA was precipitated overnight at -20°C by addition of 1/10th volume of 3 M NaOAc, pH 5.5 and 3 volumes of ethanol (EtOH). The RNA was then pelleted and washed with 70% aqueous EtOH, dried, and resuspended in nuclease-free water to obtain a final concentration of ~6 mg/mL. The rRNA fragment was refolded and purified

by size exclusion chromatography. To refold the RNA, the sample was heated at 95°C for 2 min and then cooled to 65°C over 5 min. MgCl₂ was subsequently added to a final concentration of 10 mM prior to a final cooling step at room temperature for at least 30 min. After removing insoluble debris, RNA was purified by FPLC on a HiLoad 26/60 Superdex 200 column (GE Healthcare Life Sciences) using buffer containing 50 mM HEPES (pH 7.5), 10 mM MgCl₂, and 50 mM KCl. Fractions containing the desired rRNA product were combined and precipitated overnight at -20°C by addition of 1/10th volume of 3 M NaOAc, pH 5.5 and 3 volumes of EtOH. The RNA was then pelleted and washed with ice-cold 80% aqueous EtOH, dried, and resuspended in nuclease-free water. After confirming RNA purity on a denaturing 5% TBE, 7M Urea-PAGE gel, the RNA sample was concentrated to ~450 mM using a SpeedVac Vacuum Concentrator prior to storage at -80°C.

Cfr Kinetic Assay

Methylation activity of Cfr^{WT} and Cfr^{V4} were assessed by monitoring radioactivity incorporation into RNA. Flavodoxin and flavodoxin reductase enzymes were prepared as described previously⁶³. Prior to assembling reaction components, the RNA substrate was refolded as described above. Reactions were conducted in 52 µL volumes in an anaerobic chamber (MBraun, oxygen levels less than 1.8 ppm) under the following conditions: 100 mM HEPES (pH 8.0), 100 mM KCl, 10 mM MgCl₂, 2 mM DTT, 50 µM Flavodoxin, 25 µM Flavodoxin reductase, 100 µM rRNA substrate, 2 mM [³H-methyl] S-adenosylmethionine (175.8 dpm/pmol), and 5 µM apo-reconstituted Cfr. Reactions were equilibrated at 37°C for 5 min and subsequently initiated by addition of NADPH (Sigma, final concentration 2 mM). The reaction was allowed to proceed at 37°C and timepoints at 0, 2, 4, 6, and 8 min of 10 µL volume were quenched by the addition of H₂SO₄ (50 mM final

concentration). For each timepoint, the RNA volume was brought up to 100 μ L with nuclease-free water and was purified away from other reaction components by an RNA Clean & Concentrator kit (Zymo Research) by following the manufacturer's instructions. Purified RNA eluate was added to Ultima Gold scintillation fluid, and the total amount of radioactivity incorporated in the product was detected using a Beckman-Coulter LS6500 scintillation counter. Amount of product generated at each time point was calculated by subtracting background radioactivity ($t=0$ min) and considering that 2 of the 3 tritium atoms from [3 H-methyl] *S*-adenosylmethionine would be incorporated into the final methylated RNA product^{11,39}.

Evaluation of Cfr protein expression by quantitative western blot

E. coli expressing empty plasmid, CfrWT, or Cfr mutants were grown at 37°C to an OD₆₀₀ of ~0.4 with shaking by diluting an overnight culture 1:100 into 10 mL LB media containing ampicillin (100 μ g/mL) and AHT inducer (30 ng/mL). Cells were harvested by centrifugation. Cell pellets were lysed for 15 min using B-PER Bacterial Protein Extraction Reagent (Thermo Scientific) containing DNase I (New England Biolabs) and 1X cOmplete, EDTA-free protease inhibitor cocktail (Roche). Whole cell lysate samples containing 4 μ g of protein were fractionated using a 4–20% SDS-PAGE gel (Bio-Rad). Proteins were transferred to a 0.2 μ m nitrocellulose membrane using a Trans-Blot Turbo transfer system (Bio-Rad) with a 7 min, mixed MW protocol. Membranes were incubated with TBST-Blotto buffer (50 mM Tris-pH 7.5, 150 mM NaCl, 0.1% Tween-20, 5% w/v Bio-Rad Blotting Grade Blocker) for 1 h at room temperature, followed by TBST-Blotto containing two primary antibodies: monoclonal mouse anti-FLAG M2 (1:2,000 dilution, Sigma) and monoclonal rabbit anti-RNA polymerase beta (1:2,000 dilution, Abcam) for 1 h at room temperature. After washing 3 x 5 min with TBST, membranes were then incubated

overnight at 4°C with TBST-Blotto containing two secondary antibodies: goat anti-rabbit IgG cross-absorbed DyLight 680 (1:10,000 dilution, Thermo) and goat anti-mouse IgG cross-absorbed IRDye 800CW (1:10,000 dilution, Abcam). Membranes were rinsed 3 x 5 min with TBST and allowed to dry completely prior imaging using a Bio-Rad ChemiDoc Molecular Imager. Quantification was performed using Image Lab Software (Bio-Rad) within the linear range of detection. The house-keeping protein RNA polymerase beta, which was stably expressed in all experimental conditions, was used as an internal loading control.

Determination of E. coli growth rate

E. coli expressing empty plasmid, CfrWT, or Cfr variants were grown at 37°C with shaking by diluting 50 µL of an overnight culture into 10 mL of LB media containing ampicillin (100 µg/mL) and AHT inducer (30 ng/mL). OD₆₀₀ values were recorded every 20 min with a microtiter plate reader (SpectraMax M5, Molecular Devices).

qPCR Primer Design

qPCR primer sequences for *cfr*, *recA*, and *luc* were designed using NCBI Primer Blast. Template accession numbers, amplicon length, and primer sequences are described in **Table 2.5**. Primer sequences for *rrsA* were used as published previously⁹¹.

Determination of Cfr mRNA expression by RT-qPCR

Bacterial growth. *E. coli* expressing empty plasmid control, CfrWT, or Cfr variants were grown at 37°C with shaking by diluting an overnight culture 1:100 into 5 mL of LB media containing ampicillin (100 µg/mL) and AHT inducer (30 ng/mL). When cells reached an OD₆₀₀ of ~ 0.4,

RNAprotect Bacteria Reagent (Qiagen) was added to the culture following manufacturer's instructions. Cells were then harvested by centrifugation for 10 min at 5000 x g at 4°C and frozen on dry ice.

Total RNA isolation and DNase treatment. Pellets were then thawed and resuspended in 200 µL of lysis buffer containing 30 mM Tris-HCl (pH 8.0), 0.1 mM EDTA, 15 mg/mL lysozyme, and Proteinase K (New England Biolabs). Following lysis for 10 min at room temperature, total RNA was isolated using a RNeasy mini kit (QIAGEN) following the manufacturer's instructions. Yield and purity of isolated RNA was assessed by NanoDrop UV spectrophotometer (Thermo). RNA integrity was assessed by performing 1% TBE agarose gel electrophoresis with samples that had been boiled for 95°C for 5 min in RNA loading dye (New England Biolabs). Genomic DNA was eliminated by incubating 2 µg of RNA with 2 U of RQ1 RNase-free DNase I (Promega) for 30 min at 30°C. The DNase reaction was halted by the addition of RQ1 Stop Solution (Promega) and incubation for 10 min at 65° C.

cDNA synthesis. Reverse transcription was performed using the iScript cDNA Synthesis Kit (Bio-Rad) following the manufacturer's instructions with 10-fold diluted DNase-treated RNA. In brief, reactions of 20 µL volume were prepared by combining 4 µL 5X iScript buffer, 1 µL iScript RNase H+ MMLV reverse transcriptase, 11 µL nuclease-free water, and 4 µL of RNA. Reactions were incubated for 5 min at 25 °C, followed by 20 min at 42 °C and 1 min at 95 °C. If not used immediately, cDNA was stored at -20°C.

RT-qPCR. SsoAdvanced Universal SYBR Green Supermix (Bio-Rad) was used for 10 µL qPCR reactions. Each reaction contained 5 µL of 2X Supermix, 0.3 µM of each forward and reverse primer, and 4 µL of diluted cDNA. The cDNA was diluted 40-fold for reactions with *cfr* primers and 4,000-fold for reactions *rrsA* primers. Reactions were prepared in a 96-well PCR Plate (Bio-

Rad, MLL9601) and run on a Bio-Rad CFX qPCR Machine. The thermal cycling conditions were as follows: 98°C for 30 s, followed by 35 cycles of 98°C for 10 s and 60°C for 45 s with plate read, ending with melt curve analysis using 5s, 0.5 °C increment steps from 65 °C to 95 °C. A no template control and no reverse transcription control were included on each plate for each primer pair. Cq values were determined using CFX Maestro Software using a single threshold method. For each sample, the average of three triplicate Cq values was used for further analysis. Relative transcript expression was calculated using the Pfaffl method⁹². Expression was normalized to *rrsA* transcripts which is stably expressed in *E. coli* BW25113⁹¹ and across our experimental conditions.

Polysome analysis

Lysate preparation and sucrose gradient fractionation were adapted from previously published protocols with modification^{52,93}.

Lysate preparation. *E. coli* expressing empty plasmid control, CfrWT, or Cfr mutants were grown at 37°C with shaking by diluting an overnight culture 1:100 into 400 mL of LB media containing ampicillin (100 µg/mL) and AHT inducer (30 ng/mL). Cells were harvested at an OD₆₀₀ ~0.4-0.5 in 200 mL batches by rapid filtration at 37°C followed by flash freezing in liquid nitrogen as described previously⁵². Each frozen cell pellet was combined with 650 µL lysis buffer as frozen droplets containing 20 mM Tris (pH 8.0), 10 mM MgCl₂, 100 mM NH₄Cl, 5 mM CaCl₂, 0.4% Triton X-100, 0.1% NP-40, 100 U/ml RNase-free DNase I (Roche), and 10 U/mL SUPERase-In (Invitrogen). Cells with lysis buffer were pulverized in a 10 mL jar containing a 12 mm grinding ball using a TissueLyser II (QIAGEN) by performing 5 rounds of 3 min at 15 Hz. Canisters were pre-chilled by submersion in liquid nitrogen for at least 1 min prior to each round of pulverization.

Lysates were recovered from the frozen jars using a spatula pre-chilled in liquid nitrogen and stored at -80°C until further use.

Sucrose Gradient Fractionation. Pulverized lysates were thawed at 30°C for 2 min followed by an ice-water bath for 20 min. Lysates were clarified by centrifugation at 20,000 x g for 10 min at 4°C. The RNA concentration of the clarified lysate was measured by NanoDrop UV spectrophotometer (Thermo) and diluted to 2.5 mg/mL with lysis buffer. Ribosome and mRNA components were separated on a linear, 12 mL, 10-55% (w/v) sucrose gradient containing 20 mM Tris (pH 8.0), 10 mM MgCl₂, 100 mM NH₄Cl, 2 mM DTT, and 10 U/mL SUPERase-In. Sucrose gradients were generated using a Bio-Comp Gradient Master with the following program: Time = 1:58 s; Angle = 81.5°, Speed = 16 rpm. For each biological sample, 190 µL (~0.5 mg RNA) of clarified lysate was loaded onto sucrose gradients in duplicate. Ultracentrifugation was performed using a SW Ti41 rotor (Beckman Coulter) for 201,000 x g for 2.5 h at 4°C. Gradients were fractionated using a Bio-Comp Fractionator in 20 fractions at a speed of 0.25 mm/sec where absorbance at 260 nm was continuously monitored.

RNA Extraction and DNase Treatment. Fractions 1+2, 3+4, 16+17, and 18+19 were combined. RNA was extracted from uniform volumes of each fraction or combination of fractions. RNA extraction was performed by adding one volume of TRIzol reagent (Invitrogen), mixing until homogeneous, and incubating at room temperature for 5 min. Samples were then incubated at room temperature for another 5 min following the addition of 0.4 volumes of chloroform. After centrifugation for 15 min at 12,000 x g at 4°C, the aqueous supernatant was transferred to a new tube to which 250 pg of a luciferase control RNA spike-in (luc, Promega). RNA was precipitated overnight at -20°C by the addition of 1 volume of isopropanol and 2 µL of GlycoBlue (15 mg/mL, Invitrogen). RNA was pelleted by centrifugation, washed twice with 75% ice-cold, aqueous

ethanol, and allowed to dry at room temperature for ~30 min. The RNA was then resuspended in 20 μ L of nuclease-free water. RNA quality and concentration were assessed by a NanoDrop UV spectrophotometer (Thermo). Genomic DNA was eliminated by incubating 10 μ L of isolated RNA with 1 U of RQ1 RNase-free DNase I (Promega) for 30 min at 30°C. The DNase reaction was halted by the addition of RQ1 Stop Solution (Promega) and incubation for 10 min at 65°C.

cDNA synthesis and RT-qPCR. Reverse transcription was performed using the iScript cDNA Synthesis Kit (Bio-Rad) following the manufacturer's instructions. In brief, reactions of 20 μ L volume were prepared by combining 4 μ L 5X iScript buffer, 1 μ L iScript RNase H⁺ MMLV reverse transcriptase, 5 μ L nuclease-free water, and 10 μ L of DNase-treated RNA. Reactions were incubated for 5 min at 25 °C, followed by 20 min at 42 °C and 1 min at 95 °C. SsoAdvanced Universal SYBR Green Supermix (Bio-Rad) was used for 10 μ l qPCR reactions in a 96-well plate as described above. Each reaction contained 5 μ L of 2X Supermix, 0.3 μ M of each forward and reverse primer, and 4 μ L of 10-fold diluted cDNA. Reactions containing cfr, recA, and luc primers (**Table 2.5**) were performed for each fraction, including a no template control and no reverse transcription control for each primer set on each plate. The average of three triplicate C_q values was used for further analysis.

Data Analysis. Normalized mRNA distribution profiles for the target mRNAs were calculated as described previously⁹⁴. In brief, the relative abundance of each target mRNA normalized to luciferase RNA spike-in. The percentage of target mRNA found across gradient fractions was calculated by dividing the amount of target mRNA detected in one fraction by the sum of the target mRNA detected in all fractions.

Protein Degradation Assay

Bacterial growth and rifampicin treatment. *E. coli* expressing CfrWT or Cfr mutants were grown at 37°C with shaking by diluting an overnight culture 1:100 into 25 mL of LB media containing ampicillin (100 µg/mL) and AHT inducer (30 ng/mL). When cells reached an OD₆₀₀ ~0.4-0.5, rifampicin (Sigma) was subsequently added to a final concentration of 100 µg/mL, and cultures were allowed continued incubation at 37°C with shaking. Timepoints at 0, 20, 40, 60, 80, 100 min were harvested by centrifuging 3 mL of the culture at 8,000 rpm at 4°C for 10 min, decanting the supernatant, and immediately flash-freezing the pellet in liquid nitrogen. Cell pellets for each time point were lysed using B-PER Bacterial Protein Extraction Reagent as described above.

Western blot. Whole cell lysate samples containing 5 µg of protein were fractionated on a 4-20% SDS-PAGE gel and transferred onto a 0.2 µm nitrocellulose membrane as described above. Membranes were stained with Ponceau S stain (0.1% w/v Ponceau S, 5% v/v acetic acid) and imaged using a Bio-Rad ChemiDoc Molecular Imager. After blocking in TBST-Blotto buffer for 1 h at room temperature, membranes were incubated with TBST-Blotto containing primary monoclonal mouse anti-FLAG M2 antibody (1:2,000 dilution, Sigma) or monoclonal mouse anti-GAPDH antibody (1:2,000 dilution, Abcam) for 1 h at room temperature. After washing 3 x 5 min with TBST, membranes were incubated overnight at 4°C with TBST-Blotto containing a secondary antibody, goat anti-mouse cross-absorbed IRDye 800CW (1:10,000 dilution, Abcam). Membranes were rinsed and imaged as described above.

Purification of Cfr-modified E. coli ribosome

Cfr-modified, 70S ribosomal subunit was purified from *E. coli* MRE600 expressing CfrV7 variant using previously published protocol with modification^{33,95}. In short, *E. coli* transformed with pZA-

encoded CfrV7 were grown to an OD₆₀₀ of 0.5 in LB media containing ampicillin (100 µg/mL) and AHT inducer (30 ng/mL) at 37°C with shaking. Cells were harvested by centrifugation, washed, and lysed by using a microfluidizer. The lysate was clarified by ultracentrifugation at 30,000 x g 30 min at 4°C using a Ti45 rotor (Beckman Coulter) twice. The recovered supernatant was applied to a 32 % w/v sucrose cushion in buffer containing 20 mM HEPES-KOH (pH 7.5), 500 mM NH₄Cl, 20 mM Mg(OAc)₂, 0.5 mM EDTA, 6 mM β-mercaptoethanol, 10 U/mL SuperASE-In and was ultracentrifuged at 100,000 x g for 16 h at 4 °C in a SW Ti41 rotor (Beckman Coulter). After removing the supernatant, the pellet was resuspended slowly at 4°C over 1 h in Buffer A containing 20 mM HEPES-KOH (pH 7.5), 200 mM NH₄Cl, 20 mM Mg(OAc)₂, 0.1 mM EDTA, 6 mM β-mercaptoethanol, 10 U/mL SuperASE-In. Particulates that were not resuspended were removed by centrifugation at 10,000 rpm for 10 min at 4°C. Sample concentration was determined by NanoDrop UV spectrophotometer (Thermo), where A₂₆₀=1 corresponds to 24 pmol of 70S ribosome. Tight-coupled 70S ribosomes were purified as described previously⁹⁶. In brief, 70S ribosomes were purified on a 15-30% w/v sucrose gradient in Buffer A. Sucrose gradients were generated using a Bio-Comp Gradient Master. 300-400 pmol of 70S ribosomes were loaded on each sucrose gradient. Ultracentrifugation was performed using a SW Ti41 rotor (Beckman Coulter) for 75,416 x g for 16 h at 4°C. Gradients were fractionated using a Bio-Comp Fractionator in 20 fractions at a speed of 0.25 mm/sec where absorbance at 260 nm was continuously monitored. Fractions corresponding to 70S ribosomes were combined and precipitated by slow addition at 4°C of PEG 20,000 in Buffer A to a final concentration of 9% w/v. Ribosomes were isolated by centrifugation for 10 min at 17,500 x g. After removing the supernatant, ribosomes were slowly resuspended overnight at 4°C in buffer containing 50 mM HEPES-KOH (pH 7.5), 150 mM KOAc, 20 mM Mg(OAc)₂, 7 mM β-mercaptoethanol, 20 U/mL SuperASE-In.

Cryo-EM analysis

Purified 70S ribosomal subunits were diluted from 2 to 0.5 mg/ml in Buffer A, applied to 300-mesh carbon coated (2nm thickness) holey carbon Quantifoil 2/2 grids (Quantifoil Micro Tools) and flash-frozen as described in⁹⁷. Data were collected using serialEM on the in-house Titan Krios X-FEG instrument (Thermo Fisher Scientific) operating at an acceleration voltage of 300 kV and a nominal underfocus of $\Delta z = 0.2$ to $1.5 \mu\text{m}$ at a nominal magnification of 29 000 (calibrated physical pixel size of 0.822 \AA). We recorded 2055 movies using a K2 direct electron detector camera in super-resolution mode with dose fractionation (80 individual frames were collected, starting from the first one). Total exposure time was 8 s, with the total dose of 80 e- (or 1 e-/ $\text{\AA}^2/\text{frame}$). Images in the stack were aligned using the whole-image motion correction and patch motion correction (5×5 patches) methods in MotionCor2⁹⁸. Before image processing, all micrographs were checked for quality and 1531 best were selected for the next step of image processing. The contrast transfer function of each image was determined using GCTF⁹⁹ as a standalone program. For particle selection we have used Relion 3.0 autopicking procedure¹⁰⁰. For the first steps of image processing, we used data binned by a factor of 8 (C8 images). During the first round of 2D classification we removed only images with ice or other contaminants. Subsequently, the initial structure was generated using the *ab initio* procedure in CryoSPARC v2.0. Following this step, we performed Relion 3D classification with bin by four data (C4) to exclude bad particles. The resulting 141 549 particle images of ribosomes were used for subsequent classification and refinement procedures. For the initial refinement we used a spherical mask, which was followed by further refinement using a mask around the stable part of 50S (excluding L1 stalk, L7/L12 region). A further improved cryo-EM map was obtained by using CTF-refinement procedure from Relion 3.0. The post-processing procedure implemented in Relion

3.0¹⁰⁰ was applied to the final maps with appropriate masking, B-factor sharpening (automatic B-factor estimation was -55.86) and resolution estimation to avoid over-fitting (final resolution after post-processing with 50S mask applied was 2.7 Å). Subsequently the stack of CTF-refined particles was processed in a new version of CryoSPARC v2.0¹⁰¹. After homogeneous refinement the same stack of particles was additionally refined in cisTEM¹⁰². After Auto-Refine (with automasking within cisTEM) we performed local refinement using 50S mask (the same one used for refinement in Relion) and also applied per particle CTF refinement as implemented in cisTEM software. After such refinement the resolution was improved to 2.2. This map after Sharpen3D¹⁰² was used for model building and map interpretation.

Atomic model building and refinement

The final model of the 50S subunit was generated by multiple rounds of model building in Coot¹⁰³ and subsequent refinement in PHENIX¹⁰⁴. The restraints for the novel m²m⁸A nucleotide for the atomic model fitting and refinements were generated using eLBOW¹⁰⁵. The atomic model of the 50S subunit from the *E. coli* ribosome structure (PDB 6PJ6)³³ was used as a starting point and refined against the experimental cryo-EM map by iterative manual model building and restrained parameter-refinement protocol (real-space refinement, positional refinement, and simulated annealing). Final atomic model comprised of ~92 736 atoms (excluding hydrogens) across the 3015 nucleotides and 3222 amino acids of 28 ribosomal proteins. Proteins L7, L10, L11 and L31 were not modelled in. In addition, 179 Mg²⁺, 2716 water molecules, one Zn²⁺ and one Na⁺ were included in the final model. Prior to running MolProbity¹⁰⁶ analysis, nucleotides 878–898, 1052–1110, 2101–2189 of 23S rRNA, and ribosomal protein L9 were removed, due to their high degree of disorder. Overall, protein residues and nucleotides show well-refined geometrical parameters

(Table 2.4). Figures were prepared using Pymol Molecular Graphics System, Version 2.4.1 unless otherwise noted.

qPTxM analysis of post-transcriptional modifications

The final model and map were run through qPTxM³³ with default parameters except for `d_min=2` and `cc_threshold=0.5` to search for evidence of posttranscriptional modifications. Of a total of 39 sites with density suggesting possible modifications, two were C8-methyl adenosines, A556 and A2503. None of the identified sites were 2'O-methyl cytosines. To calculate expected density dropoff curves for methylated and unmethylated nucleotides, the *phenix.fmodel*¹⁰⁴ tool was used to generate noise-free maps from models of a single nucleotide in each state, and scripts modified from qPTxM were used to collect measurements of the density at 0.1 Å intervals along the vector of the proposed methylation. Means and standard deviations were calculated for densities at the four positions tested by qPTxM on each nucleotide, from which Z-scores were then calculated for selected nucleotides. To measure densities for both the best tested rotamer of m(2'O)C 2498 and the modeled rotamer, densities along the 2'O-methyl bond were compared between the files generated by qPTxM run twice as described above, once with `prune=True` (removing the modeled methyl group and placing the rotameric methyl with the strongest density) and once with `prune=False` (leaving the modeled methyl group intact).

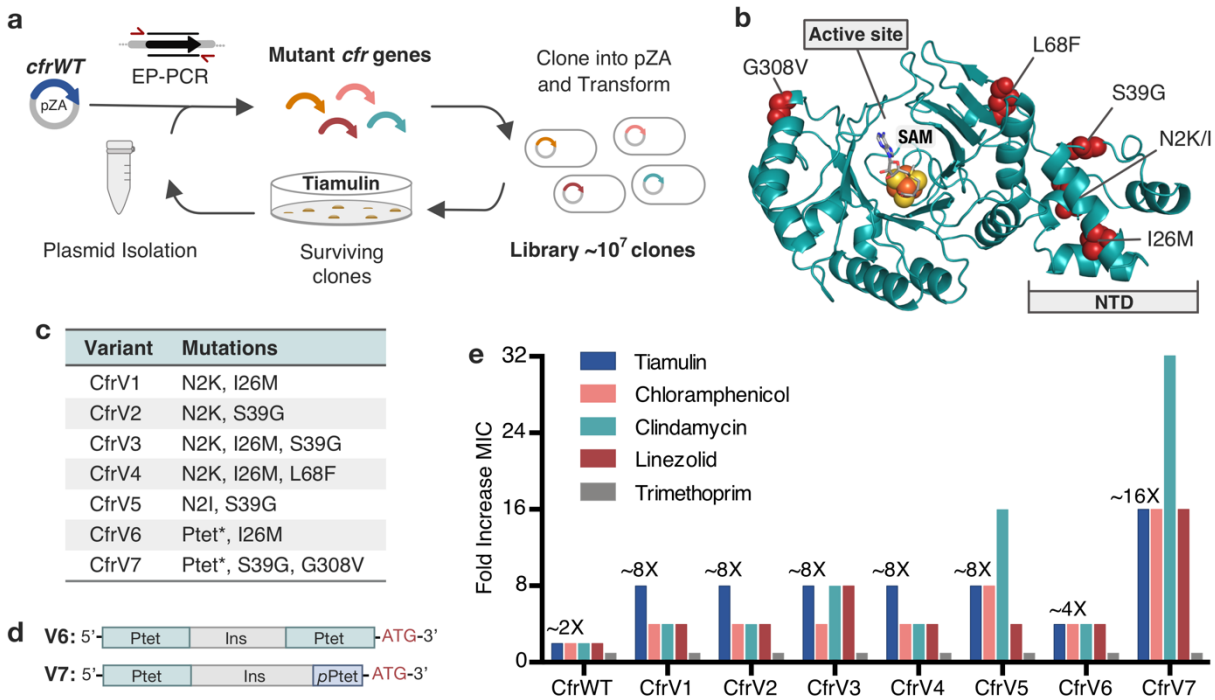


Figure 2.1 | Evolved variants of Cfr confer increased antibiotic resistance. (a) Evolution of Cfr under selection by the PTC-targeting antibiotic tiamulin. (b) Cfr homology model based on RlmN generated by I-TASSER server¹⁰⁷ with mutagenic hotspots in red. N-terminal domain (NTD) is labeled. Active site denoted by S-adenosylmethionine (SAM, grey) and [4Fe-4S] cluster (orange). (c) Evolved variants containing Cfr mutations selected for further study. Ptet* indicates alterations to promoter sequence. (d) Promoter architecture of CfrV6 and CfrV7 where pPtet designates a partial Ptet promoter sequence and Ins designates a variable insertion sequence. (e) Fold improvement in MIC resistance value for PhLOPS_A antibiotics and trimethoprim compared to empty pZA vector control determined from three biological replicates by microbroth dilution method. Trimethoprim is a negative control antibiotic that does not target the ribosome. LZD testing was performed against *E. coli* BW25113 lacking efflux pump, *acrB*.

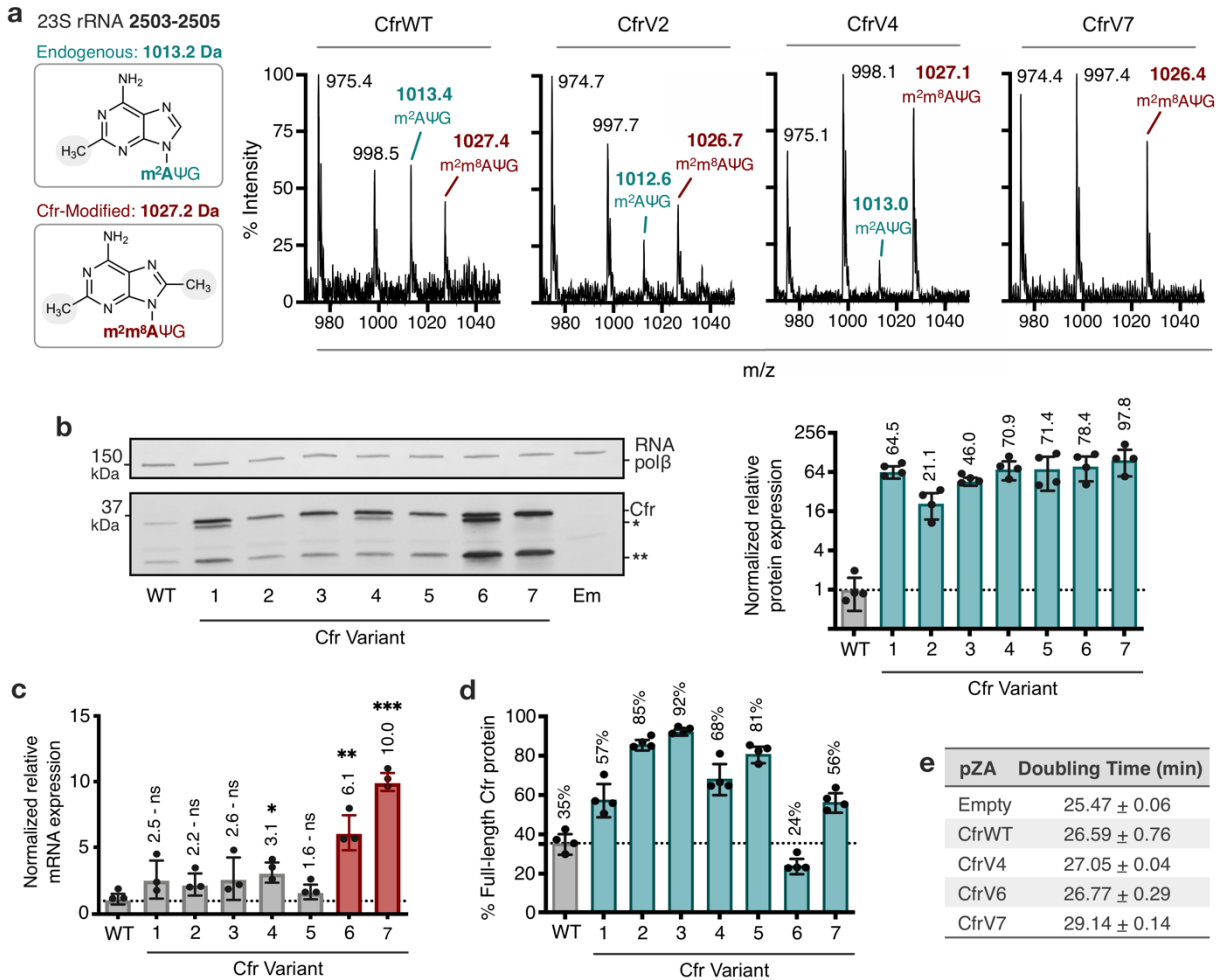


Figure 2.2 | Cfr variants cause increased methylation of 23S rRNA at A2503. (a) Endogenously modified (m^2A_{2503}) and Cfr-hypermodified ($m^2m^8A_{2503}$) rRNA fragments correspond to m/z values of 1013 and 1027, respectively. MALDI-TOF mass spectra of 23S rRNA fragments isolated from *E. coli* expressing CfrWT, and evolved Cfr variants V2, V4, and V7. Ψ is pseudouridine, m^2A is 2-methyladenosine, m^2m^8A is 2,8-dimethyladenosine. (b) Relative protein expression of full-length Cfr variants compared to full-length CfrWT detected by immunoblotting against a C-terminal FLAG tag and quantification of top Cfr bands. Signal was normalized to housekeeping protein RNA polymerase β -subunit. Data is presented as the average of four biological replicates with standard deviation on a \log_2 axis. Asterisks denote N-terminally truncated versions of Cfr that do not contribute to resistance. Em = empty vector control. (c) Relative transcript levels for variants compared to CfrWT determined from three biological replicates with standard deviation. Statistical analysis was performed using a two-tailed t-test on \log_2 transformed data. (d) Percentage of total Cfr expression attributed to production of full-length Cfr protein, presented as the average of four biological replicates with standard deviation. (e) Doubling times for *E. coli* expressing empty plasmid, CfrWT, or Cfr variants determined from three biological replicates with standard error.

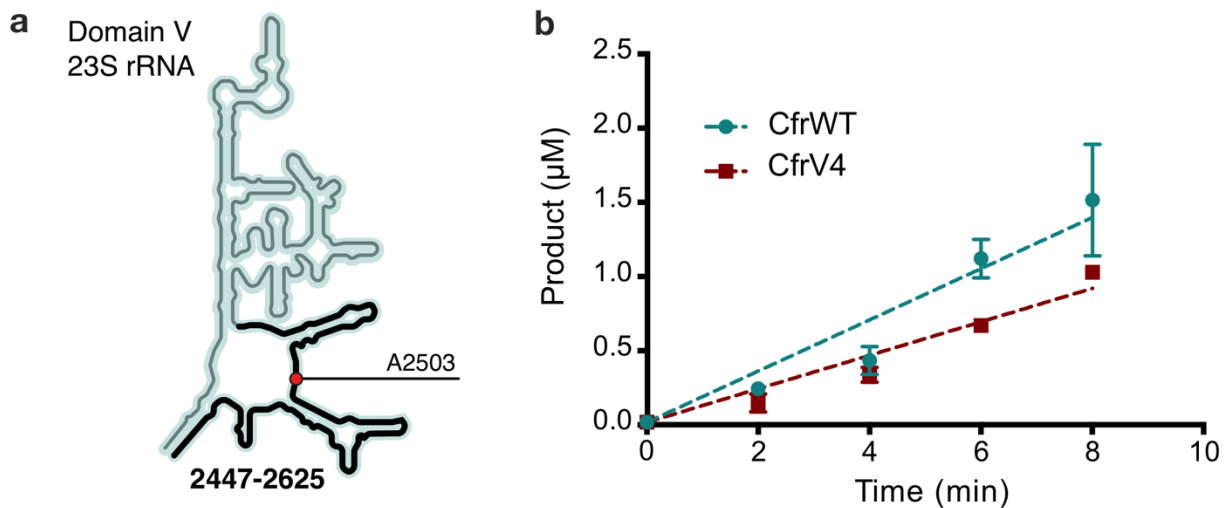


Figure 2.3 | *In vitro* characterization of CfrWT and CfrV4. (a) Schematic representation of 23S rRNA domain V secondary structure highlighting the rRNA fragment 2447-2625 used in the kinetic assay. Position of the Cfr substrate nucleotide A2503 is indicated by a red circle. (b) Time-dependent formation of methylated rRNA product by CfrWT or evolved CfrV4 in reactions containing 5 μM apo-reconstituted Cfr enzyme, 100 μM 23S rRNA fragment 2447-2625, and 2 mM [^3H -methyl] S-adenosylmethionine. Values are presented as the average and standard error of two replicates. Turnover numbers for CfrWT and CfrV4 are $3.45 \times 10^{-2} \pm 3.2 \times 10^{-3} \text{ min}^{-1}$ and $2.25 \times 10^{-2} \pm 1.3 \times 10^{-3} \text{ min}^{-1}$, respectively.

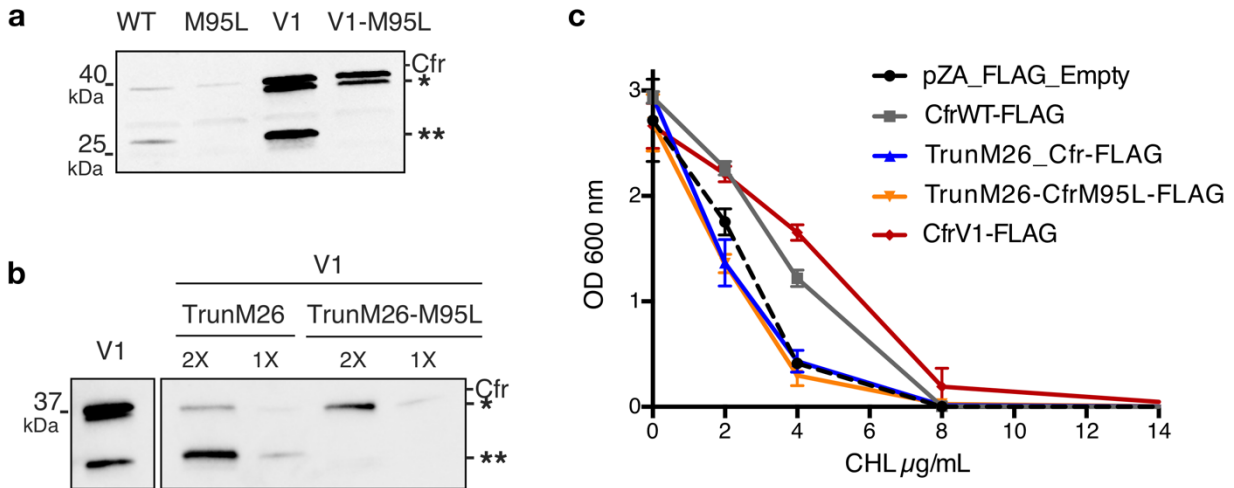


Figure 2.4 | N-terminally truncated Cfr products do not contribute to resistance. (a) Detection of Cfr protein products by immunoblotting against C-terminal FLAG tag. Directed evolution mutation I26M is sufficient to produce the higher-molecular weight truncated species (denoted by *). Mutation of M95L (AUG \rightarrow CUG) abolishes production of smaller truncated species (denoted by **). Blot is representative of two biological replicates. (b) Detection of Cfr protein products by immunoblotting against C-terminal FLAG tag with ANTI-FLAG M2-Peroxidase antibody (Sigma). TrunM26 refers to a Cfr construct where amino acids 1-25 have been eliminated. This construct yields predominately species **, with * as the minor expressed protein. TrunM26-M95L eliminates amino acids 1-25 and also removes internal Met start site through M95L mutations, yielding species *. (c) Dose-dependent growth inhibition of *E. coli* expressing N-terminally truncated Cfrs in the presence of chloramphenicol (CHL). Results presented as the average of two biological replicates with standard error.

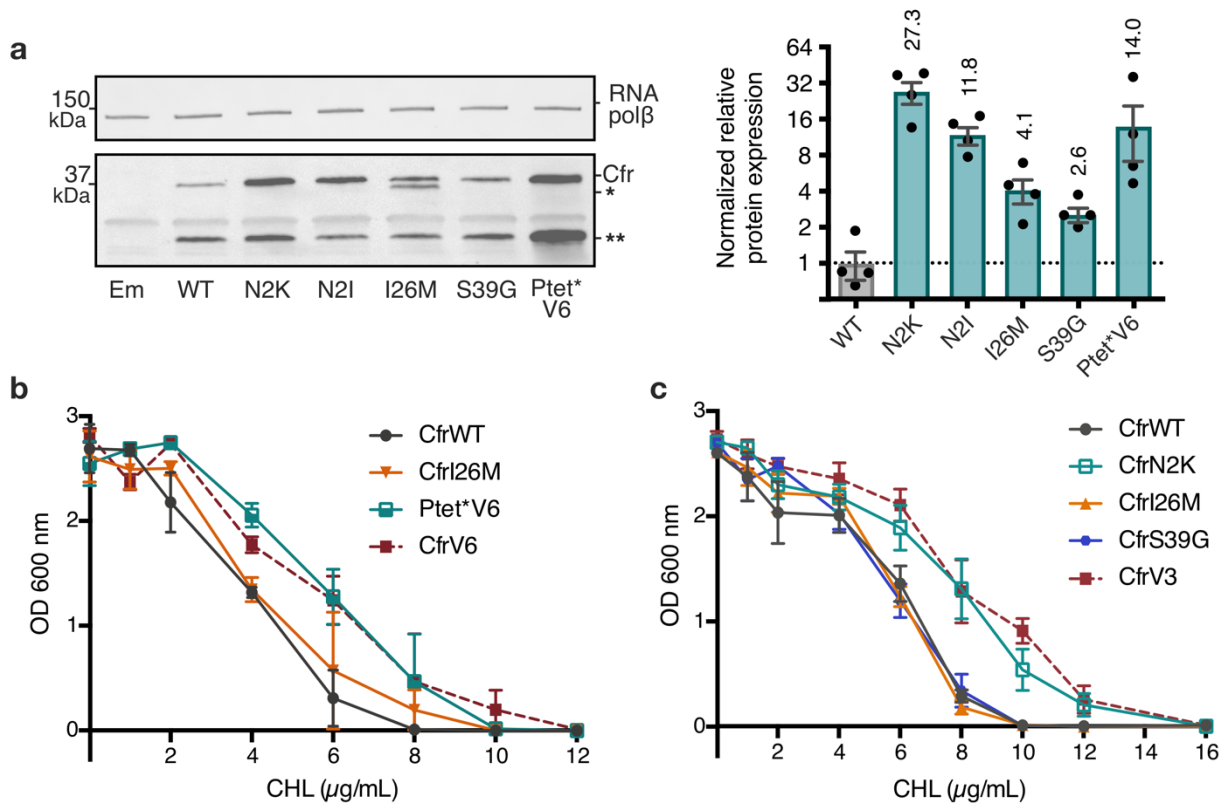


Figure 2.5 | Mutations to the second amino acid and promoter are the largest contributors to Cfr expression and resistance. (a) Effect of Cfr mutations and promoter alteration on relative Cfr protein expression was assessed by immunoblotting against a C-terminal FLAG tag. Quantification was performed for full-length Cfr protein normalized to housekeeping protein RNA polymerase β -subunit. Data is presented as the average of four biological replicates with standard deviation on a log₂ axis. Asterisks denote N-terminally truncated Cfr protein products that do not contribute to resistance and were not included in quantification. Em = empty vector control. (b) and (c) Dose-dependent growth inhibition of *E. coli* expressing pZA-encoded CfrWT, CfrV6 (panel b), CfrV3 (panel c) and individual mutants that comprise these variants towards chloramphenicol (CHL) presented as an average of three biological replicates with standard error.

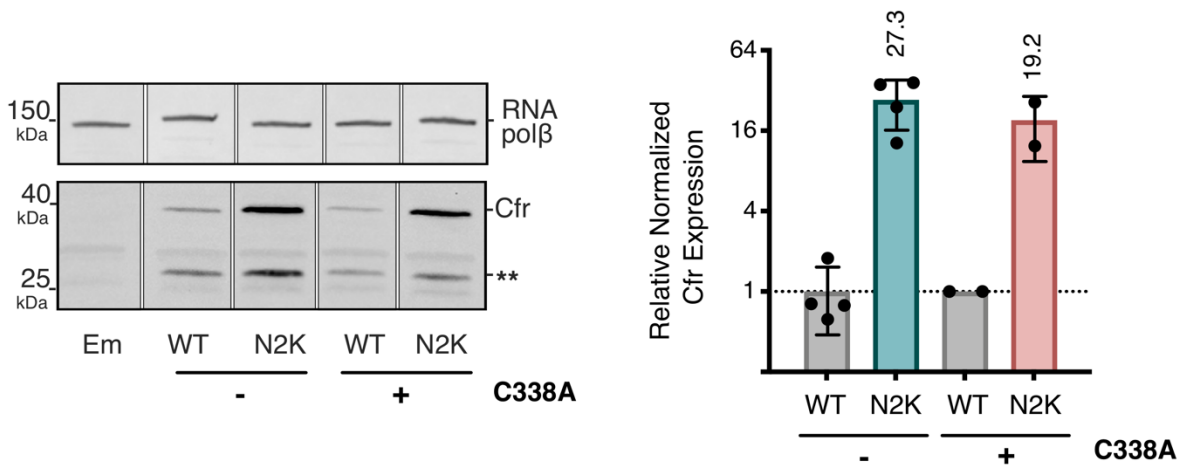


Figure 2.6 | Cfr modification of the ribosome does not impact expression of CfrN2K. Relative expression of CfrN2K compared to CfrWT, in the presence or absence of an additional C338A mutation that renders Cfr catalytically inactive. Therefore, in constructs carrying the C338A mutation, Cfr constructs are produced by ribosomes that lack the m⁸A2503 modification. Signal of full-length Cfr protein was normalized to housekeeping protein RNA polymerase β -subunit, presenting the average of two biological replicates and standard deviation on a log₂ axis. Asterisks denote truncated Cfr products that do not contribute to resistance and were not included in quantification. (c) Original, uncropped image of panel (a). Em = empty vector control.

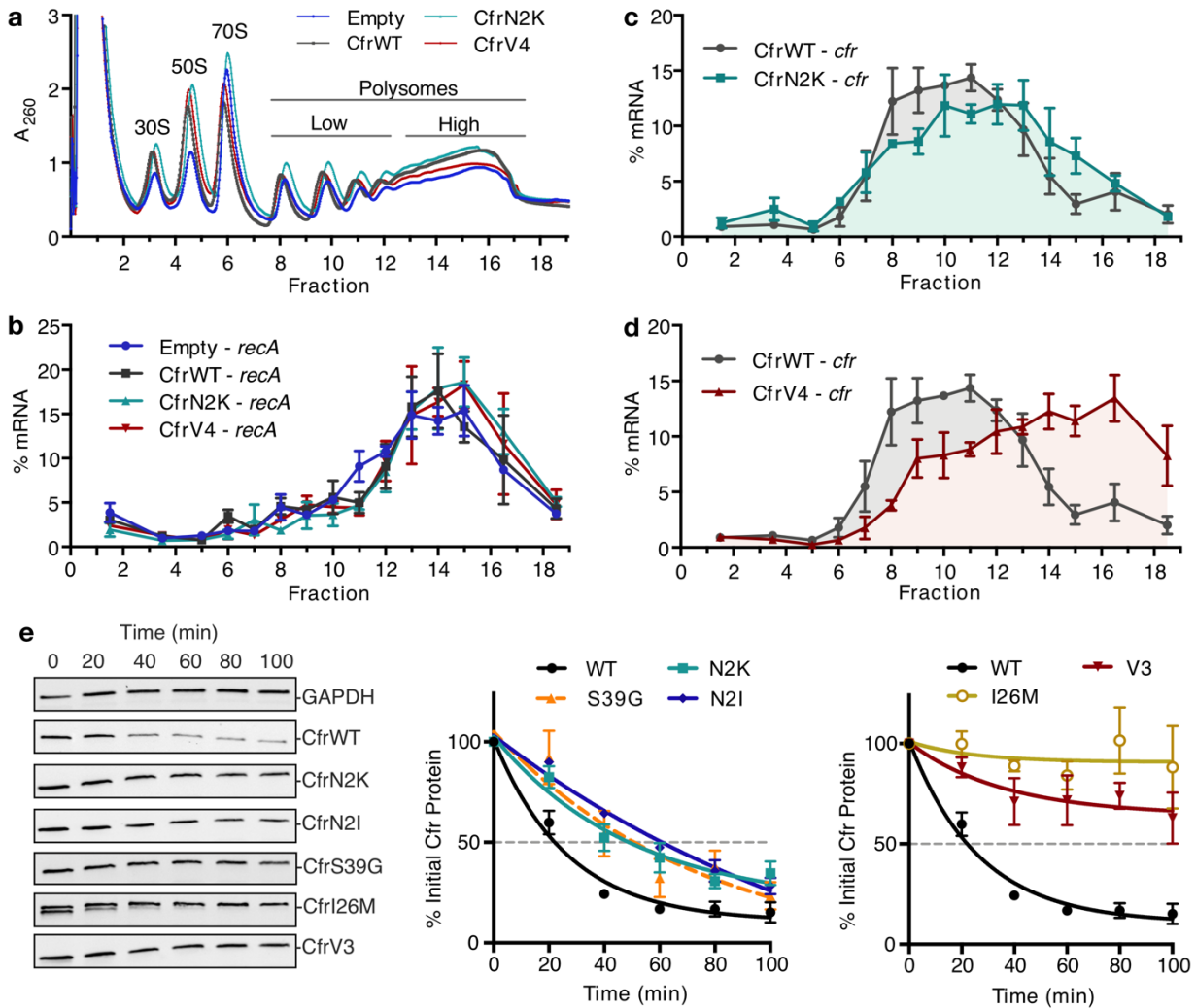


Figure 2.7 | Directed evolution mutations impact Cfr translation and degradation. (a) Sucrose gradient fractionation of polysomes from *E. coli* expressing empty vector or CfrWT/N2K/V4 denoting fractions corresponding to low- and high-density polysomes. (b) mRNA distribution of well-translated, housekeeping gene *recA* across polysome profiles. (c) mRNA distribution of Cfr transcripts expressing CfrWT or CfrN2K. (d) mRNA distribution of Cfr transcripts expressing CfrWT or CfrV4. For B-D, transcript levels for each fraction were determined by RT-qPCR and normalized by a luciferase mRNA control spike-in. Values presented as the average of three biological replicates with standard error. (e) Protein degradation kinetics of CfrWT, single mutations CfrN2K/N2I/S39G/I26M, and evolved variant CfrV3 in *E. coli* after halting expression by rifampicin treatment. Percentage of Cfr protein remaining over time was determined by immunoblotting against C-terminal FLAG tag and presented as the average of three biological replicates with standard error.

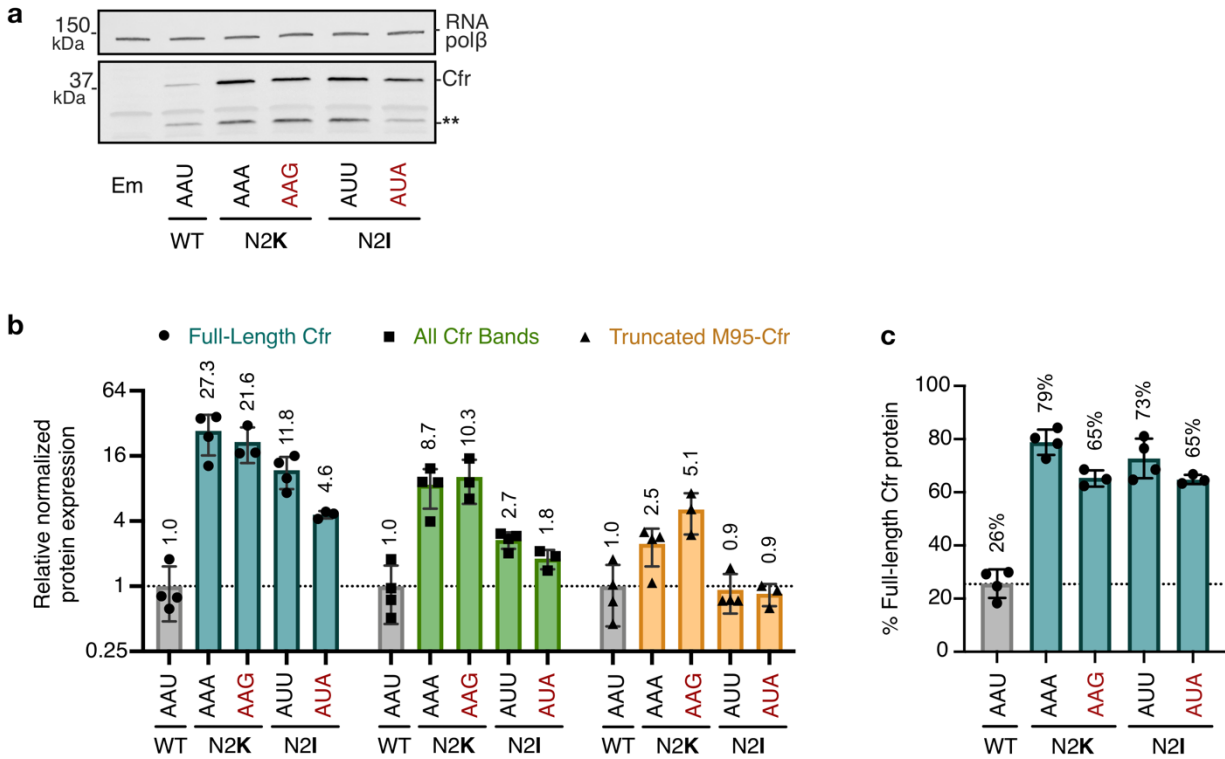


Figure 2.8 | Impact of 2nd codon identity on Cfr expression. (a) Cfr protein levels were assessed by immunoblotting against a C-terminal FLAG tag. Mutations away from the directed evolution mutation are in red lettering. Asterisks denote the truncated Cfr products that do not contribute to resistance. Em = empty vector control. (b) Relative protein expression of full-length Cfr (teal), all Cfr bands (green), and the truncation corresponding to translation initiation at Met95 (yellow) for second codon mutants compared to Cfr^{WT}. Signal was normalized to housekeeping protein RNA polymerase β -subunit. Data is presented as the average of three or four biological replicates with standard deviation on a \log_2 axis. (c) Percentage of total Cfr expression attributed to production of full-length Cfr protein, presented as the average of three or four biological replicates with standard deviation.

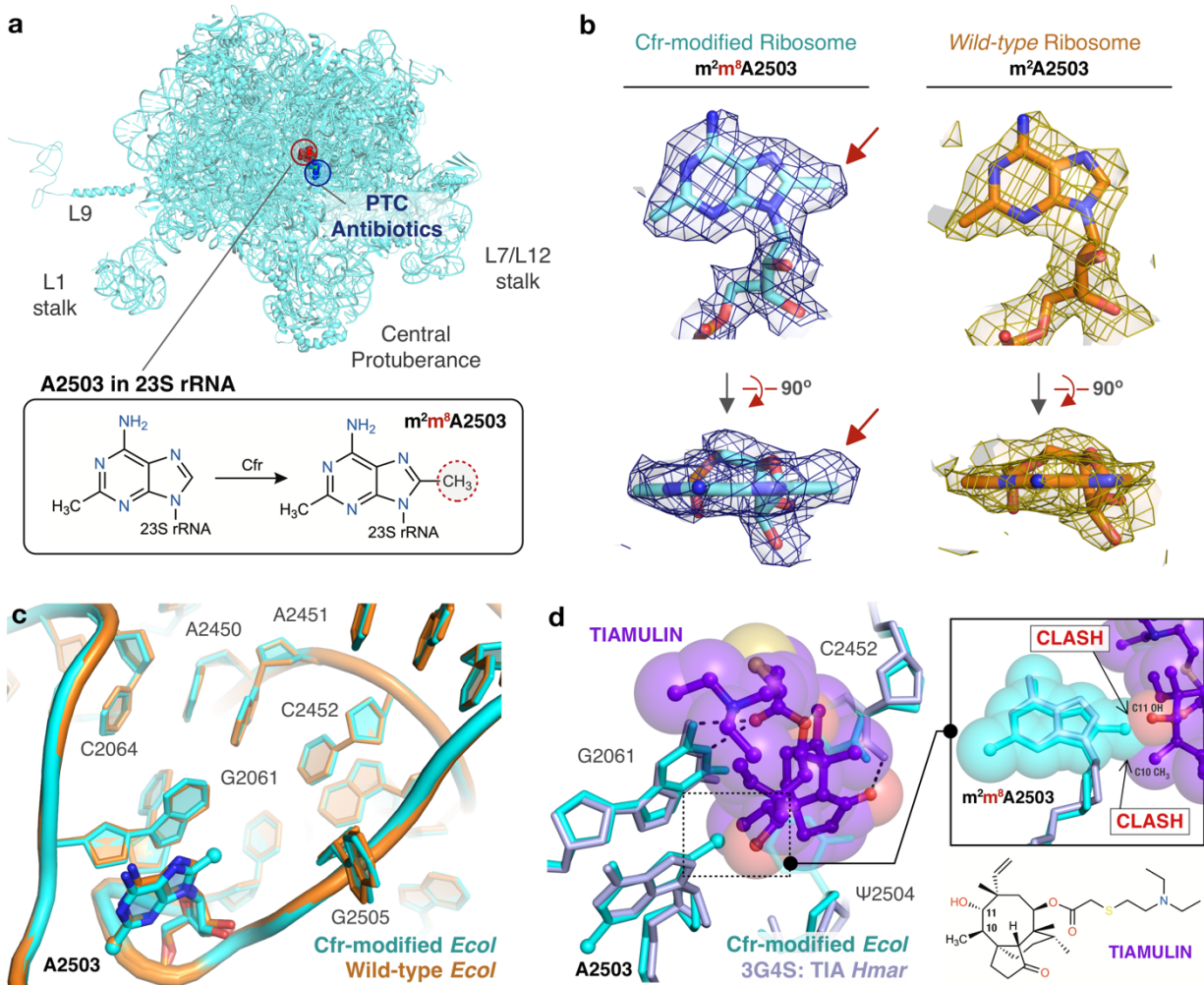


Figure 2.9 | Near-stoichiometric ribosome methylation by CfrV7 enables structural determination of Cfr-mediated resistance to antibiotics. (a) Cfr-modified 50S ribosomal subunit highlighting adenosine 2503 (A2503) within 23S rRNA and the binding site of PTC-targeting antibiotics. Cfr methylates A2503 at the C8 carbon to produce m^2m^8A2503 . (b) Cryo-EM density maps of adenosine 2503 in 23S rRNA contoured to 3σ . Cfr-modified (m^2m^8A2503) in cyan. Wild-type (m^2A2503) in orange; PDB 6PJ6. (c) Close up view of 23S rRNA nucleotides in the 50S ribosomal subunit. Cfr-modified *E. coli* ribosome in cyan. Wild-type *E. coli* ribosome in orange; PDB 6PJ6. (d) Structural overlay of Cfr-modified *E. coli* ribosome (cyan) and *H. marismortui* 50S ribosome in complex with pleuromutilin antibiotic tiamulin (purple, PDB 3G4S) highlighting steric clashes between m^8A2503 and the antibiotic.

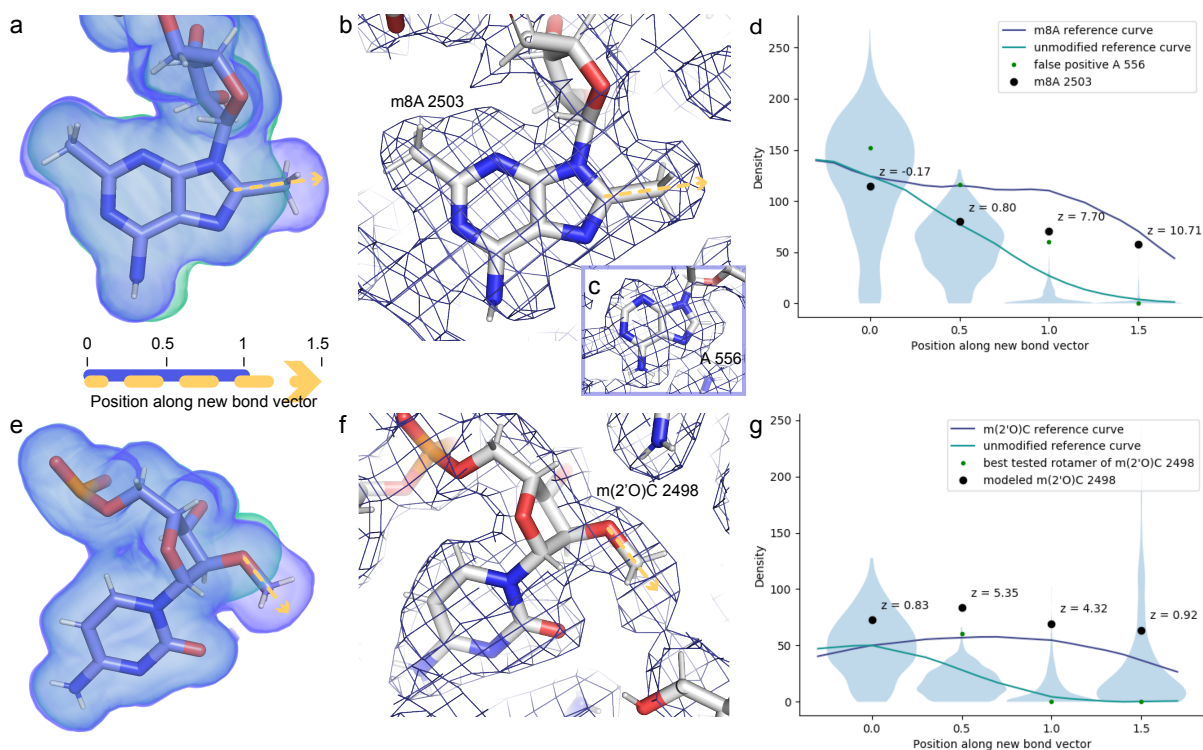


Figure 2.10 | Cross-validation of methylations on C8 of A2503 and 2'O of C2498 from the cryoEM density map. Ideal, noise-free densities were calculated for the post-transcriptionally modified (purple) and unmodified (green) nucleotides (**a**, **e**). We can distinguish which of these maps better matches the experimental map by examining the dropoff in density when moving from the reference atom (C8 or 2'O) toward and beyond the methyl group. To this end, the noise-free calculated densities were used to generate reference curves for these two modifications (**d**, **g**). These curves were scaled to match the mean density at the reference atom for all instances of adenosines (**d**) or cytosines (**g**) in the experimental structure, and for those same nucleotides, densities at four selected positions along the vector are also shown in violin plots (**d**, **g**). Based on these four densities as well as calculated difference density at the 1.0 position and the correlation coefficient between the calculated and experimental map for the entire nucleotide, the program qPTxM for detection of posttranscriptional modifications identified two adenosines where the map supported C8 methylation: A2503 and a false positive A556 (**b-d**). Investigation of the densities at these two sites confirmed that the shape of the density dropoff curve for A2503 more closely matched the methylated reference curve while that of A556 more closely matched the unmethylated reference curve, and that the latter site was identified as a strong candidate primarily due to the strong density at all atoms. qPTxM identified no cytosines where the map supported 2'O methylation (**g**). The densities along the methylation bond vector more closely match the unmodified than the methylated reference curve at C2498 (**f**) when the methyl group is placed at any of the rotameric positions (green dots), but along the modeled O-Me bond (black dots), the dropoff closely matches the shape of the methylated reference curve (**g**). Plots are annotated with Z-scores for the A2503 and C2498 densities relative to all adenosines and cytosines in the map.

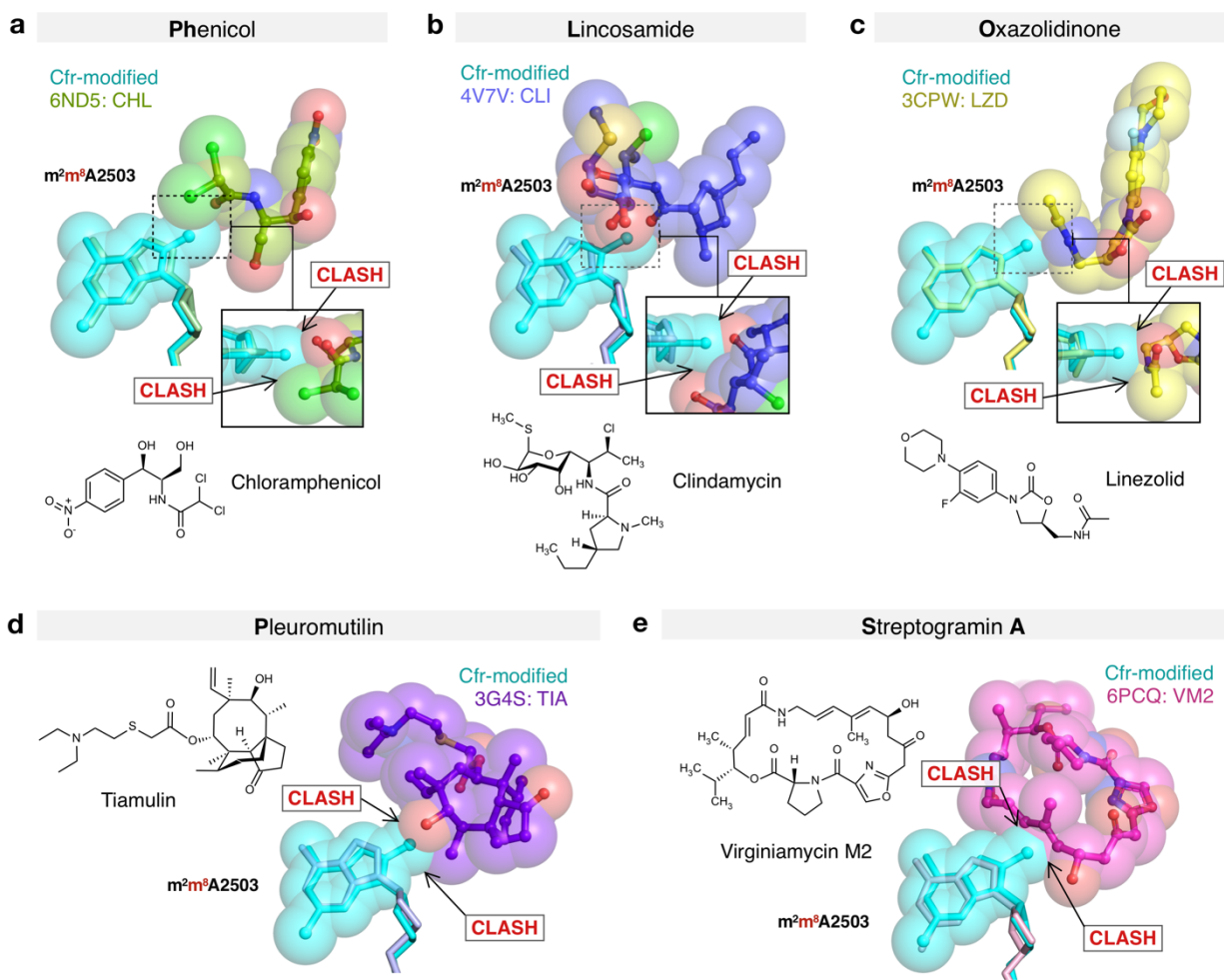


Figure 2.11 | Cfr-mediated resistance to PhLOPS_A antibiotics. Structural overlay of Cfr-modified *E. coli* 50S ribosome (cyan) and ribosomes in complex with (a) chloramphenicol (CHL); PDB 6ND5, (b) clindamycin (CLI); PDB 4V7V, (c) linezolid (LZD); PDB 3CPW, (d) tiamulin (TIA) PDB 3G4S, and (e) virginiamycin M2 (VM2); PDB 6PCQ. Inserts are close-up views of the steric clashes between m^8A2503 and corresponding PTC-targeting antibiotics.

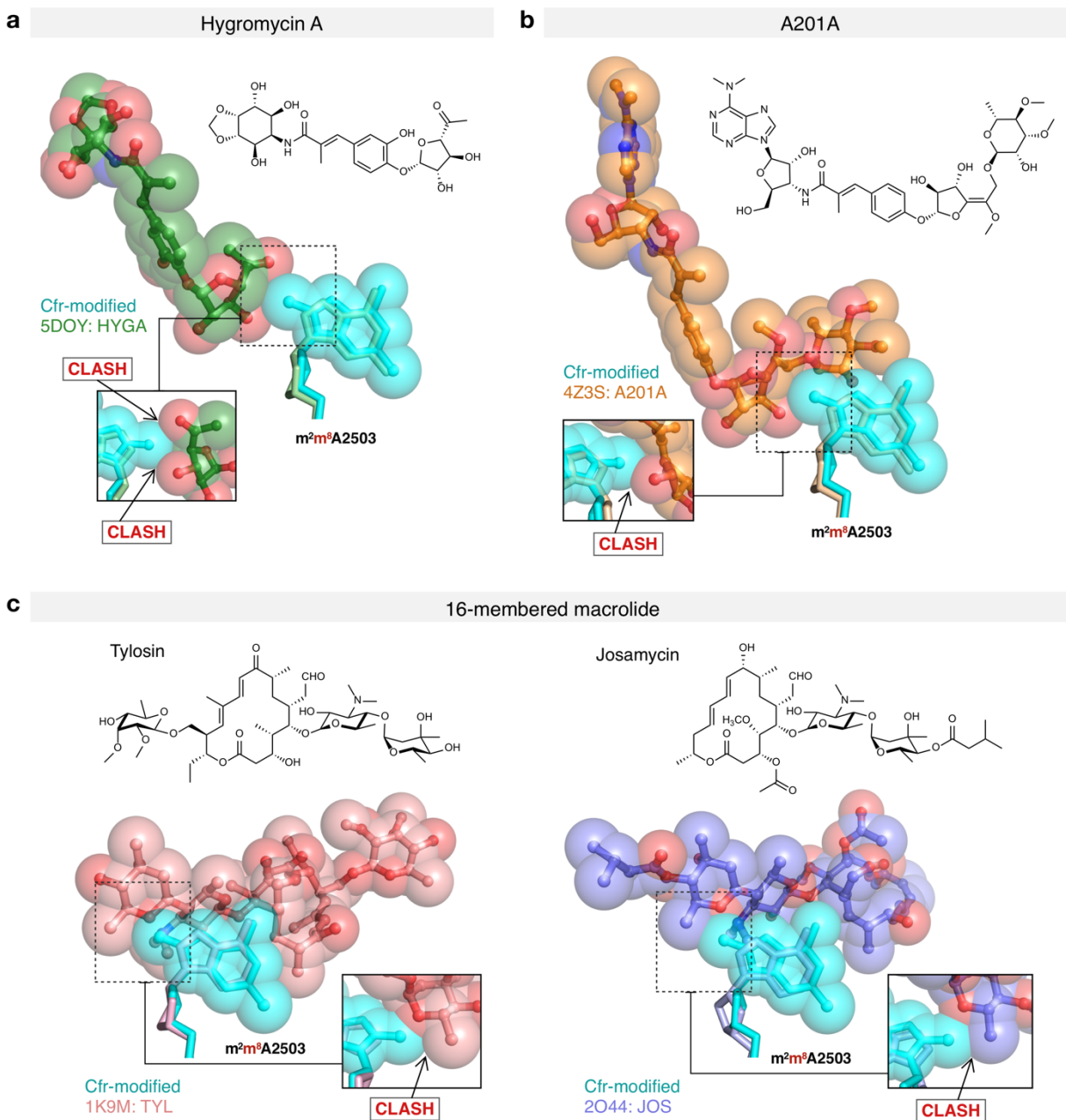


Figure 2.12 | Cfr-mediated resistance to hygromycin A, A201A, and 16-membered macrolide antibiotics. Structural overlay of Cfr-modified *E. coli* 50S ribosome (cyan) and ribosomes in complex with (a) hygromycin A (HYGA); PDB 5DOY, (b) nucleoside analog A201A; PDB 4Z3S, (c) 16-membered macrolides tylosin (TYL); PDB 1K9M and josamycin (JOS); PDB 2O44. Inserts are close-up views of the steric clashes between m^8A2503 and corresponding PTC-targeting antibiotics.

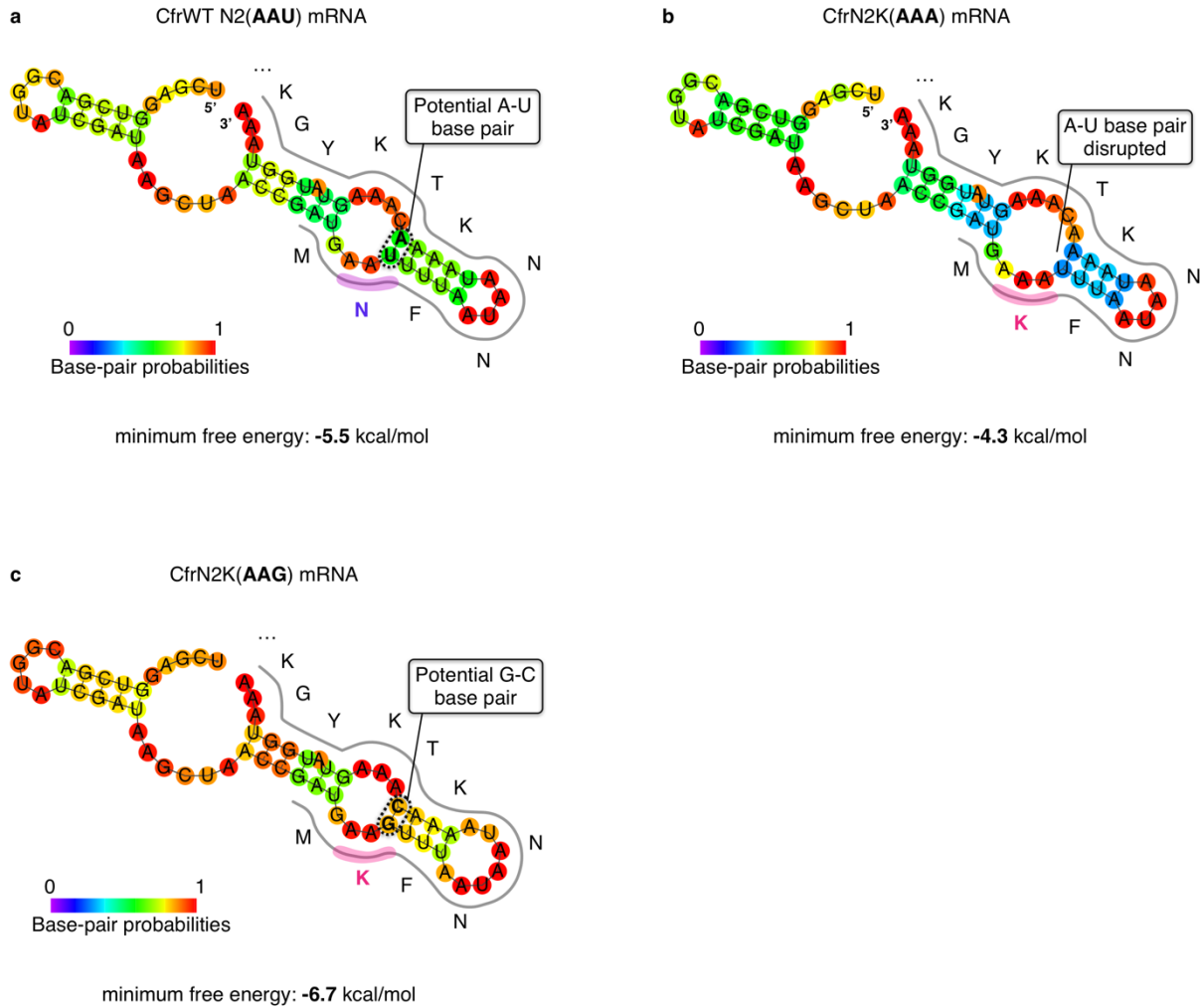


Figure 2.13 | RNA secondary structure predictions near the Cfr start codon. Minimum free energy secondary structure prediction by RNAfold v2.4.8¹⁰⁸ of the 30 mRNA nucleotides upstream and downstream of the Cfr AUG start codon for (a) CfrWT, (b) CfrN2K(AAA) and (c) CfrN2K(AAG). Bases are colored according to their base-pair probabilities.

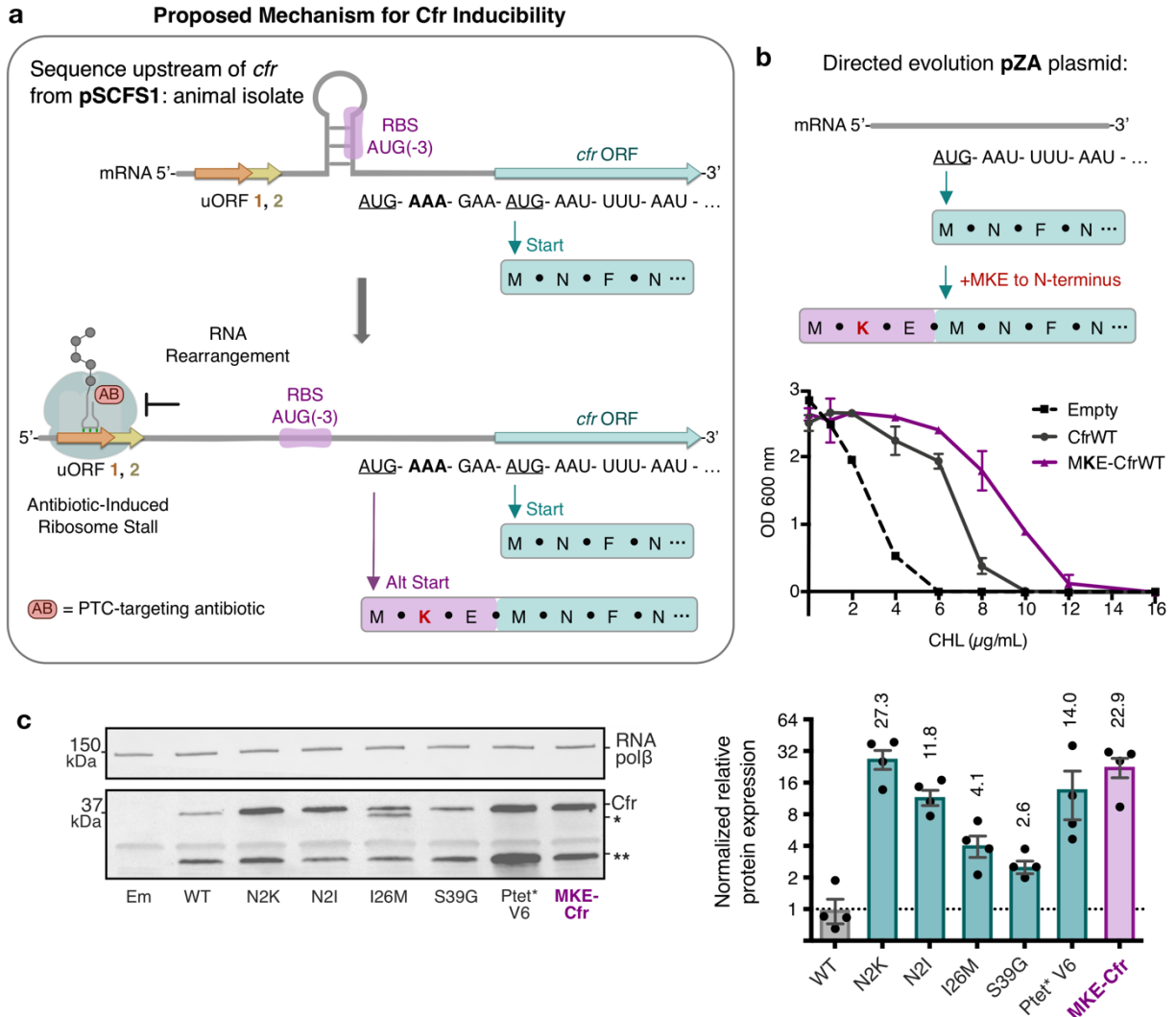


Figure 2.14 | Start codon selection as a proposed mechanism of Cfr inducibility. (a) Sequence upstream of *cfr* from pSCFS1 (Accession: AJ579365) resistance plasmid from an animal-derived *S. sciuri* isolate. The upstream region contains 2 overlapping upstream ORFs (uORFs) followed by an RNA structural element. Proposed antibiotic-induced ribosome stalling at uORF1/2 and RNA rearrangement could reveal the occluded RBS, allowing translation to initiate at AUG(-3), adding an MKE polypeptide to the N-terminus of Cfr. (b) Addition of an N-terminal MKE peptide to Cfr in the context of the pZA plasmid where expression is controlled by the non-native tetracycline-inducible promoter, P_{tet} . Growth inhibition of *E. coli* with pZA-encoded MKE-Cfr in the presence of CHL determined from two biological replicates with standard error. (c) Relative protein expression of full-length MKE-Cfr compared to full-length CfrWT detected by immunoblotting against a C-terminal FLAG tag and quantification of top Cfr bands. Signal was normalized to housekeeping protein RNA polymerase β -subunit. Data is presented as the average of four biological replicates with standard deviation on a \log_2 axis. Em = empty vector control.

Gene	% Id	Accession No/ IMG Database ID	2	28	38			
Cfr	100	AJ879565	-MNFNNKTKY	GKIQEFLRSN	NEPDYR IKQI	TNAIFKQRIS	RFEDMKVLPK	LLREDLINNF
Cfr (B)	74	KM359438	---M Q QKNKY	IRIQEFLKQN	KFPN YR IKQI	TNAIFPGRIN	NFNEITVLPK	SLRDMLIEEF
Cfr (C)	55	CCL89685	-----M S KY	KKMKQLIADM	RLPEYR Y KQL	LDAVFLQGIM	RFEDMKLLPK	TLREKLVEQF
Cfr (D)	64	MG707078	-ML Q KQLTKY	QQIEKVLKEC	QQPNYR IK QI	LHCIFKEKKT	DFNEMSVLPK	NLRDTLTTEI
Cfr (E)	51	WP_105119688.1	---M I YSKY	EVMKRCISGM	NFPDYR Y EQL	IKMIFAQHIP	DFHSMYMLPE	RLRSNLAETF
	74	2511698410	---M Q QKNKY	IRIQEFLKQN	KFPDFR IN QI	KNAVFKGRIN	HFNEITVLPK	SLRKLMLNEF
	56	643787315	---M K LTSKY	ETIRRILSEC	KQPEYR Y AQI	MDAIFKQNI G	EYERM T ILPK	FLRDELNRIL
	56	646363554	---M K YLSKY	EKIRKILSAL	NQPNYR Y SQI	TEAIFK KN IG	NFEAMNNL P K	PVRNELIKEL
	61	2815943689	M K VVN H ATKY	ERLKHFLNAL	NEPTYR Y KQI	TEAIFK H RIG	AFNKMT T L P K	ALRESLINEF
	57	2609355091	--M K Q T KTKY	GKIKQILSNL	KLPDYR Y EQL	TKAIFHQRID	NFEDMHIL P K	ALRIALVNEF
	56	642847821	--M K Q T KTKY	GKIKQIVSNL	KLPDYR Y EQL	TKAIFHQRID	NFEDMHIL P K	ALRMALVNEF
	55	2517499511	--M K Q T KTKY	EKIKQIVSNL	KLPDYR Y EQV	TKAIFHQRID	NFDDM R IL P K	ALRIALVNEF
	55	2558672851	--M K Q T KIKY	GKMKQVSNL	KLPDYR Y EQL	AKAIFHQRID	DFDDMHIL P K	ALRIALVNEF
	54	641293316	---M N YSKY	ETMKQLIADM	KLPDYR Y EQI	IKAIF S QHT S	TFEKM S T L PL	ELK K SLINT F

Figure 2.15 | Protein sequence alignment of Cfr and Cfr homologues. CfrWT used for the starting point for directed evolution is displayed as the top sequence (Cfr) in blue. Cfr(B), Cfr(C), Cfr(D), and Cfr(E) are Cfr homologues which have been functionally characterized, reviewed⁸⁸. Remaining sequences are Cfr homologues that clade with Cfr or Cfr-like genes as described previously (Stojković et al., 2019). Percent shared amino acid identity (% Id) with Cfr is noted. Directed evolution mutations N2K, I26M, and S39G are highlighted with red lettering. Alignment was performed using MUSCLE¹⁰⁹ and the first ~60 residues are displayed. Cfr homologous sequences were derived from the following organisms: *Staphylococcus aureus* (AJ879565), *Clostridioides difficile* (KM359438), *Clostridioides difficile* T10 (CCL89685), *Enterococcus faecium* (MG707078), Firmicutes (WP_105119688.1), *Bacillus amyloliquefaciens* (2511698410), *Brevibacillus brevis* (643787315), *Geobacillus* sp. Y412MC10 (646363554), *Bacillus clausii* (2815943689), *Clostridium saccharoperbutylacetonicum* (2609355091), *Clostridium sporogenes* (642847821), *Clostridium acidurici* (2517499511), *Clostridium manganotii* (2558672851), *Clostridium phytofermentans* (641293316).

Table 2.1 | Cfr sequence variants from the first enrichment round. Open reading frame mutations and alterations to sequences 5' (promoter) and 3' (insertion in 3' untranslated region) of the *cfr* gene are designated. Green lettering designates to the original Asn codon in CfrWT, while green with * designates an Asn synonymous codon. N2K(AAA) codon is in red, while N2I(AUU) codon is in blue.

Tiamulin µg/mL	Colony #	Mutations	2 nd Codon
400	2 (CfrV6)	Promoter, I26M, E351Stop, 3'UTR-INS	AAU
	3	N2K , S39G, I326V, Q346H, E351Stop	AAA
	4	N2K , S39G, N57D, S348C, E351Stop, 3'UTR-INS	AAA
	5	N2K , S18R, E266D, E351Stop	AAA
	6 (CfrV2)	N2K , S39G, E351Stop	AAA
500	1	N2K , I26M, S273R, E351Stop	AAA
	2	N2K , S39G, N347K, S348Stop	AAA
	3 (CfrV3)	N2K , I26M, S39G, E351Stop, 3'UTR-INS	AAA
	5	N2K , S39G, K198N, Q346Stop	AAA
	6	N2K , S39G, E351Stop, 3'UTR-INS	AAA
	7	<i>N2I</i> , S39G, Q202H, M301K, E351Stop, 3'UTR-INS	AUU
600	1 (CfrV1)	N2K , I26M, E351Stop, 3'UTR-INS	AAA
	2	<i>N2I</i> , I26M, N73H, E351Stop	AUU
	4	N2K , N20S, K35R, S39G, L68F, N238D, L265H, E351Stop	AAA
	5	<i>N2I</i> , S39G, Q349Stop, 3'UTR-INS	AUU
700	1 (CfrV7)	Promoter, S39G, E351Stop, 3'UTR-INS	AAU
	2	N5K, S39G, I233L, E351Stop	AAU
	4	<i>N2I</i> , I26M, S39G, G308V, E351Stop	AUU
	5	S39G, L68F, G115R, K198R, E351Stop, 3'UTR-INS	AAC*
	6	S39G, L289M, E351Stop, 3'UTR-INS	AAC*
	7	<i>N2I</i> , S39G, E351Stop, 3'UTR-INS	AUU
	8	N2K , I26M, N238D, E351Stop	AAA
800	1	N2K , S39G, Q346R, Q349Stop, 3'UTR-INS	AAA
	2	<i>N2I</i> , S39G, I233L, P259H, Q349Stop, 3'UTR-INS	AUU
	4	N5I, K35R, S39G, E351Stop, 3'UTR-INS	AAC*
	5	Promoter, L68F, S348N, E351Stop, 3'UTR-INS	AAU
	6	Promoter, I26M, K45Q, L68F, E351Stop, 3'UTR-INS	AAU

Table 2.2 | Cfr sequence variants from the second enrichment round. Open reading frame mutations and alterations to sequences 5' (promoter) and 3' (insertion in 3' untranslated region) of the cfr gene are designated. Green lettering designates to the original Asn codon in CfrWT, while green with * designates an Asn synonymous codon. N2K(AAA) codon is in red, while N2I(AUU) codon is in blue.

Tiamulin µg/mL	Colony #	Mutations	2 nd Codon
1000	1	Promoter, <i>N2I</i> , D23E, I26M, A305T, Q349Stop, 3'UTR-INS	<i>AUU</i>
	2	N2K , S39G, Q346R, E351Stop, 3'UTR-INS	AAA
	3	N2K , I26M, T62A, E351Stop	AAA
	4	N5K, S39G, A305T, E351Stop	<i>AAU</i>
	6	N2K , S39G, N65S, Q349Stop, 3'UTR-INS	AAA
	7 (CfrV5)	<i>N2I</i> , S39G, E351Stop, 3'UTR-INS	<i>AUU</i>
	8	N2K , I26M, Q349Stop, 3'UTR-INS	AAA
1250	2	S39G, L68F, G115R, K198R, E351Stop, 3'UTR-INS	<i>AAC</i> *
	4	Promoter, Y127F, D234G, E351Stop, 3'UTR-INS	<i>AAC</i> *
	5	Promoter, I26M, S39G, Q72K, S85T, E351Stop, 3'UTR-INS	<i>AAU</i>
	6	N2K , I26M, N65S, Q349Stop, 3'UTR-INS	AAA
	7 (CfrV4)	N2K , I26M, L68F, E351Stop, 3'UTR-INS	AAA
	8	Promoter, N5K, S39G, S273N, S277R, K315E, E351Stop	<i>AAU</i>
1500	1	Promoter, N2K , R17S, N73H, E351Stop	AAA
	2	N2K , S39G, S196G, E270K, G308R, K315R, E351Stop, 3'UTR-INS	AAA
	4	Promoter, N2K , S39G, Q346H, S348I, 3'UTR-INS	AAA
	5	Promoter, I26M, Q36L, N347K, S348Stop, 3'UTR-INS	<i>AAU</i>
	6	Promoter, <i>N2I</i> , D23E, I26M, A305T, Q349Stop, 3'UTR-INS	<i>AUU</i>
	7	N2K , S39G, E351Stop	AAA
	8	Promoter, S39G, E351Stop, 3'UTR-INS	<i>AAU</i>

Table 2.3 | Promoter architecture of Cfr variants from final enrichment rounds with promoter alterations. Abbreviations: Ptet = promoter; Ins = insertion sequence of various length; pPtet = partial promoter.

Enrichment Round	Tiamulin $\mu\text{g/mL}$	Colony #	Promoter Architecture
-	-	CfrWT	Ptet – cfr
1	400	2 (CfrV6)	Ptet – Ins – Ptet – cfr
	700	1 (CfrV7)	Ptet – Ins – pPtet – cfr
	800	5	Ptet – Ins – pPtet – cfr
	800	6	Ptet – Ins – pPtet – cfr
2	1000	1	Ptet – Ins – pPtet – cfr
	1250	4	Ptet – Ins – pPtet – cfr
	1250	5	Ptet – Ins – pPtet – cfr
	1250	8	Ptet – Ins – pPtet – cfr
	1500	1	Ptet – Ins – pPtet – cfr
	1500	4	Ptet – Ins – pPtet – cfr
	1500	5	Ptet – Ins – pPtet – Ins – pPtet – cfr
	1500	6	Ptet – Ins – pPtet – cfr
	1500	8	Ptet – Ins – pPtet – cfr

Table 2.4 | Cryo-EM data collection, refinement, and validation statistics

Data collection and processing	
Electron microscope	Krios
Magnification	29 000
Number of micrographs	2055
Number of particles picked from good micrographs	162 713
Number of particles used in final reconstruction	141 549
Pixel size (Å)	0.822
Defocus range (µm)	-0.2 to -1.5
Voltage (kV)	300
Electron dose (e-/Å ²)	80
Map refinement	
Model resolution (Å)	2.2
FSC threshold	0.143
Model resolution range (Å)	2.2–20
Map sharpening B-factor (Å ²)	-55.86
Refinement and model statistics	
Clashscore, all atoms	2.23
	<u>Protein geometry</u>
MolProbity score	1.29
Rotamer outliers (%)	0.92
Cβ deviations >0.25 Å (%)	0.32
Ramachandran (%)	
- Favored	95.79
- Allowed	4.01
- Outliers	0.2
Deviations from ideal geometry	
- Bonds (%)	0.03
- Angles (%)	0.08
	<u>Nucleic acid geometry</u>
Probably wrong sugar puckers (%)	0.84
Bad backbone conformations (%)	12.86
Bad bonds (%)	0.07
Bad angles (%)	0.08

Table 2.5 | Primer sequences used in this study

Primer Name	Application	Sequence
cfr	RT-qPCR	Fwd: 5'-AGCAGAGCAAAATTCAGAGCAAGT-3' Rev: 5'-TCCAATGTGCGCCTGTAGCACAA-3' Length of amplicon: 169 bp
luc Accession no: X65316.2	RT-qPCR	Fwd: 5'-AGATCGTGGATTACGTGCGCC-3' Rev: 5'-TGGACTTTCCGCCCTTCTTG-3' Length of amplicon: 156 bp
recA Accession no: CP037857.1	RT-qPCR	Fwd: 5'-ATCGCCTGGCTCATCATACG-3' Rev: 5'-GCACTGGAAATCTGTGACGC-3' Length of amplicon: 152 bp

References

1. Tenson, T. & Mankin, A. Antibiotics and the ribosome. *Mol. Microbiol.* **59**, 1664–1677 (2006).
2. Wilson, D. N. The A–Z of bacterial translation inhibitors. *Critical Reviews in Biochemistry and Molecular Biology* vol. 44 393–433 (2009).
3. Arenz, S. & Wilson, D. N. Blast from the Past: Reassessing Forgotten Translation Inhibitors, Antibiotic Selectivity, and Resistance Mechanisms to Aid Drug Development. *Mol. Cell* **61**, 3–14 (2016).
4. Vester, B. & Long, K. S. *Antibiotic Resistance in Bacteria Caused by Modified Nucleosides in 23S Ribosomal RNA*. (Landes Bioscience, 2013).
5. Wilson, D. N. Ribosome-targeting antibiotics and mechanisms of bacterial resistance. *Nat. Rev. Microbiol.* **12**, 35–48 (2014).
6. Schwarz, S., Werckenthin, C. & Kehrenberg, C. Identification of a Plasmid-Borne Chloramphenicol-Florfenicol Resistance Gene in *Staphylococcus sciuri*. *Antimicrob. Agents Chemother.* **44**, 2530–2533 (2000).
7. Kehrenberg, C., Schwarz, S., Jacobsen, L., Hansen, L. H. & Vester, B. A new mechanism for chloramphenicol, florfenicol and clindamycin resistance: methylation of 23S ribosomal RNA at A2503. *Mol. Microbiol.* **57**, 1064–1073 (2005).
8. Giessing, A. M. B. *et al.* Identification of 8-methyladenosine as the modification catalyzed by the radical SAM methyltransferase Cfr that confers antibiotic resistance in bacteria. *RNA* **15**, 327–336 (2009).
9. Kaminska, K. H. *et al.* Insights into the structure, function and evolution of the radical-SAM 23S rRNA methyltransferase Cfr that confers antibiotic resistance in bacteria. *Nucleic*

- Acids Res.* **38**, 1652–1663 (2010).
10. Yan, F. *et al.* RlmN and Cfr are radical SAM enzymes involved in methylation of ribosomal RNA. *J. Am. Chem. Soc.* **132**, 3953–3964 (2010).
 11. Yan, F. & Fujimori, D. G. RNA methylation by radical SAM enzymes RlmN and Cfr proceeds via methylene transfer and hydride shift. *Proc. Natl. Acad. Sci. U. S. A.* **108**, 3930–3934 (2011).
 12. Grove, T. L. *et al.* A Radically Different Mechanism for S-Adenosylmethionine-Dependent Methyltransferases. *Science* vol. 332 604–607 (2011).
 13. Long, K. S., Poehlsgaard, J., Kehrenberg, C., Schwarz, S. & Vester, B. The Cfr rRNA methyltransferase confers resistance to Phenicol, Lincosamides, Oxazolidinones, Pleuromutilins, and Streptogramin A antibiotics. *Antimicrob. Agents Chemother.* **50**, 2500–2505 (2006).
 14. Smith, L. K. & Mankin, A. S. Transcriptional and translational control of the mlr operon, which confers resistance to seven classes of protein synthesis inhibitors. *Antimicrob. Agents Chemother.* **52**, 1703–1712 (2008).
 15. Polikanov, Y. S. *et al.* Distinct tRNA Accommodation Intermediates Observed on the Ribosome with the Antibiotics Hygromycin A and A201A. *Mol. Cell* **58**, 832–844 (2015).
 16. Toh, S.-M. *et al.* Acquisition of a natural resistance gene renders a clinical strain of methicillin-resistant *Staphylococcus aureus* resistant to the synthetic antibiotic linezolid. *Mol. Microbiol.* **64**, 1506–1514 (2007).
 17. Arias, C. A. *et al.* Clinical and microbiological aspects of linezolid resistance mediated by the cfr gene encoding a 23S rRNA methyltransferase. *J. Clin. Microbiol.* **46**, 892–896 (2008).

18. Shen, J., Wang, Y. & Schwarz, S. Presence and dissemination of the multiresistance gene *cfr* in Gram-positive and Gram-negative bacteria. *J. Antimicrob. Chemother.* **68**, 1697–1706 (2013).
19. Vester, B. The *cfr* and *cfr*-like multiple resistance genes. *Res. Microbiol.* **169**, 61–66 (2018).
20. Morales, G. *et al.* Resistance to linezolid is mediated by the *cfr* gene in the first report of an outbreak of linezolid-resistant *Staphylococcus aureus*. *Clin. Infect. Dis.* **50**, 821–825 (2010).
21. Locke, J. B. *et al.* Elevated linezolid resistance in clinical *cfr*-positive *Staphylococcus aureus* isolates is associated with co-occurring mutations in ribosomal protein L3. *Antimicrob. Agents Chemother.* **54**, 5352–5355 (2010).
22. Bonilla, H. *et al.* Multicity outbreak of linezolid-resistant *Staphylococcus epidermidis* associated with clonal spread of a *cfr*-containing strain. *Clin. Infect. Dis.* **51**, 796–800 (2010).
23. Cai, J. C., Hu, Y. Y., Zhou, H. W., Chen, G.-X. & Zhang, R. Dissemination of the same *cfr*-carrying plasmid among methicillin-resistant *Staphylococcus aureus* and coagulase-negative staphylococcal isolates in China. *Antimicrob. Agents Chemother.* **59**, 3669–3671 (2015).
24. Layer, F. *et al.* Dissemination of linezolid-dependent, linezolid-resistant *Staphylococcus epidermidis* clinical isolates belonging to CC5 in German hospitals. *J. Antimicrob. Chemother.* **73**, 1181–1184 (2018).
25. Lazaris, A. *et al.* Novel multiresistance *cfr* plasmids in linezolid-resistant methicillin-resistant *Staphylococcus epidermidis* and vancomycin-resistant *Enterococcus faecium* (VRE) from a hospital outbreak: co-location of *cfr* and *optrA* in VRE. *J. Antimicrob. Chemother.* **72**, 3252–3257 (2017).
26. Dortet, L. *et al.* Long-lasting successful dissemination of resistance to oxazolidinones in

- MDR *Staphylococcus epidermidis* clinical isolates in a tertiary care hospital in France. *J. Antimicrob. Chemother.* **73**, 41–51 (2018).
27. Weßels, C. *et al.* Emergence and control of linezolid-resistant *Staphylococcus epidermidis* in an ICU of a German hospital. *J. Antimicrob. Chemother.* **73**, 1185–1193 (2018).
 28. LaMarre, J. M., Locke, J. B., Shaw, K. J. & Mankin, A. S. Low fitness cost of the multidrug resistance gene *cf*. *Antimicrob. Agents Chemother.* **55**, 3714–3719 (2011).
 29. Schwarz, S. *et al.* Lincosamides, Streptogramins, Phenicol, and Pleuromutilins: Mode of Action and Mechanisms of Resistance. *Cold Spring Harb. Perspect. Med.* **6**, (2016).
 30. Toh, S.-M., Xiong, L., Bae, T. & Mankin, A. S. The methyltransferase YfgB/RlmN is responsible for modification of adenosine 2503 in 23S rRNA. *RNA* **14**, 98–106 (2008).
 31. Schlünzen, F. *et al.* Structural basis for the interaction of antibiotics with the peptidyl transferase centre in eubacteria. *Nature* **413**, 814–821 (2001).
 32. Tu, D., Blaha, G., Moore, P. B. & Steitz, T. A. Structures of MLSBK antibiotics bound to mutated large ribosomal subunits provide a structural explanation for resistance. *Cell* **121**, 257–270 (2005).
 33. Stojković, V. *et al.* Assessment of the nucleotide modifications in the high-resolution cryo-electron microscopy structure of the *Escherichia coli* 50S subunit. *Nucleic Acids Res.* **48**, 2723–2732 (2020).
 34. Barlow, M. & Hall, B. G. Experimental prediction of the natural evolution of antibiotic resistance. *Genetics* **163**, 1237–1241 (2003).
 35. Wellner, A., Raitses Gurevich, M. & Tawfik, D. S. Mechanisms of protein sequence divergence and incompatibility. *PLoS Genet.* **9**, e1003665 (2013).
 36. Stojković, V., Noda-Garcia, L., Tawfik, D. S. & Fujimori, D. G. Antibiotic resistance

- evolved via inactivation of a ribosomal RNA methylating enzyme. *Nucleic Acids Res.* **44**, 8897–8907 (2016).
37. Andersen, T. E., Porse, B. T. & Kirpekar, F. A novel partial modification at C2501 in *Escherichia coli* 23S ribosomal RNA. *RNA* **10**, 907–913 (2004).
 38. Stojković, V. & Fujimori, D. G. Radical SAM-Mediated Methylation of Ribosomal RNA. *Methods Enzymol.* **560**, 355–376 (2015).
 39. Bauerle, M. R., Grove, T. L. & Booker, S. J. Investigation of Solvent Hydron Exchange in the Reaction Catalyzed by the Antibiotic Resistance Protein Cfr. *Biochemistry* **57**, 4431–4439 (2018).
 40. Gottesman, S. Proteolysis in bacterial regulatory circuits. *Annu. Rev. Cell Dev. Biol.* **19**, 565–587 (2003).
 41. Bhattacharyya, S. *et al.* Accessibility of the Shine-Dalgarno Sequence Dictates N-Terminal Codon Bias in *E. coli*. *Mol. Cell* **70**, 894–905.e5 (2018).
 42. Bentele, K., Saffert, P., Rauscher, R., Ignatova, Z. & Blüthgen, N. Efficient translation initiation dictates codon usage at gene start. *Mol. Syst. Biol.* **9**, 675 (2013).
 43. Tuller, T. *et al.* An evolutionarily conserved mechanism for controlling the efficiency of protein translation. *Cell* **141**, 344–354 (2010).
 44. Verma, M. *et al.* A short translational ramp determines the efficiency of protein synthesis. *Nat. Commun.* **10**, 5774 (2019).
 45. Goodman, D. B., Church, G. M. & Kosuri, S. Causes and Effects of N-Terminal Codon Bias in Bacterial Genes. *Science* vol. 342 475–479 (2013).
 46. Boël, G. *et al.* Codon influence on protein expression in *E. coli* correlates with mRNA levels. *Nature* **529**, 358–363 (2016).

47. Looman, A. C. *et al.* Influence of the codon following the AUG initiation codon on the expression of a modified lacZ gene in Escherichia coli. *EMBO J.* **6**, 2489–2492 (1987).
48. Stenström, C. M., Jin, H., Major, L. L., Tate, W. P. & Isaksson, L. A. Codon bias at the 3'-side of the initiation codon is correlated with translation initiation efficiency in Escherichia coli. *Gene* **263**, 273–284 (2001).
49. Stenström, C. M., Holmgren, E. & Isaksson, L. A. Cooperative effects by the initiation codon and its flanking regions on translation initiation. *Gene* **273**, 259–265 (2001).
50. Stenström, C. M. & Isaksson, L. A. Influences on translation initiation and early elongation by the messenger RNA region flanking the initiation codon at the 3' side. *Gene* **288**, 1–8 (2002).
51. Sato, T. *et al.* Codon and base biases after the initiation codon of the open reading frames in the Escherichia coli genome and their influence on the translation efficiency. *J. Biochem.* **129**, 851–860 (2001).
52. Li, G.-W., Burkhardt, D., Gross, C. & Weissman, J. S. Quantifying Absolute Protein Synthesis Rates Reveals Principles Underlying Allocation of Cellular Resources. *Cell* vol. 157 624–635 (2014).
53. Dong, H., Nilsson, L. & Kurland, C. G. Co-variation of tRNA Abundance and Codon Usage in Escherichia coli at Different Growth Rates. *Journal of Molecular Biology* vol. 260 649–663 (1996).
54. Del Tito, B. J., Jr *et al.* Effects of a minor isoleucyl tRNA on heterologous protein translation in Escherichia coli. *J. Bacteriol.* **177**, 7086–7091 (1995).
55. Nakamura, Y., Gojobori, T. & Ikemura, T. Codon usage tabulated from international DNA sequence databases: status for the year 2000. *Nucleic Acids Res.* **28**, 292 (2000).

56. Purta, E., O'Connor, M., Bujnicki, J. M. & Douthwaite, S. YgdE is the 2'-O-ribose methyltransferase RlmM specific for nucleotide C2498 in bacterial 23S rRNA. *Mol. Microbiol.* **72**, 1147–1158 (2009).
57. Goethe, O., Heuer, A., Ma, X., Wang, Z. & Herzon, S. B. Antibacterial properties and clinical potential of pleuromutilins. *Nat. Prod. Rep.* **36**, 220–247 (2019).
58. Murphy, S. K., Zeng, M. & Herzon, S. B. A modular and enantioselective synthesis of the pleuromutilin antibiotics. *Science* **356**, 956–959 (2017).
59. Farney, E. P., Feng, S. S., Schäfers, F. & Reisman, S. E. Total Synthesis of (+)-Pleuromutilin. *J. Am. Chem. Soc.* **140**, 1267–1270 (2018).
60. Besier, S., Ludwig, A., Zander, J., Brade, V. & Wichelhaus, T. A. Linezolid resistance in *Staphylococcus aureus*: gene dosage effect, stability, fitness costs, and cross-resistances. *Antimicrob. Agents Chemother.* **52**, 1570–1572 (2008).
61. Ebihara, N., Hitomi, S., Goto, M., Koganemaru, H. & Sekiguchi, Y. Recovery of linezolid-resistant, methicillin-susceptible *Staphylococcus aureus* in a case of implanted pacemaker-associated infection. *JMM Case Reports* **1**, e001297 (2014).
62. Lobritz, M., Hutton-Thomas, R., Marshall, S. & Rice, L. B. Recombination proficiency influences frequency and locus of mutational resistance to linezolid in *Enterococcus faecalis*. *Antimicrob. Agents Chemother.* **47**, 3318–3320 (2003).
63. McCusker, K. P. *et al.* Covalent intermediate in the catalytic mechanism of the radical S-adenosyl-L-methionine methyl synthase RlmN trapped by mutagenesis. *J. Am. Chem. Soc.* **134**, 18074–18081 (2012).
64. Grove, T. L., Benner, J. S., Radle, M. I. & Ahlum, J. H. A radically different mechanism for S-adenosylmethionine-dependent methyltransferases. (2011).

65. Saito, K., Green, R. & Buskirk, A. R. Translational initiation in *E. coli* occurs at the correct sites genome-wide in the absence of mRNA-rRNA base-pairing. *Elife* **9**, (2020).
66. Boal, A. K. *et al.* Structural basis for methyl transfer by a radical SAM enzyme. *Science* **332**, 1089–1092 (2011).
67. Schwalm, E. L., Grove, T. L., Booker, S. J. & Boal, A. K. Crystallographic capture of a radical S-adenosylmethionine enzyme in the act of modifying tRNA. *Science* **352**, 309–312 (2016).
68. LaMarre, J. *et al.* The genetic environment of the *cfr* gene and the presence of other mechanisms account for the very high linezolid resistance of *Staphylococcus epidermidis* isolate 426-3147L. *Antimicrob. Agents Chemother.* **57**, 1173–1179 (2013).
69. Dougan, D. A., Micevski, D. & Truscott, K. N. The N-end rule pathway: From recognition by N-recognins, to destruction by AAA proteases. *Biochimica et Biophysica Acta (BBA) - Molecular Cell Research* vol. 1823 83–91 (2012).
70. Tobias, J. W., Shrader, T. E., Rocap, G. & Varshavsky, A. The N-end rule in bacteria. *Science* **254**, 1374–1377 (1991).
71. Koubek, J., Schmitt, J., Galmozzi, C. V. & Kramer, G. Mechanisms of Cotranslational Protein Maturation in Bacteria. *Front Mol Biosci* **8**, 689755 (2021).
72. Ragusa, S., Mouchet, P., Lazennec, C., Dive, V. & Meinnel, T. Substrate recognition and selectivity of peptide deformylase. Similarities and differences with metzincins and thermolysin. *J. Mol. Biol.* **289**, 1445–1457 (1999).
73. Hirel, P. H., Schmitter, M. J., Dessen, P., Fayat, G. & Blanquet, S. Extent of N-terminal methionine excision from *Escherichia coli* proteins is governed by the side-chain length of the penultimate amino acid. *Proc. Natl. Acad. Sci. U. S. A.* **86**, 8247–8251 (1989).

74. Frottin, F. *et al.* The Proteomics of N-terminal Methionine Cleavage* *S. Mol. Cell. Proteomics* **5**, 2336–2349 (2006).
75. Xiao, Q., Zhang, F., Nacev, B. A., Liu, J. O. & Pei, D. Protein N-terminal processing: substrate specificity of Escherichia coli and human methionine aminopeptidases. *Biochemistry* **49**, 5588–5599 (2010).
76. Izert, M. A., Klimecka, M. M. & Górna, M. W. Applications of Bacterial Degrons and Degradors — Toward Targeted Protein Degradation in Bacteria. *Frontiers in Molecular Biosciences* vol. 8 (2021).
77. Ottofuelling, R. D., Ninnis, R. L., Truscott, K. N. & Dougan, D. A. Novel modification by L/F-tRNA-protein transferase (LFTR) generates a Leu/N-degron ligand in Escherichia coli. *bioRxiv* (2021).
78. Kudla, G., Murray, A. W., Tollervey, D. & Plotkin, J. B. Coding-sequence determinants of gene expression in Escherichia coli. *Science* **324**, 255–258 (2009).
79. Cifuentes-Goches, J. C., Hernández-Ancheyta, L., Guarneros, G., Oviedo, N. & Hernández-Sánchez, J. Domains two and three of Escherichia coli ribosomal S1 protein confers 30S subunits a high affinity for downstream A/U-rich mRNAs. *J. Biochem.* **166**, 29–40 (2019).
80. Rodnina, M. V. The ribosome in action: Tuning of translational efficiency and protein folding. *Protein Sci.* **25**, 1390–1406 (2016).
81. Choi, J. *et al.* How Messenger RNA and Nascent Chain Sequences Regulate Translation Elongation. *Annu. Rev. Biochem.* **87**, 421–449 (2018).
82. Samatova, E., Daberger, J., Liutkute, M. & Rodnina, M. V. Translational Control by Ribosome Pausing in Bacteria: How a Non-uniform Pace of Translation Affects Protein Production and Folding. *Front. Microbiol.* **11**, 619430 (2020).

83. Kehrenberg, C., Aarestrup, F. M. & Schwarz, S. IS21-558 insertion sequences are involved in the mobility of the multiresistance gene *cfr*. *Antimicrob. Agents Chemother.* **51**, 483–487 (2007).
84. Deshpande, L. M. *et al.* Detection of a New *cfr*-Like Gene, *cfr*(B), in *Enterococcus faecium* Isolates Recovered from Human Specimens in the United States as Part of the SENTRY Antimicrobial Surveillance Program. *Antimicrob. Agents Chemother.* **59**, 6256–6261 (2015).
85. Marín, M. *et al.* *Clostridium difficile* isolates with high linezolid MICs harbor the multiresistance gene *cfr*. *Antimicrob. Agents Chemother.* **59**, 586–589 (2015).
86. Hansen, L. H. & Vester, B. A *cfr*-like gene from *Clostridium difficile* confers multiple antibiotic resistance by the same mechanism as the *cfr* gene. *Antimicrob. Agents Chemother.* **59**, 5841–5843 (2015).
87. Pang, S. *et al.* Linezolid-resistant ST872 *Enterococcus faecium* harbouring *optrA* and *cfr* (D) oxazolidinone resistance genes. *Int. J. Antimicrob. Agents* **55**, 105831 (2020).
88. Schwarz, S. *et al.* Mobile Oxazolidinone Resistance Genes in Gram-Positive and Gram-Negative Bacteria. *Clin. Microbiol. Rev.* **34**, e0018820 (2021).
89. Stojković, V. *et al.* *cfr*(B), *cfr*(C), and a New *cfr*-Like Gene, *cfr*(E), in *Clostridium difficile* Strains Recovered across Latin America. *Antimicrob. Agents Chemother.* **64**, (2019).
90. Wiegand, I., Hilpert, K. & Hancock, R. E. W. Agar and broth dilution methods to determine the minimal inhibitory concentration (MIC) of antimicrobial substances. *Nat. Protoc.* **3**, 163–175 (2008).
91. Zhou, K. *et al.* Novel reference genes for quantifying transcriptional responses of *Escherichia coli* to protein overexpression by quantitative PCR. *BMC Mol. Biol.* **12**, 18

- (2011).
92. Pfaffl, M. W. A new mathematical model for relative quantification in real-time RT-PCR. *Nucleic Acids Res.* **29**, e45 (2001).
 93. Mohammad, F. & Buskirk, A. R. Protocol for Ribosome Profiling in Bacteria. *Bio Protoc* **9**, (2019).
 94. Pringle, E. S., McCormick, C. & Cheng, Z. Polysome Profiling Analysis of mRNA and Associated Proteins Engaged in Translation. *Curr. Protoc. Mol. Biol.* **125**, e79 (2019).
 95. Mehta, P., Woo, P., Venkataraman, K. & Karzai, A. W. Ribosome Purification Approaches for Studying Interactions of Regulatory Proteins and RNAs with the Ribosome. in *Bacterial Regulatory RNA: Methods and Protocols* (ed. Keiler, K. C.) 273–289 (Humana Press, 2012).
 96. Khusainov, I. *et al.* Structure of the 70S ribosome from human pathogen *Staphylococcus aureus*. *Nucleic Acids Res.* **45**, 1026 (2017).
 97. Khatter, H., Myasnikov, A. G., Natchiar, S. K. & Klaholz, B. P. Structure of the human 80S ribosome. *Nature* **520**, 640–645 (2015).
 98. Zheng, S. Q. *et al.* MotionCor2: anisotropic correction of beam-induced motion for improved cryo-electron microscopy. *Nat. Methods* **14**, 331–332 (2017).
 99. Zhang, K. Gctf: Real-time CTF determination and correction. *J. Struct. Biol.* **193**, 1–12 (2016).
 100. Scheres, S. H. W. RELION: implementation of a Bayesian approach to cryo-EM structure determination. *J. Struct. Biol.* **180**, 519–530 (2012).
 101. Punjani, A., Rubinstein, J. L., Fleet, D. J. & Brubaker, M. A. cryoSPARC: algorithms for rapid unsupervised cryo-EM structure determination. *Nat. Methods* **14**, 290–296 (2017).

102. Grant, T., Rohou, A. & Grigorieff, N. cisTEM, user-friendly software for single-particle image processing. *eLife* vol. 7 (2018).
103. Emsley, P., Lohkamp, B., Scott, W. G. & Cowtan, K. Features and development of Coot. *Acta Crystallographica Section D Biological Crystallography* vol. 66 486–501 (2010).
104. Adams, P. D. *et al.* PHENIX: a comprehensive Python-based system for macromolecular structure solution. *Acta Crystallogr. D Biol. Crystallogr.* **66**, 213–221 (2010).
105. Moriarty, N. W., Grosse-Kunstleve, R. W. & Adams, P. D. electronic Ligand Builder and Optimization Workbench (eLBOW): a tool for ligand coordinate and restraint generation. *Acta Crystallogr. D Biol. Crystallogr.* **65**, 1074–1080 (2009).
106. Chen, V. B. *et al.* MolProbity: all-atom structure validation for macromolecular crystallography. *Acta Crystallogr. D Biol. Crystallogr.* **66**, 12–21 (2010).
107. Yang, J. & Zhang, Y. I-TASSER server: new development for protein structure and function predictions. *Nucleic Acids Res.* **43**, W174–81 (2015).
108. Lorenz, R. *et al.* ViennaRNA Package 2.0. *Algorithms Mol. Biol.* **6**, 26 (2011).
109. Edgar, R. C. MUSCLE: a multiple sequence alignment method with reduced time and space complexity. *BMC Bioinformatics* **5**, 113 (2004).

Chapter 3

Structural basis for context-specific inhibition of translation by oxazolidinone antibiotics

Abstract

The antibiotic linezolid, the first clinically approved member of the oxazolidinone class, inhibits translation of bacterial ribosomes by binding to the peptidyl transferase center. Recent work has demonstrated that linezolid does not inhibit peptide bond formation at all sequences but rather acts in a context-specific manner, namely when alanine occupies the penultimate position of the nascent chain. However, the molecular basis for context-specificity has not been elucidated. Here we show that the second-generation oxazolidinone radezolid also induces stalling with a penultimate alanine and determined high-resolution cryo-EM structures of linezolid- and radezolid-stalled ribosome complexes to explain this mechanism of action. These structures reveal that the alanine side chain fits within a small hydrophobic crevice created by oxazolidinone, resulting in improved ribosome binding. Modification of the ribosome by the antibiotic resistance enzyme Cfr disrupts stalling due to repositioning of the modified nucleotide. Together, our findings provide molecular understanding for context-specificity of oxazolidinones.

Introduction

During translation, peptide bond formation occurs in the peptidyl transferase center (PTC) of the ribosome. The PTC is located within the large ribosomal subunit and catalyzes extension of the polypeptide chain through proper positioning of the peptidyl-tRNA in the P-site and aminoacyl tRNA in the A-site. Due to its functional importance, the PTC of the bacterial ribosome is a common target for antibiotics that inhibit translation^{1,2}.

The PTC antibiotic linezolid (LZD, **Figure 3.1a**) was the first clinically approved member of the synthetic oxazolidinone class of antibiotics³. Linezolid is used to treat drug-resistant gram-positive infections including those caused by methicillin-resistant *S. aureus* and vancomycin-

resistant Enterococci⁴. Initial cross-linking experiments identified the binding site for linezolid within the PTC A-site only when performed with actively translating ribosomes^{5,6}, suggesting that other translation components may be involved in linezolid binding. However, existing structures of linezolid-bound ribosomes have been obtained with ribosomes devoid of charged tRNAs^{7,8} or ribosomes containing a P-site tRNA lacking a nascent chain⁹. Recent evidence obtained through ribosome profiling and single-molecule studies demonstrated that linezolid does not indiscriminately inhibit the formation of every peptide bond but rather interferes with translation at certain mRNA sites^{10,11}. Robust inhibition of translation and ribosome stalling by linezolid is strongly favored when the amino acid alanine occupies the penultimate, (-1), position within the nascent chain. Together, these results suggest that interactions between linezolid and the nascent peptide may be important for stabilizing antibiotic binding to the ribosome. However, the exact nature of these interactions is yet to be elucidated.

Despite the clinical success of LZD, emerging resistance mechanisms have threatened its clinical utility. Such mechanisms of resistance include alteration of ribosomal RNA (rRNA) and ribosomal proteins^{12,13} and ribosome protection through ABC-F proteins¹⁴. A prevalent form of transferable resistance to LZD is the rRNA-modifying enzyme Cfr, which methylates the ribosome within the PTC to perturb antibiotic binding¹⁵⁻¹⁷. Emerging resistance sparked the development of second-generation oxazolidinone derivatives, such as radezolid (RZD), with improved potency¹⁸. Radezolid (**Figure 3.1a**) is in clinical development for bacterial acne and community-acquired pneumonia¹⁹. Compared to linezolid, radezolid retains the aryl-oxazolidinone core (rings A and B) and C5 group but has alterations to the C/D ring system. Given that key chemical elements are conserved between LZD and RZD it is plausible that RZD can also act as a context-specific inhibitor of translation. The importance of both conserved and distinct structural features of second

generation oxazolidinones to translation inhibition and context specificity, if any, is yet to be determined.

In this work, we discovered that RZD exhibits ribosome stalling behavior similar to that of LZD, arresting translating ribosomes when alanine occupies the penultimate position within the nascent peptide chain. Capitalizing on the stalling preference of these two antibiotics, we generated high resolution cryo-EM structures of LZD- and RZD-stalled ribosome complexes. Direct comparison of the drug-stalled translation complexes with the structures of the vacant ribosomes bound to the same antibiotics enabled identification of molecular contacts that improve oxazolidinone binding to the ribosome. Specifically, we find that the penultimate alanine fits within a shallow hydrophobic pocket created by the oxazolidinone molecules, providing structural rationale for context specificity and highlighting the role of the growing peptide chain in antibiotic binding. Our analysis of RZD action on ribosomes modified by the oxazolidinone resistance enzyme Cfr and the structure of RZD bound to the Cfr-modified ribosome provides the first insights into how this second generation oxazolidinone interacts with a LZD-resistant ribosome.

Results

LZD and RZD have similar ribosome stalling behavior

Previous *in vitro* toe-printing experiments have demonstrated that LZD induces ribosome stalling on a model mRNA sequence when the amino acid alanine is located in the penultimate (-1) position of the nascent polypeptide chain^{10,11} (**Figure 3.1b**). LZD-induced ribosome stalling is abolished when the penultimate alanine is replaced with tyrosine (**Figure 3.1b**). To evaluate if the second generation oxazolidinone RZD shows similar stalling behavior, we carried out *in vitro*

toeprinting analysis to monitor the position of stalled ribosomes on the previously described mRNAs encoding the peptide sequences MFKAFKNIIRRTL and MFKYFKNIIRRTL¹¹.

Similarly to LZD, the presence of RZD permits formation of the first peptide bond with both mRNA transcripts as templates (**Figure 3.1b**). This result indicates that RZD is likely not a universal inhibitor of translation and also may not act as an initiation inhibitor as suggested for LZD by some earlier studies²⁰. While no inhibition of translation at the early mRNA codons was observed on the MFKYFK-encoding template, presence of RZD or LZD led to selective stalling of the ribosome during translation of the MFKAFK-encoding template. The stalling occurred at the F5 codon when an alanine residue was in the penultimate position within the nascent peptide chain. These results indicate that RZD- or LZD- bound ribosomes are unable to catalyze peptide bond formation between F5 and K6 when the MFKAF nascent peptide occupies the exit tunnel. Comparison of the relative intensity of the stalled ribosome toeprint bands suggests that RZD is a stronger inducer of ribosome stalling than LZD (**Figure 3.1c**). The observation that RZD is unable to stall the ribosome if the critical alanine residue is replaced with a tyrosine (MFKYF) is consistent with the specificity of action of LZD (**Figure 3.1b**).

Formation of stalled ribosome complexes and cryo-EM analysis

Guided by the *in vitro* stalling behavior, we designed a stalling peptide to capture LZD and RZD stalled ribosome complexes (SRC) for structural analysis, herein referred to as LZD-SRC and RZD-SRC, respectively. Stalled complexes were generated by conducting coupled *in vitro* transcription-translation reactions with *E. coli* ribosomes in the presence of oxazolidinone antibiotics (**Figure 3.2a**). To favor SRC formation at the F5 codon, we designed the template such that the open reading frame encoding the MFKAF stalling peptide was truncated after the F5 codon

(**Figure 3.2a**). 70S SRCs were purified away from other components of the translation reaction by sucrose gradient fractionation and vitrified on carbon grids for cryo-EM analysis. Refinement and reconstruction were performed using the cisTEM software suite²¹ to obtain 2.5 Å resolution structure of LZD-SRC and 2.5 Å resolution of RZD-SRC (**Figure 3.2b**, **Figure 3.3**, **Table 3.1**).

The generated cryo-EM maps of LZD-SRC and RZD-SRC have well-defined densities for the oxazolidinone antibiotic and rRNA nucleotides, especially those within the PTC. Both cryo-EM maps also have distinct densities for the peptidyl-tRNA located in the P-site. No A-site or E-site tRNAs are present. Modeling of the peptidyl-tRNA structure within the density maps unambiguously assigns the penultimate residue of the nascent peptide as alanine, as expected based on the mRNA template used in the experiment (**Figure 3.2**). This assignment is further supported by cryo-EM densities corresponding to the mRNA:tRNA interaction because $\text{UUC}_{\text{mRNA}}:\text{GAA}_{\text{tRNA-Phe}}$ offers a better fit than $\text{GCA}_{\text{mRNA}}:\text{UGC}_{\text{tRNA-Ala}}$ (**Figure 3.4**).

To directly compare how presence of the nascent peptide may influence positioning of the antibiotic and/or conformation of rRNA nucleotides, we also generated structures of vacant *E. coli* 70S ribosomes in complex with LZD or RZD alone, herein referred to as LZD-70S and RZD-70S, at 2.4 Å resolution and 2.5 Å resolution, respectively (**Figure 3.3**, **Table 3.1**). Similarly to the stalled complexes, antibiotic-only bound structures have unambiguous densities for the oxazolidinone antibiotic (**Figure 3.5a,b**).

The penultimate alanine facilitates antibiotic binding

The overall binding modes of LZD and RZD within the PTC in antibiotic-only bound and in SRC are similar to those described previously^{7-9,22} (**Figure 3.6**). The binding mode of LZD and RZD is also similar to that of other oxazolidinone derivatives²²⁻²⁶, including contezolid and

cadazolid, of which the cadazolid structure also contains a P-site tRNA (**Figure 3.6**). The fluorophenyl moiety (B-ring) sits in the A-site cleft, a hydrophobic pocket formed by splayed out nitrogen bases of nucleotides C2452 and A2451 (**Figure 3.6**). The oxazolidinone ring (A-ring) of LZD and RZD is positioned in an offset π - π stacking interaction with Ψ 2504. Interestingly, we find that the carbonyl of the oxazolidinone ring does not interact with rRNA but is rather chelated to a solvent molecule or ion (**Figure 3.7a,b**), corroborating previous SAR studies that demonstrated the importance of an electron-pair donor for activity²⁷.

The binding poses for both LZD and RZD are near-identical between the antibiotic-only and stalled-ribosome structures (**Figure 3.7c,d**). We do, however, observe improved density for both antibiotics in SRC, suggesting that presence of the stalling nascent peptide stabilizes the placement of LZD and RZD in the ribosome (**Figure 3.5a,b**). Specifically, we observe improved density for the C5 acetamide group for both antibiotics, as well as enhanced density for the D-ring of RZD in the SRC structure. Of note, in previously published density maps of oxazolidinones bound to vacant ribosomes^{7-9,22}, the acetamide is less well resolved and has been modeled in a variety of positions, likely due to its ability to sample multiple conformations (**Figure 3.6**). Our structures suggest that the nascent peptide present in the SRC stabilizes the C5 group, thereby providing a more biologically relevant view on drug placement.

The nascent protein chain, and more specifically, the penultimate Ala residue, contributes directly to formation of the drug binding site (**Figure 3.2b**, **Figure 3.5c,d**). In contrast to the orientation of the flanking residues within the nascent peptide, the side chain of the penultimate alanine faces towards the oxazolidinone. In this orientation, the methyl group of alanine fits snugly within the hydrophobic crevice formed by the C5 group and A/B-ring system of the antibiotic. The crevice is deep enough to accommodate the small side chain of alanine, but is too shallow to fit

bulkier side chains, including that of tyrosine, providing rationale for the differential stalling preferences observed in our toeprinting experiments (**Figure 3.1b**). In the stalled complex, the alanine's side chain methyl group engages in a CH- π interaction with the aryl B-ring of the oxazolidinone (3.6 Å and 3.9 Å between C atom and plane of the B-ring for LZD-SRC and RZD-SRC, respectively) (**Figure 3.5c-f**). This interaction likely facilitates antibiotic binding to the A-site of the PTC, resulting in enhanced occlusion of incoming aminoacyl tRNAs. Glycine, the smallest amino acid residue which lacks a side chain, would not clash with the ribosome-bound antibiotic when present in the penultimate position of the nascent peptide, yet it is not favored for drug-induced ribosome stalling^{10,11}. The inability of glycine to form the alanine-specific CH- π interaction with the drug molecule likely explains this observation.

A similar CH- π interaction has been recently observed between the penultimate alanine and aryl ring of chloramphenicol (CHL), another PTC-targeting antibiotic that also exhibits context-specific inhibition of translation²⁸. Superposition with the CHL complex reveals significant overlap between the aryl groups of CHL and LZD and acquire similar positioning with respect to the penultimate alanine of the nascent peptide, suggesting that these antibiotics likely exploit the same interaction to achieve context specificity (**Figure 3.8**). In contrast to CHL, which also induces robust ribosome stalling when serine or threonine occupy the penultimate position, LZD exhibits a notably stronger preference for alanine¹⁰. While *in silico* modeling of serine or threonine at the penultimate position in LZD-SRC reveals that serine can be accommodated, the methyl group of threonine generates a steric clash for all favored rotamers (**Figure 3.9**). Recent work hypothesized that CHL-induced stalling with serine in the penultimate position of the nascent peptide is stabilized by a H-bond between the serine hydroxyl and chlorine atom of CHL²⁸. Since the C5 group of LZD does not have an analogous electron-pair donor, it is likely that the unsatisfied

H-bond acceptor, rather than sterics, accounts for LZD's strong preference for alanine over serine. Interestingly, these results suggest that previously developed LZD derivatives with C5 substitutions to more polar groups²⁶, such as LZD-5 which contains a dichloroacetamide moiety similar to CHL, may exhibit expanded stalling profiles.

Additional interactions with rRNA nucleotides

In LZD and RZD antibiotic-only 70S structures, the exit tunnel nucleotide A2062 can adopt two distinct conformations (**Figure 3.5g**). In its dominant conformation the A2062 base projects into the lumen of the exit tunnel, while in the minor conformation, A2062 is rotated and lays flat against the tunnel wall. Strikingly, in the stalled ribosome complexes with the nascent protein chain occupying the tunnel, the A2062 base is found only in the rotated state juxtaposed against the wall of the tunnel (**Figure 3.5h, Figure 3.10a**). The rotated state of A2062 is stabilized by a H-bond between the N1 atom of adenine and the stalling peptide backbone, as well as a non-canonical A:A base-pair with m²A2503 (**Figure 3.10b**). The non-canonical A:A base-pair is also observed in ribosome structures containing the context-specific inhibitor CHL and a penultimate alanine/threonine-containing peptide²⁸. Interestingly, the interaction between A2503 and A2602 was previously found to be essential for macrolide-induced stalling of bacterial ribosomes²⁹⁻³¹ and is also a critical interaction for drug-like molecule PF846-mediated selective inhibition of translation termination in human ribosomes³². In this conformation, the exocyclic amine of A2062 is within H-bonding distance of the acetamide carbonyl of LZD/RZD (3.0 Å/3.3 Å), which likely explains why we observe improved density for the C5 group in the stalled complexes (**Figure 3.5a,b**). This interaction has not been observed in existing structures of LZD/RZD-bound vacant ribosomes due to the alternative orientation of A2062. The peptide-induced interaction between

A2062 and the oxazolidinone is distinct from that observed with CHL. In a structure of the ribosome-CHL complex that lacks the nascent peptide, A2062 is already in a rotated state to form a H-bond with the antibiotic³³.

Compared to the oxazolidinone-only bound structures, we also observe stabilization of several dynamic PTC nucleotides in conformations that favor additional contacts with the antibiotics. We observe improved density for U2585, which as the C4 enol tautomer could provide a H-bonding interaction with the oxygen atom of the morpholine ring in LZD (**Figure 3.10c,e, Figure 3.11**). Although U2506 does not make direct contact with LZD, we observe dramatically improved density for this nucleotide in a conformation analogous to an uninduced or nonproductive state of the PTC³⁴ (**Figure 3.10c, Figure 3.11**). In the RZD-stalled complex, we observe improved densities for U2506, U2585 and A2602 (**Figure 3.11**). U2506 and A2602 provide π - π stacking interactions with the C- and D-ring, respectively, while U2585 engages in a H-bond with the secondary amine of RZD (**Figure 3.5b, Figure 3.10d,f**). Interestingly, the D-ring interaction with A2602 was not observed in a previous ribosome structure with RZD²² but has been observed in structures with oxazolidinones containing other D-ring substituents^{23,24} (**Figure 3.5e,f**). The additional interaction with A2602 likely explains why RZD is a better inhibitor of translation compared to LZD, as the stabilized D-ring would account for improved drug binding and provide additional steric interference with incoming aminoacyl tRNAs (**Figure 3.12**). Together these results suggest that, in addition to favorable interactions with the penultimate alanine, interactions between otherwise dynamic rRNA nucleotides and the oxazolidinone likely play a role in improving antibiotic binding to the ribosome to facilitate stalling.

Cfr methylation perturbs the stalled ribosome complex

A prevalent resistance mechanism to LZD identified in multiple clinical isolates worldwide^{35–40} involves methylation of rRNA by the Cfr enzyme, which adds a methyl group at the C8 atom of A2503 (m⁸A2503) in 23S rRNA^{15,17,41–43}. It has been speculated that the Cfr modification disrupts LZD binding to the ribosome by introducing a steric clash between the installed methyl mark and the C5 group of the antibiotic. While this modification confers high levels of resistance to LZD, RZD retains modest efficacy against Cfr-positive strains^{44,45} (**Figure 3.13a**), likely due to retained interactions on the other side of the molecule involving the D-ring (**Figure 3.5b**). However, this suggests that binding of RZD to Cfr-modified ribosomes would require structural changes, such as the C5 group of RZD adopting an alternative conformation to accommodate the C8 methyl group of m⁸A2503 or shifting of the modified nucleotide to open room for the C5 side chain. Given that positioning of both the C5 group and A2503 may influence context specificity, we wanted to evaluate the ability of RZD to induce stalling of Cfr-modified ribosomes.

To perform *in vitro* assays, we expressed Cfr in *E. coli* and isolated ribosomes with near-complete methylation of m⁸A2503 as described previously⁴³. As expected, RZD retains considerable activity against the m⁸A2503 ribosomes. *In vitro* translation of sf-GFP by Cfr-modified ribosomes was barely affected by LZD but could be inhibited by RZD albeit with some loss in potency (IC₅₀ = 0.9 μM for wild-type and IC₅₀ = 4.9 μM for Cfr-modified (**Figure 3.13b**)). Toeprinting experiments showed that, as expected, the m⁸A2503 modification considerably reduced LZD-dependent ribosome arrest at the F5 codon of the MFKAF...-encoding ORF (**Figure 3.14a**). Strikingly, RZD, while retaining its general translation inhibitory activity, was notably less efficient in arresting the m⁸A2503 ribosome at the F5 codon of the MFKAF template (**Figure**

3.14a). Qualitatively similar results were observed when we performed toeprinting analysis using the sf-GFP coding sequence as a template. LZD and RZD induced stalling of unmodified ribosomes at several specific sites within the sf-GFP coding sequence. LZD-mediated stalling was essentially eliminated when translation was driven by Cfr-modified ribosomes. In contrast, RZD retained its ability to cause stalling of the Cfr-modified ribosomes, albeit with diminished efficiency (**Figure 3.13c**). These results suggest that RZD remains a good inhibitor of Cfr-modified ribosomes because causing weak stalling at multiple sites within the mRNA ORFs would still be sufficient to inhibit expression of most cellular proteins. Together, these results suggest that presence of the C8 methyl group at A2503 does not completely prevent binding of RZD but partially diminishes its ability to arrest translation in the alanine-specific manner.

In search of a molecular explanation for this result, we determined the structure of a RZD-stalled Cfr-modified ribosome containing the MFKAF-tRNA in the P-site at 2.4 Å resolution (**Table 3.1, Figure 3.3**). While the binding mode of the antibiotic is near-identical to that observed in the stalled wild-type (WT) ribosome, m⁸A2503 is shifted away from RZD to accommodate the C5 group (**Figure 3.14b-d**). A2503 positioning is also distinct from that observed in vacant Cfr-modified ribosomes, suggesting that repositioning is due to RZD accommodation and not due to C8 methylation per se (**Figure 3.13d**). While the penultimate alanine is able to retain the CH- π interaction with RZD, the Cfr modification encroaches on the antibiotic binding pocket so that binding of RZD faces the increased energy barrier of partially displacing m⁸A2503 relative to its position observed in the unmodified SRC (**Figure 3.14b-d**). The increased packing requirements of the alanine side chain, antibiotic, and A2503 with the addition of the C8-methyl group (**Figure 3.13e**) likely restricts conformational flexibility between these components to diminish formation

of a stable stalled complex. Indeed, some destabilization of the SRC is revealed by poor density for certain side chains of the nascent peptide (**Figure 3.15**).

Strikingly, we also find that A2062 adopts a single observable conformation within the lumen of the exit tunnel, which is now positioned too far away to engage in an H-bond with RZD (**Figure 3.14b**, **Figure 3.16**). This is distinct from the stalled WT complex, where A2062 is found in the rotated conformation against the tunnel wall and is also distinct from the RZD-only bound complex where both conformations are observed (**Figure 3.16**). Given that the noncanonical A:A base-pair with A2503 is likely involved in stabilizing the rotated state of A2062, the shifted position of m⁸A2503 may contribute to reversion of A2062 to the lumen conformation. Interestingly, perturbation of the same A:A interaction has also been shown to disrupt macrolide-dependent ribosome stalling³¹.

Our structural findings also provide important insights into how RZD retains efficacy against LZD-resistant ribosomes. While the Cfr modification of A2503 perturbs H-bonding between the antibiotic and A2062, we note retention of other interactions. Although somewhat diminished, we observe densities for the D-ring and A2602 engaged in a π - π stacking interaction analogous to that observed in the WT, non-Cfr modified complex (**Figure 3.14e**). Because LZD does not contain the additional D-ring, its binding is more dramatically impacted by steric occlusion by m⁸A2503 and/or the lost interaction with A2062. Our results suggest that in addition to shortening of the C5 group, which has been carried out with other oxazolidinones derivatives^{19,24,46}, extension of the ring system on the opposite end of the molecule is an orthogonal, viable strategy for generating oxazolidinone antibiotics that overcome Cfr resistance. The combination of both approaches has been showcased in the development of tedizolid and

cadazolid, both of which exhibit potent antimicrobial activity against Cfr-containing, linezolid-resistant strains^{24,47}.

Discussion

We identified two factors that contribute to context specificity of oxazolidinones LZD and RZD. While the antibiotic can still bind to the ribosome that lacks the nascent protein chain, as revealed by our and previously published structures of the vacant ribosome complexed with LZD and RZD, presence of the nascent chain stabilizes binding of the drug by providing additional points of contact. Most importantly, the side chain of the penultimate alanine residue is intercalated into the complementary-shaped cavity formed by the drug molecule (**Figure 3.2b**, **Figure 3.5c,d**, **Figure 3.17a,b**). Larger amino acids in the penultimate position of the nascent peptide would clash with the antibiotic, preventing its binding (**Figure 3.17a**). In contrast, glycine cannot make a CH- π interaction with the drug, thereby making its binding less favorable (**Figure 3.17a**). As a secondary effect of the alanine interaction, we also observe stabilization of dynamic nucleotides in conformations that provide additional contacts with the antibiotic (**Figure 3.10**, **Figure 3.11**). The culmination of these interactions leads to improved antibiotic binding to the ribosomal A-site in the presence of nascent peptides containing a penultimate Ala, facilitating competition with incoming aminoacyl tRNAs and thus resulting in ribosome stalling (**Figure 3.17a,b**).

Our structural investigations into RZD binding to a Cfr-modified ribosome revealed the importance of the D-ring in stabilizing ribosome engagement, providing insight into how RZD retains efficacy against Cfr modified ribosomes (**Figure 3.17c**). We find that although RZD loses some potency, which is consistent with diminished stalling on alanine-containing peptides, RZD remains an overall effective inhibitor of m⁸A2503 containing ribosomes. Our structural findings

suggest the Cfr modification likely diminishes RZD stalling by forcing an energetically-disfavorable repositioning of A2503, which also results in loss of an interaction between exit tunnel nucleotide A2062 and the drug (**Figure 3.17c**). In summary, our findings provide a unifying model for context-specific inhibition of translation by oxazolidinone antibiotics. Our observation that the antibiotic binding pocket is formed, in part, by the nascent peptide, has revealed the “missing” component of translation machinery involved in antibiotic binding from previous cross-linking experiments. The importance of Ala in the penultimate position of the nascent peptide for stabilizing the antibiotic provides the structural basis for context specificity observed in ribosome profiling and single molecule studies. Our structural insights into nascent-peptide specific inhibition of translation by oxazolidinones, and complementary work in related systems^{28,48-50}, suggests prospects for the development of drugs that can modulate activity of the ribosomes in a protein-selective manner.

Materials and Methods

Generation of DNA templates for PURExpress system

DNA templates were prepared by performing PCR reactions with AccuPrime Taq DNA Polymerase (Thermo Fisher). DNA templates used for toeprinting analysis were prepared by combining the following previously published primers¹¹: 100 μ M T7, 100 μ M NV1, 10 μ M SMFRET-Fwd, 10 μ M SMFRET-Rev, and either 10 μ M SMFRET-Mid(FKAFK) (for the MFKAFK... template) or 10 μ M SMFRET-Mid(FKYFK) (for the MFKYFK... template). DNA templates used for the generation of stalled ribosome complexes were prepared by combining the following primers: 100 μ M T7, 100 μ M ORF_SD, 10 μ M T7_MFKAF_Fwd, and 10 μ M SD_MFKAF_Rev. Primer sequences are listed in **Table 3.2**. The PCR product was purified using

the MiniElute PCR kit (Qiagen) following manufacturer's instructions and quality was confirmed using an 8% TBE (Novagen) gel. Sequence architecture of the resulting DNA product is outlined in **Table 3.2**.

Purification of 70S ribosomes

WT *E. coli* 70S ribosomes were purified from the MRE600 strain⁵¹. *E. coli* MRE600 were grown to mid-log phase in LB media at 37°C with shaking. Cfr-modified *E. coli* 70S ribosomes were purified from *E. coli* BW25113 expressing the evolved variant CfrV7⁴³. *E. coli* BW25113 transformed with pZA-encoded CfrV7 were grown to an OD₆₀₀ of ~0.7 in LB media containing ampicillin (100 µg/mL) and AHT inducer (30 ng/mL) at 37°C with shaking. Subsequent purification steps for WT and Cfr-modified ribosomes were identical. After lysis using a microfluidizer, clarified lysates were applied to a 32% w/v sucrose cushion. Tight-coupled 70S ribosomes were purified on a 15-30% w/v sucrose gradient. To eliminate sucrose, ribosomes were precipitated by the addition of PEG 20,000 and subsequently resuspended in buffer containing 50 mM Hepes-KOH (pH 7.5), 150 mM KOAc, 20 mM Mg(OAc)₂, 7 mM β-mercaptoethanol, 20 U/mL SuperASE-In.

Determination of antibiotic resistance

Antibiotic resistance was determined by broth microdilution following established protocols⁵². The *E. coli* strain BW25113 *acrB::kan*, where efflux component AcrB is replaced with a kanamycin resistance cassette, was used for resistance testing of oxazolidinones. In short, cultures of bacteria freshly transformed with empty pZA vector or pZA-encoded CfrV7 were grown at 37°C with shaking for approximately 2.5 h. Cultures were then diluted to 10⁶ cells and 50µL of

this dilution was dispensed into 96-well plates containing 50 μ L of LB media with antibiotic of interest, ampicillin (100 μ g/mL), kanamycin (50 μ g/mL), and AHT (30 ng/mL). Resistance was evaluated using 2-fold serial dilution of antibiotic with the following concentration ranges: linezolid (1-256 μ g/mL, Acros), radezolid (0.5-128 μ g/mL, Med Chem Express) The minimum inhibitory concentration (MIC) required to inhibit visible bacterial growth was determined after incubation at 37°C with shaking for 18 h. OD₆₀₀ values were also recorded with a microtiter plate reader (SpectraMax M5, Molecular Devices).

In vitro assays

Toeprinting assays were conducted as previously described^{11,49,53} using WT or Cfr-modified ribosomes purified as described above and previously⁵⁴. Briefly, reactions were prepared using the PURExpress Δ Ribosome Kit (New England Biolabs) in volumes of 5 μ L and were allowed to proceed for 15 min at 37 °C. Primer extension was initiated by the addition of AMV reverse transcriptase (New England Biolabs) and allowed to proceed for 10 min. All antibiotics were added to a final concentration of 50 μ M. Mupirocin is an Ile-tRNA synthetase inhibitor and was included in all toeprinting reactions so that any ribosomes not stalled at an upstream codon are forced to stall at the downstream hungry Ile codons.

The effect of antibiotics on protein expression was analyzed in a Δ Ribosome PURExpress cell-free transcription-translation system (New England Biolabs). The plasmid pY71⁵⁵ containing the *sf-gfp* gene under the control of T7 RNA polymerase promoter was used as a template. A typical reaction 5 μ L reaction, composed from the kit components as recommended by the manufacturer, contained 10 pmol of WT or Cfr-modified ribosomes isolated as described above⁵⁴. The reactions

were prepared on ice and then placed in the wells of a 384-well black wall/clear bottom plate. The plate was incubated at 37°C in the Tecan Infinite M200 Pro plate reader and progression of the reaction was monitored by following sf-GFP fluorescence (λ_{ex} 488 nm, λ_{em} 520 nm) over time.

Preparation of LZD- and RZD-only bound ribosomes for cryo-EM

Purified 70S WT or Cfr-modified ribosomes were diluted to 1 pmol/ μ L in buffer containing 50 mM Hepes-KOH (pH 7.5), 150 mM KOAc, 20 mM Mg(OAc)₂, 7 mM β -mercaptoethanol, 20 U/mL SuperASE-In. Diluted ribosomes (50 μ L) were then incubated at 4°C for 1.5 h after the addition of 3 μ L of either 1 mM linezolid (Med Chem Express) or 1 mM radezolid (Med Chem Express), yielding a final antibiotic concentration of 60 μ M (60X molar excess). Samples were then filtered for 5 min at 14,000 x g at 4°C using a 0.22 μ m low-binding Durapore PVDF filter (Millipore).

Preparation of stalled ribosome complexes for cryo-EM

Stalled ribosome complexes containing the stalling peptide and corresponding oxazolidinone antibiotic were prepared by *in vitro* transcription-translation. Reactions of 100 μ L volume were prepared using the PURExpress Δ Ribosome Kit (New England Biolabs, E3313S) containing 0.8 U/ μ L of SuperASE-In, ~1100 ng of DNA template encoding the stalling peptide sequence, 5000 pmol of linezolid (Med Chem Express) or radezolid (Med Chem Express), and 360 pmol of WT ribosomes or 250 pmol of Cfr-modified ribosomes. The reaction was halted by placing reactions on ice after incubation at 37°C for 1 h. The reaction was diluted to 190 μ L by the addition of Buffer C (50 mM Hepes-KOH-pH 7.5, 150 mM KOAc, 20 mM Mg(OAc)₂, 7 mM β -mercaptoethanol, 20 U/mL SuperASE-In) and purified by a 10-50% sucrose gradient also prepared in Buffer C.

Ultracentrifugation was performed using a SW Ti41 rotor (Beckman Coulter) at 60,000 x g for 16 h at 4°C. Gradients were fractionated using a Bio-Comp Fractionator in 20 fractions where absorbance at 260 nm was continuously monitored. Fractions corresponding to stalled ribosome complexes were precipitated by the slow addition of PEG 20,000 in Buffer C at 4°C to a final concentration of 8% w/v. Stalled complexes were isolated by centrifugation for 10 min at 17,500 x g at 4°C. After removing the supernatant, samples were slowly resuspended in Buffer C at 4°C. Sample concentration was determined by NanoDrop UV spectrophotometer (Thermo), where $A_{260}=1$ corresponds to 24 pmol of 70S ribosome. Purified stalled ribosome complexes (0.65 μ M Cfr-modified stalled ribosome complex or 2.2 μ M WT stalled ribosome complex) were then incubated with ~30X molar excess of radezolid (20 μ M for Cfr-modified stalled ribosome complexes and 60 μ M for WT stalled ribosome complex) for 1 h at 4°C. Purified WT stalled ribosome complexes (0.418 μ M) were incubated with >100X molar excess of linezolid (60 μ M) for 1 h at 4°C. Prior to freezing the grids, stalled ribosome complexes were filtered for 5 min at 14,000 x g at 4°C using a 0.22 μ m low-binding Durapore PVDF filter (Millipore).

Cryo-EM analysis

Samples described above were diluted in Buffer C and deposited onto freshly glow-discharged (EMS-100 Glow Discharge System, Electron Microscopy Sciences, 30 s at 15 mA) copper Quantifoil (Quantifoil Micro Tools GmbH) grids with 2 nm thick amorphous carbon on top. Grids were incubated for 30 s at 10 °C and 95% humidity, before blotting and vitrification by plunging into liquid ethane using a FEI Vitrobot Mark IV (ThermoFisher). Ice thickness was controlled by varying the blot time, using Whatman #1 filter paper for blotting. Grids were screened for ice quality using a FEI Talos Arctica electron microscope (ThermoFisher, 200 kV, at UCSF) before

grids were transported via dry shipper to other facilities or loaded into a UCSF FEI Titan Krios (ThermoFisher).

All datasets used for reconstruction were imaged on FEI Titan Krios microscopes (ThermoFisher, 300 kV). The LZD-70S and LZD-SRC datasets were collected at the Stanford-SLAC CryoEM Center (S²C²) using SerialEM on a microscope equipped with a Gatan K3 direct electron detector (DED) but without an imaging filter. The RZD-70S and RZD-SRC datasets were collected at the National Center for CryoEM Access and Training (NCCAT) using Leginon/Appion on a microscope equipped with a Gatan K2 Summit DED and an imaging filter (20 eV slit). The RZD-SRC* dataset was collected at UCSF on a microscope equipped with a Gatan K3 DED and an imaging filter (20 eV slit). The RZD-SRC* dataset was collected on-axis; all other datasets were collected using a nine-shot beam-image shift approach with coma compensation. All image stacks were collected in super-resolution mode. Pixel sizes, micrograph count, defocus values, and exposures varied slightly between facilities and are reported in **Table 3.1**.

All image stacks were binned by a factor of 2, motion corrected, and dose-weighted using UCSF MotionCor2⁵⁶. All reconstructions used dose-weighted micrographs. Initial CTF parameters were determined using CTFFIND4 within the cisTEM (v1.0.0-beta)²¹ software suite. Micrographs with poor CTF fits or crystalline ice were excluded. Unsupervised particle picking used a soft-edged disk template was followed by 2D classification in cisTEM. Initial and final particle counts are reported in **Table 3.1**. Only classes that clearly contained ice were omitted. An *ab initio* reconstruction was carried out in cisTEM on the RZD-SRC* dataset, which yielded a starting reference which was lowpass filtered and used as the initial reference for all five datasets. For SRC

datasets, multi-class Auto refinement in cisTEM was used to select for all particles that had tRNA present. After this, and all non-SRC datasets, were subjected to a two-class Auto refinement in cisTEM to classify between “good” particles and damaged “garbage” particles and high-frequency noise. The good classes were carried forward into single class Auto and manual refinement efforts, including per-particle CTF estimation. Care was taken not to increment the high-resolution cutoff in refinement to prevent overfitting. Unsharpened maps were used in model refinement and figure preparation. Pixel size was confirmed by comparison and cross-correlation between the resulting map and a crystallographically-derived ribosome structure. 70S maps were used for model building and figure preparation. Map resolution values are reported as particle Fourier Shell Correlation (FSC) at 0.143.

Atomic model building and refinement

Atomic models of 70S ribosome complexes with antibiotics and 70S stalled ribosome complexes were generated by rounds of model building in *Coot*⁵⁷, molecular dynamics model fitting in ISOLDE⁵⁸, and refinement in PHENIX⁵⁹. An initial model for all ribosome complexes was obtained by combining: (i) a model of WT *E. coli* 50S subunit (PDB 6PJ6)⁵²; (ii) a model of the 30S subunit from WT *E. coli* ErmBL-stalled ribosome structure (PDB: 5JU8)⁶⁰; (iii) P-tRNA and mRNA extracted from the ErmBL-stalled ribosome structure (PDB: 5JU8, mutated and remodeled in *Coot* to yield fully modified *E. coli* tRNA^{Phe} and a short mRNA, respectively); and (iv) the nascent peptide, which was modelled in *Coot*. Model refinement against the acquired LZD-SRC cryo-EM map was performed by multiple rounds of manual model building, molecular dynamics model fitting, and restrained parameter-refinement (rigid body fitting, real-space refinement, ADP refinement, and simulated annealing). Restraints for real space refinement of modified nucleotides

were generated using eLBOW⁶¹ within PHENIX⁵¹. For molecular dynamics, force fields for most modified nucleotides were available but inactive in standard releases of ISOLDE due to disfavored behavior under certain circumstances; these were toggled to active, and for nucleotides and the 4D4 amino acid without force fields available, the closest matching residue with force fields was substituted during molecular dynamics simulations as necessary. The antibiotics were held static for these simulations. The L3, L10 and L11 proteins were not modelled. Upon convergence of a satisfactory model in the LZD-SRC map, the same model was fit into the density in the other four maps, edited for chemical accuracy (removal of the peptidyl tRNA and mRNA from non-SRC models, and removal of any ions not supported by the map), and then subjected to further molecular dynamics and refinement cycles until convergence. Overall, protein residues and rRNA nucleotides show well refined geometrical parameters (**Table 3.1**). Figures were prepared using Pymol Molecular Graphics System Version 2.4.1 Schrödinger, LLC or UCSF ChimeraX Version 1.2.5⁶².

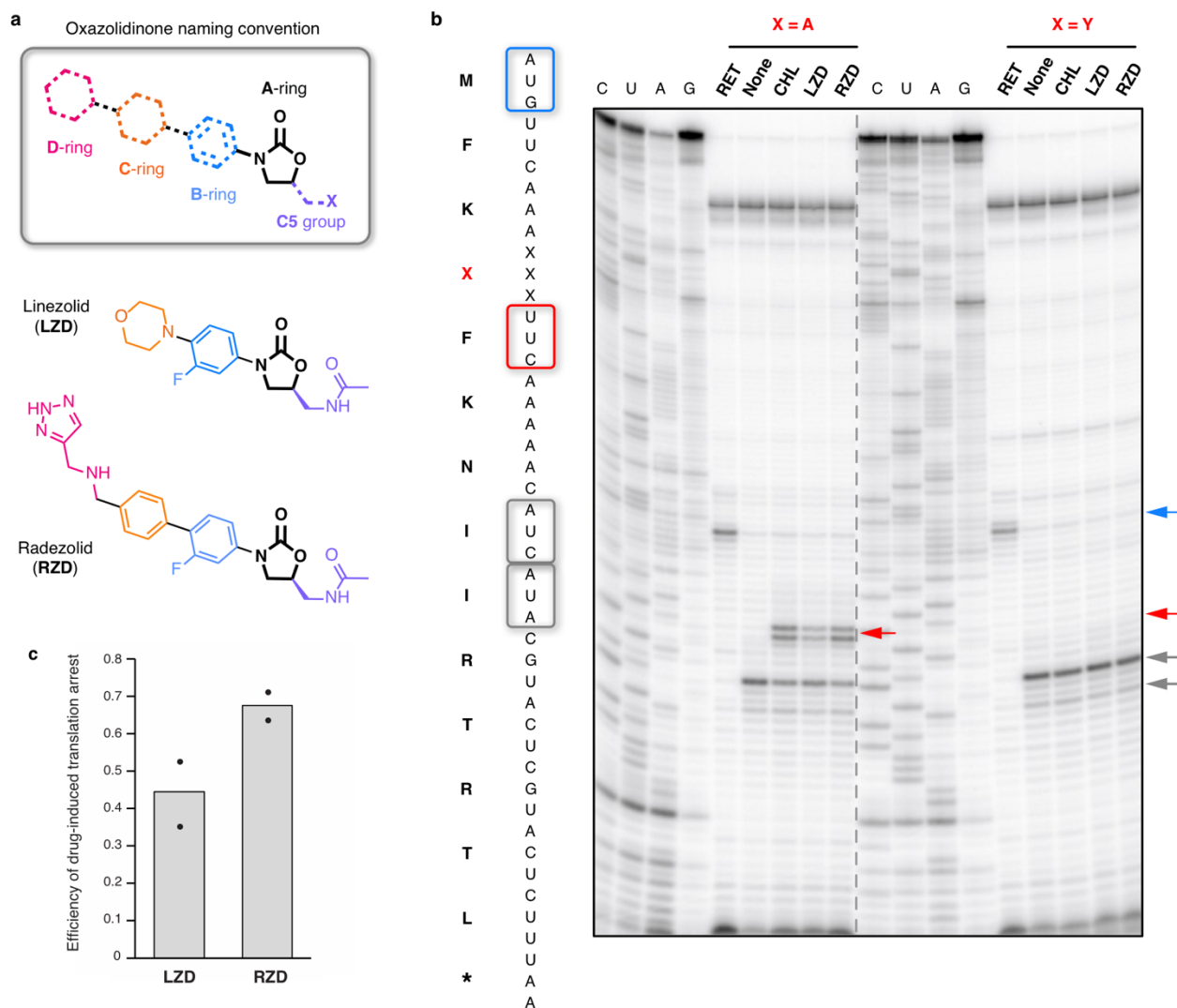


Figure 3.1 | Radezolid induces ribosome stalling with alanine in the penultimate position. (a) The oxazolidinone (A-ring) portion of the molecule is conserved amongst the oxazolidinone class and designated in black. Chemical moieties that vary amongst oxazolidinone derivatives, the C5-moiety, and B, C, and D rings, are designated by their respective color. (b) Toeprinting assays performed on model mRNAs encoding stalling and non-stalling peptides. The control antibiotic retapamulin (RET) was used to stall ribosomes at the start codon indicated by the blue arrow⁶³. ‘None’ designates reactions lacking ribosome-targeting antibiotics. The control antibiotic chloramphenicol (CHL) was used to stall with alanine at the penultimate position^{10,11}. The toeprint bands corresponding to prominent stall sites observed in reactions containing CHL, LZD, or RZD when the 4th amino acid is an alanine, but not tyrosine, are indicated by the red arrow. Due to the inclusion of the Ile-tRNA synthetase inhibitor mupirocin in all toeprinting reactions, any ribosomes not stalled at an upstream codon are trapped at the downstream Ile codons designated by grey arrows. All antibiotics were added to a final concentration of 50 μ M. The presented gel is representative of two independent experiments. c, Extent of translation inhibition by LZD and RZD calculated as the ratio of intensities of the drug-specific toeprint bands (red arrowhead, b) to the sum of intensities of the drug-specific and trap codon bands (grey arrowheads, b). The bar graph shows the mean of two independent experiments with individual data points.

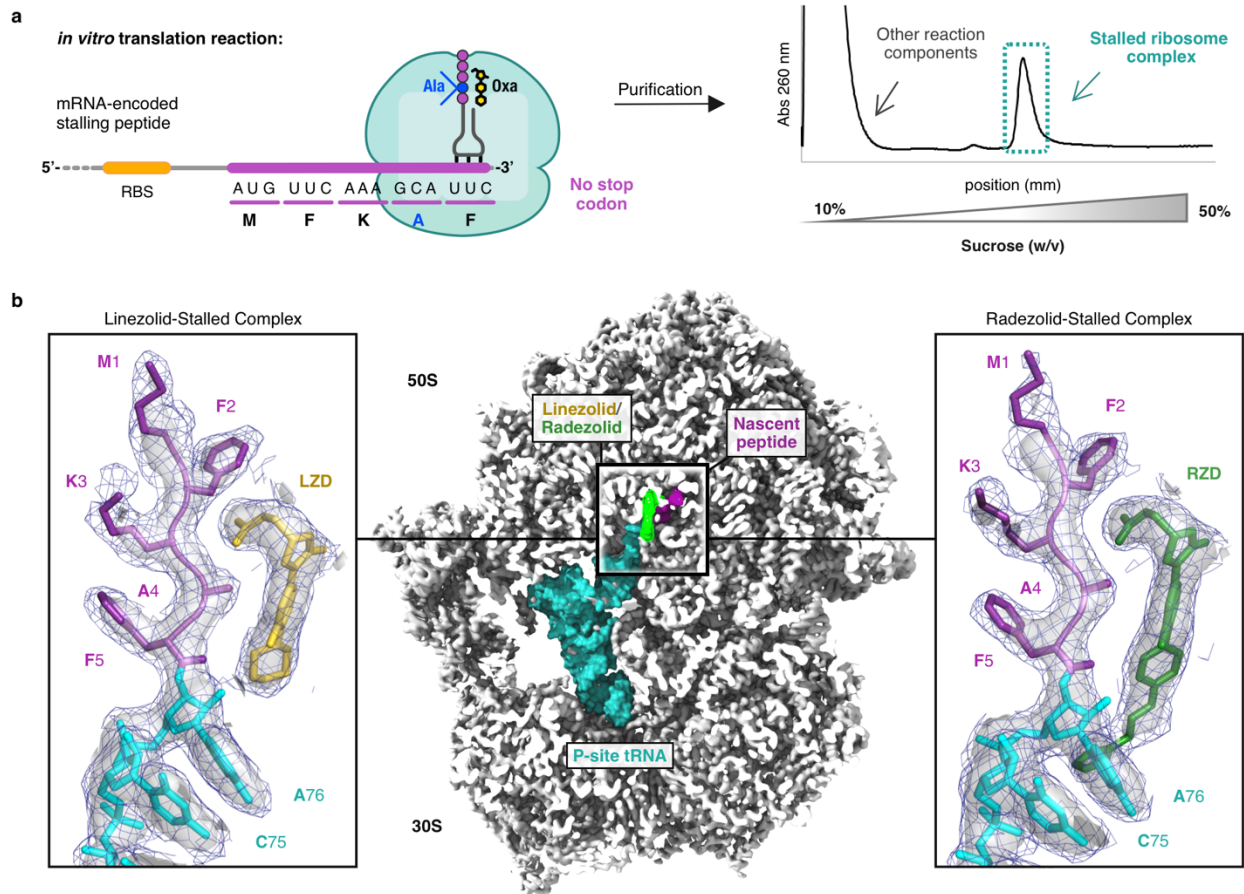


Figure 3.2 | Cryo-EM structures of linezolid and radezolid-stalled ribosome complexes. (a) Stalled complexes were generated by performing coupled *in vitro* transcription-translation reactions in the presence of the oxazolidinone (Oxa) antibiotic linezolid or radezolid. Complexes were further purified by sucrose gradient fractionation. **(b)** Cross-section of the cryo-EM density map of the stalled 70S ribosome in complex with peptidyl-tRNA and oxazolidinone. Inserts are close-up views of linezolid (LZD) or radezolid (RZD) in complex with the MFKAF nascent peptide. Coulomb potential density is contoured at 4.0σ in surface representation and 1.0σ in mesh representation. Figure was prepared using unsharpened cryo-EM density maps.

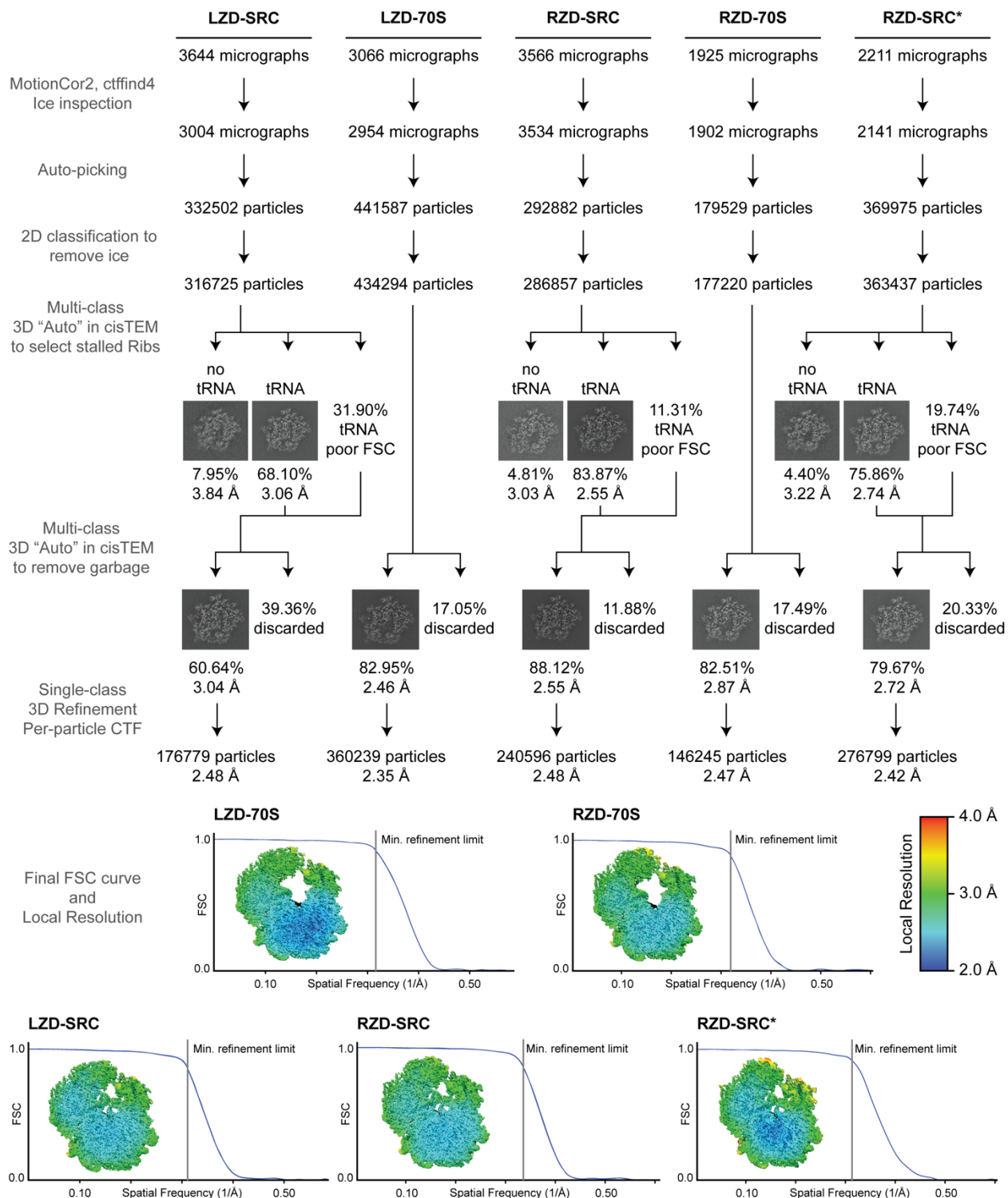


Figure 3.3 | Processing workflow, classification tree, FSC curves, and local resolution estimation for each map. Micrographs were CTF corrected and curated for ice quality, followed by unsupervised particle picking. 2D classification was used to remove residual ice particles, with all others subjected to multi-class 3D classification and refinement approaches to remove particles without tRNA (for SRCs) and select for good particles. Final FSC curves are presented along with center-slab representation of local resolution.

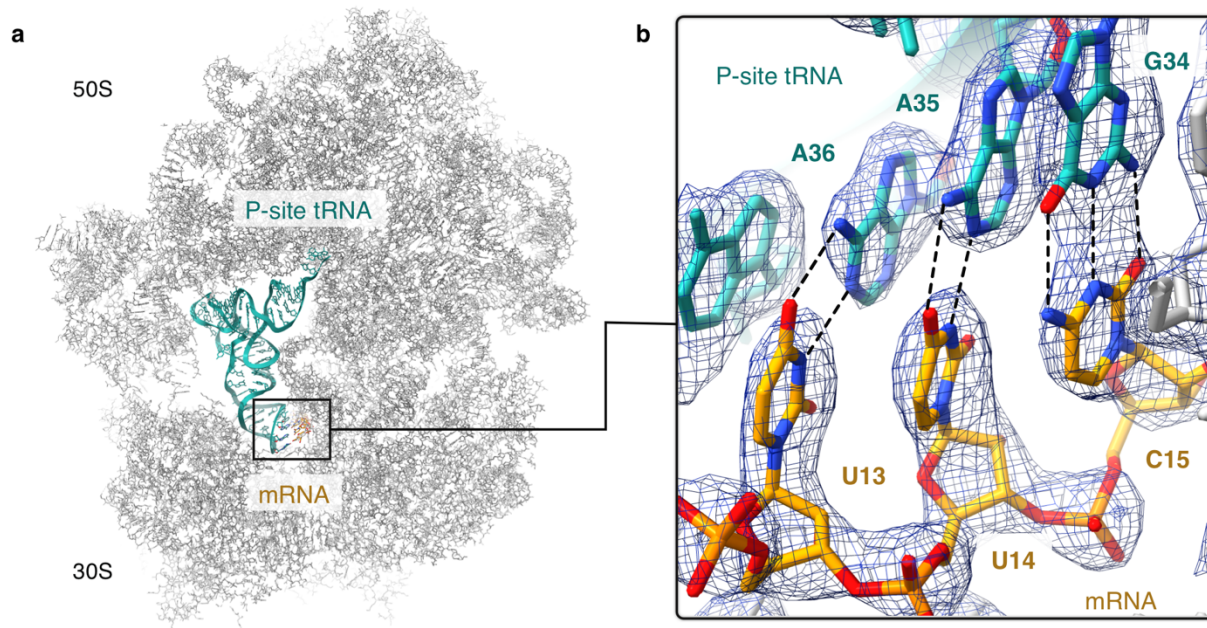


Figure 3.4 | Oxazolidinone-induced ribosome stalling at the Phe5 codon. (a) Location of the codon-anticodon interaction within the linezolid-stalled 70S ribosome complex. (b) Density for the codon-anticodon interaction is best modeled as $\text{UUC}_{\text{mRNA}}:\text{GAA}_{\text{tRNA-Phe}}$ rather than $\text{GCA}_{\text{mRNA}}:\text{UGC}_{\text{tRNA-Ala}}$ which would correspond to stalling at the upstream Ala4 codon. The figure was generated from unsharpened maps and the density is contoured at 4σ .

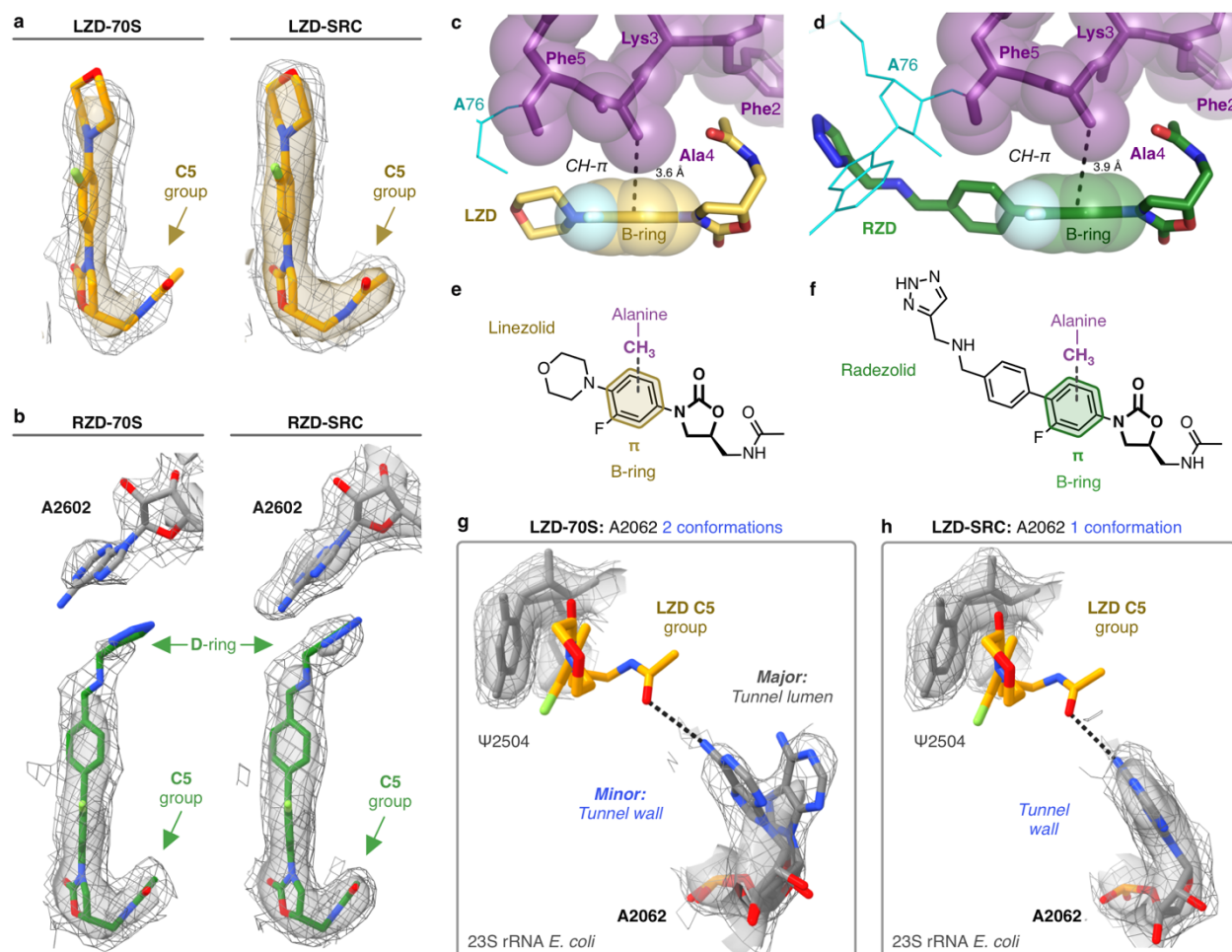


Figure 3.5 | Nascent peptide with penultimate alanine stabilizes oxazolidinone binding . For this figure, coulomb potential density is contoured at 4.0σ in surface representation and 1.0σ in mesh representation from unsharpened cryo-EM density maps. **(a)** Comparison of linezolid density in the linezolid-only bound (LZD-70S) and the linezolid-stalled complex (LZD-SRC). **(b)** Comparison of radezolid density in the radezolid-only bound (RZD-70S) and the radezolid-stalled complex (RZD-SRC). **(c)** Close up view of the CH- π interaction between the B-ring of LZD and the penultimate alanine (Ala4). **(d)** Close up view of the CH- π interaction between the RZD B-ring and the penultimate alanine. **(e)**, **(f)** Schematic of the CH- π interaction involved in stabilizing antibiotic binding in LZD-stalled (panel e) and RZD-stalled (panel f) ribosome complexes. **(g)** Density of the exit tunnel rRNA nucleotide A2062 in LZD-only bound structure, highlighting two conformations. **(h)** Density of A2062 in the LZD-stalled structure, with only one observed conformation.

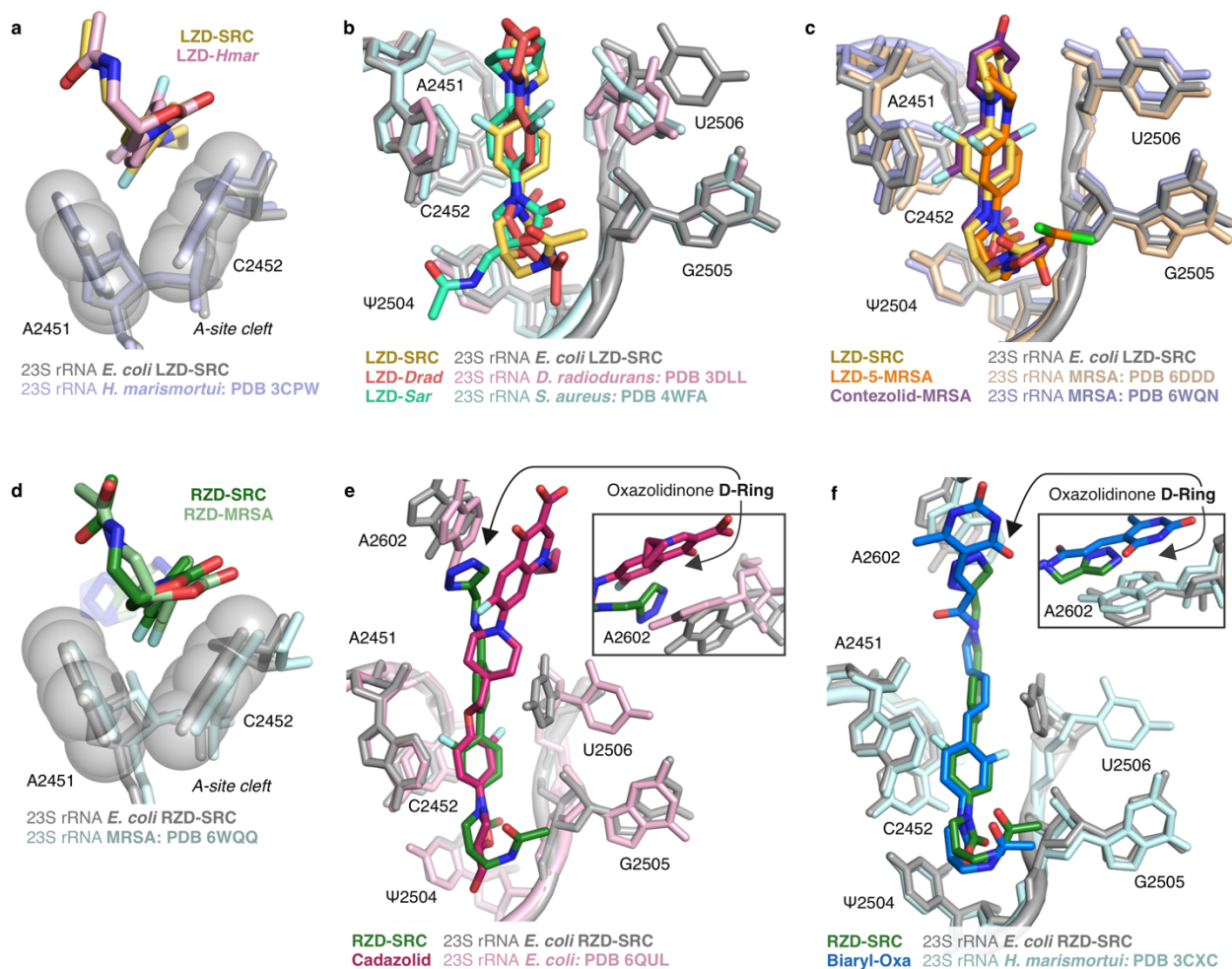


Figure 3.6 | Overview of linezolid and radezolid binding modes within the PTC . (a) Structural overlay of linezolid (LZD) bound to a *H. marismortui* ribosome (PDB: 3CPW) and linezolid-stalled *E. coli* ribosome complex (LZD-SRC), highlighting binding within the A-site cleft. (b) Overlay of *E. coli* LZD-SRC and LZD-only bound to a *D. radiodurans* (PDB: 3DLL) or *S. aureus* ribosome (PDB: 4WFA). (c) Overlay of *E. coli* LZD-SRC and MRSA ribosome bound to LZD analog (LZD-5, PDB: 6DDD) or contezolid (PDB: 6WQN). (d) Structural overlay of radezolid (RZD) bound to a MRSA ribosome (PDB: 6WQQ) and radezolid-stalled *E. coli* ribosome complex (RZD-SRC), highlighting the A-site cleft. (e) Overlay of *E. coli* RZD-SRC and *E. coli* ribosome bound to cadazolid (PDB: 6QUL). (f) Overlay of *E. coli* RZD-SRC and *H. marismortui* ribosome bound to a biaryl-oxazolidinone (PDB: 3CXC). Insets for panels (e) and (f) highlight the π -stacking interaction between the oxazolidinone D-ring and A2602. All overlays in this figure were generated by alignment of 23S rRNA nucleotides. *E. coli* numbering is used for all figure panels.

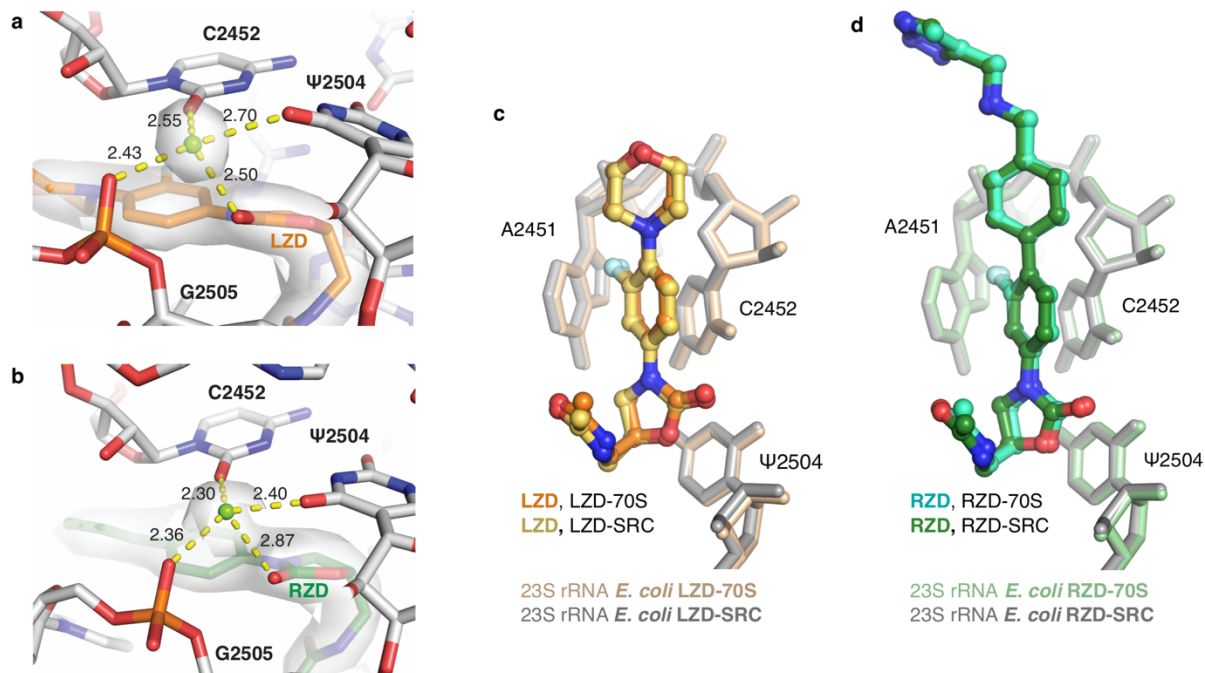


Figure 3.7 | Oxazolidinone binding modes in antibiotic-only and stalled complexes. (a) Coordination of a solvent molecule or ion to (a) linezolid (LZD) and surrounding nucleic acids in the linezolid-stalled *E. coli* ribosome complex (LZD-SRC). Coulomb potential is shown 1.5 Å from the ion and LZD ligand, contoured at 5σ in the unsharpened map, and coordination distances are shown in Ångstroms. (b) Coordination of a solvent molecule or ion to radezolid (RZD) and surrounding nucleic acids in the radezolid-stalled *E. coli* ribosome complex (RZD-SRC). Coulomb potential is shown 1.5 Å from the ion and RZD ligand, contoured at 5σ in the unsharpened map, and coordination distances are shown in Ångstroms. (c) Comparison of linezolid (LZD) binding modes in the antibiotic-only (LZD-70S, antibiotic in orange) versus LZD-stalled complex (LZD-SRC, antibiotic in yellow). (d) Comparison of radezolid (RZD) binding modes in the antibiotic-only (RZD-70S, antibiotic in teal) versus RZD-stalled complex (RZD-SRC, antibiotic in green). Structural overlays in this figure were performed by aligning the 23S rRNA chain.

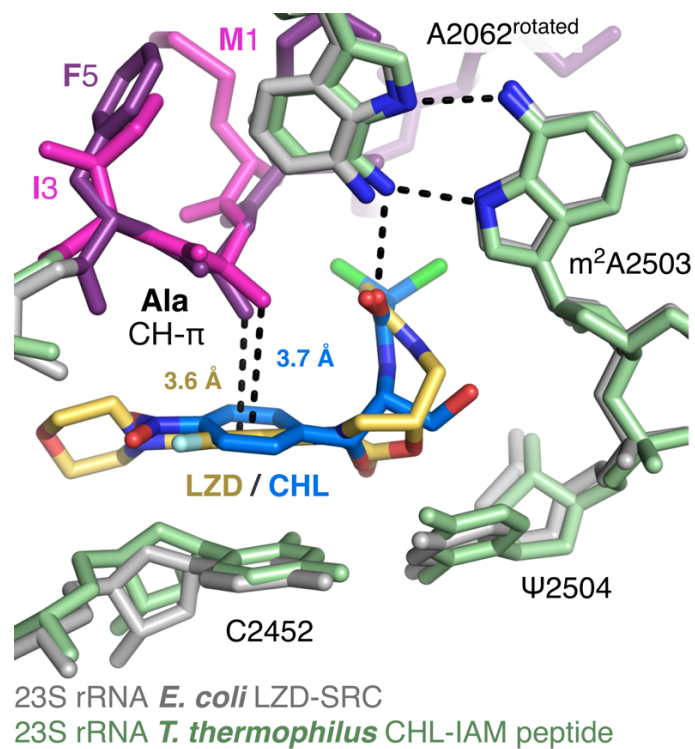


Figure 3.8 | Linezolid and chloramphenicol use the same interaction for context-specificity. Overlay was performed by alignment of 23S rRNA nucleotides 2000-3000, highlighting the CH- π interaction between the aryl ring of linezolid (LZD, yellow) or chloramphenicol (CHL, blue)²⁸ and the penultimate alanine side chain. Tri-peptide corresponding to the CHL complex is shown in pink, and the nascent chain from LZD-SRC is shown in purple. Labeling of 23S rRNA corresponds to *E. coli* numbering.

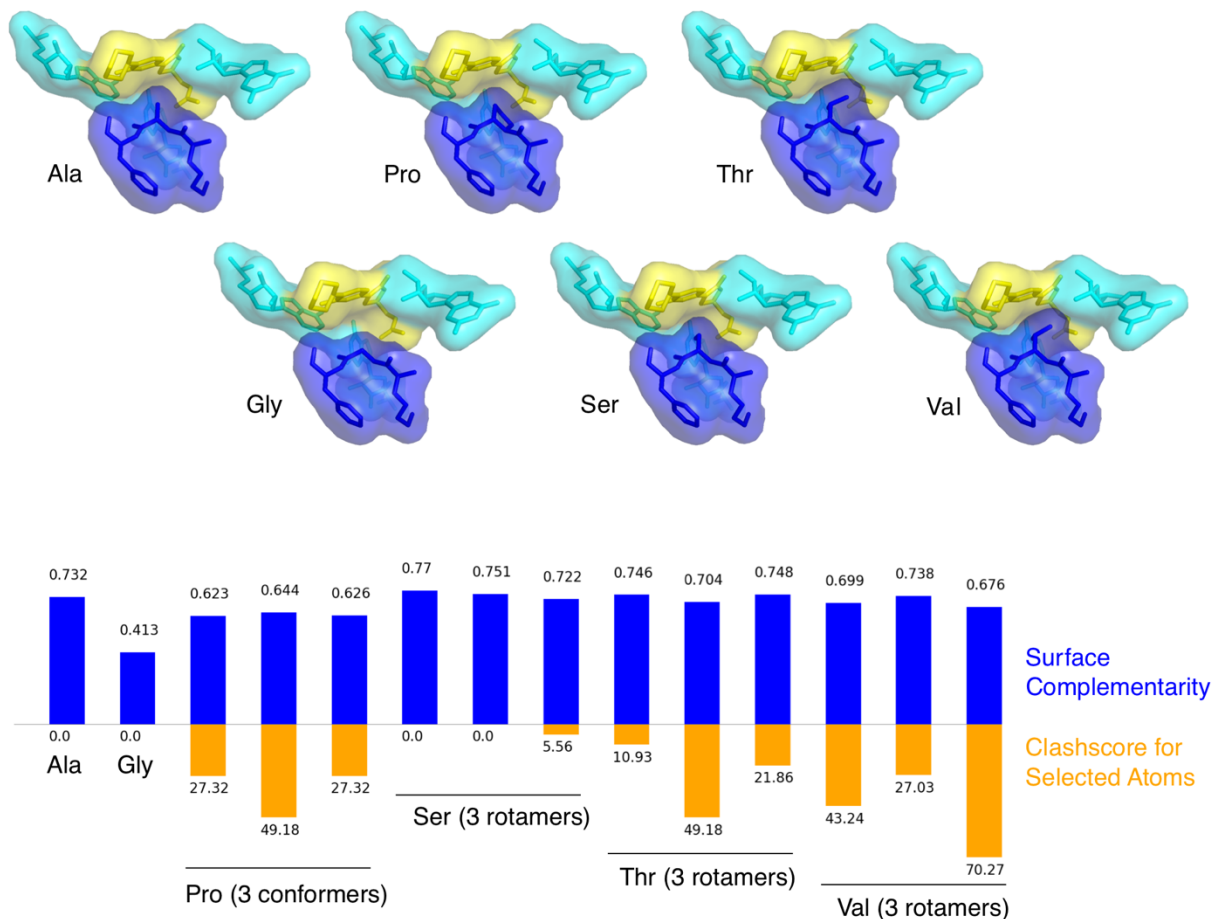


Figure 3.9 | In silico analysis of residues at the penultimate position. Substitution of glycine (Gly), proline (Pro), serine (Ser), threonine (Thr), or valine (Val) for alanine (Ala) at the penultimate position results in either reduced surface complementarity S_c as measured by the sc tool in CCP4⁶⁴ (blue bars) or increased clashscore (orange bars) in all cases except serine, which has two rotamers that slightly improve surface complementarity without clashing. Surface complementarity is calculated between two selections of atoms, the first of which is the sequence of three residues centered on the penultimate position, and the second of which is the linezolid ligand, and the three nucleotides close enough to potentially interact either favorably or unfavorably with the peptide sequence in the first selection. Surface complementarity is calculated without hydrogens modeled due to limitations of the CCP4 implementation. Alanine and serine are most highly favored for ligand binding by these metrics.

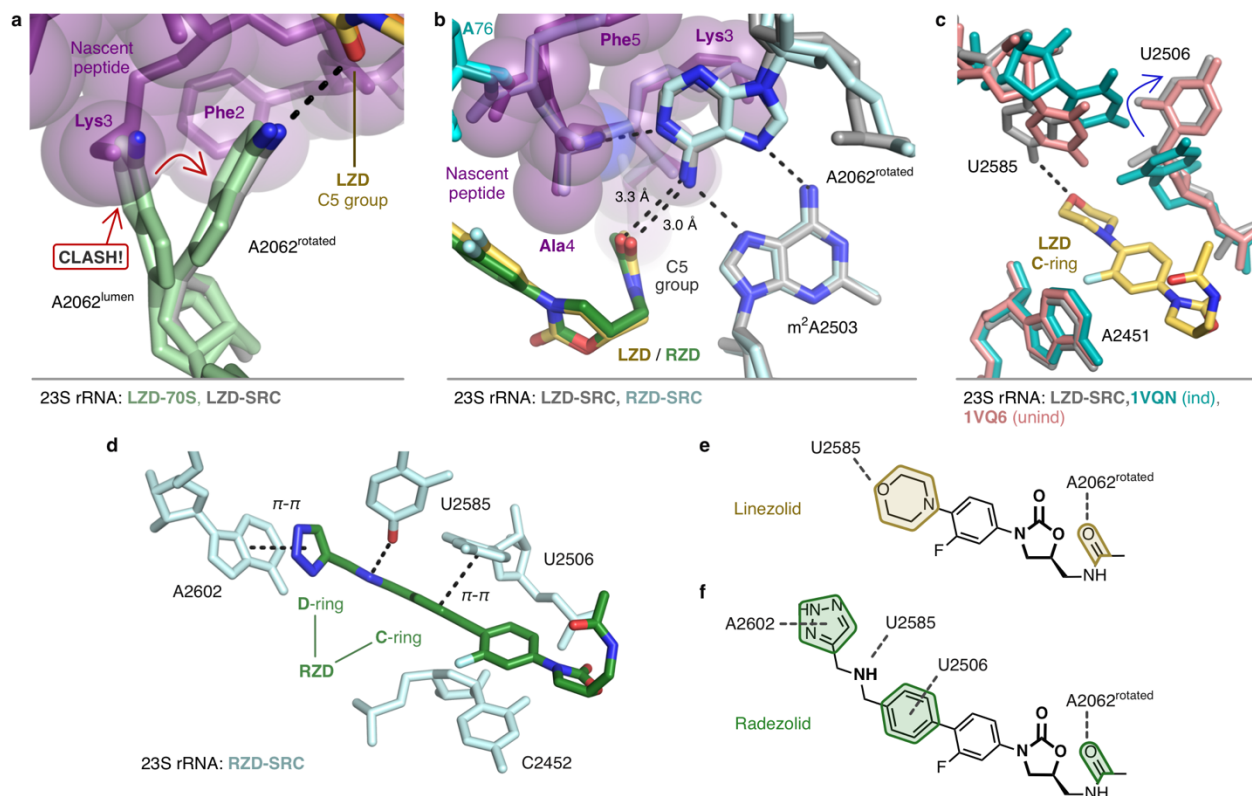


Figure 3.10 | Additional stabilization via interactions with rRNA nucleotides. (a) The rotated conformation of A2062 is adopted to accommodate the nascent chain (purple). (b) In the rotated state, A2062 makes H-bond interactions with the nascent chain (purple), m²A2503, and the C5 group of linezolid (LZD, yellow) and radezolid (RZD, green). (c) Additional interaction between U2585 and the morpholine ring of LZD (yellow). U2506 adopts a conformation consistent with the unaccommodated (unind, pink) state of the PTC³⁴. The accommodated PTC state (ind, teal) shown for comparison³⁴. Labeling of 23S rRNA corresponds to *E. coli* numbering. (d) Stabilized interactions between RZD and A2602, U2585, and U2506 observed in the stalled complex. (e), (f) Schematics of stabilized interactions for linezolid (panel e) and radezolid (panel f).

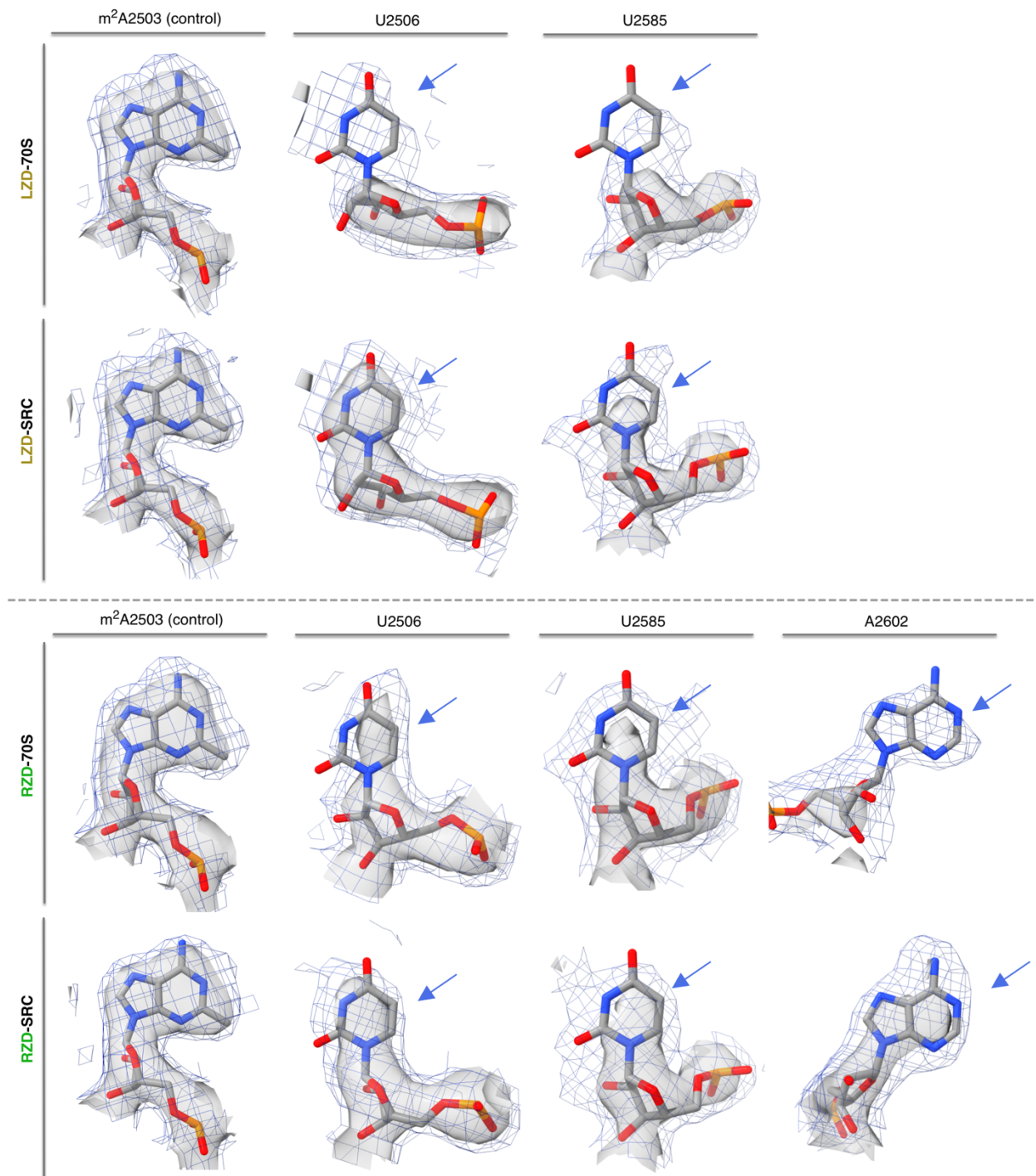


Figure 3.11 | Stabilization of PTC nucleotides. Direct comparison of nucleotide density in the linezolid-only bound (LZD-70S) and the linezolid-stalled complex (LZD-SRC), displaying m²A2503 as a control nucleotide and dynamic nucleotides U2506 and U2585. Direct comparison of nucleotide density in the radezolid-only bound (RZD-70S) and the radezolid-stalled complex (RZD-SRC), displaying A2503 and dynamic nucleotides U2506, U2585, A2602. Of note, U2506 is modeled in two conformations in LZD/RZD-70S; the relevant conformation for density comparison to SRCs is presented. Coulomb potential density is contoured at 4.0 σ in surface representation and 1.0 σ in mesh representation from unsharpened cryo-EM density maps.

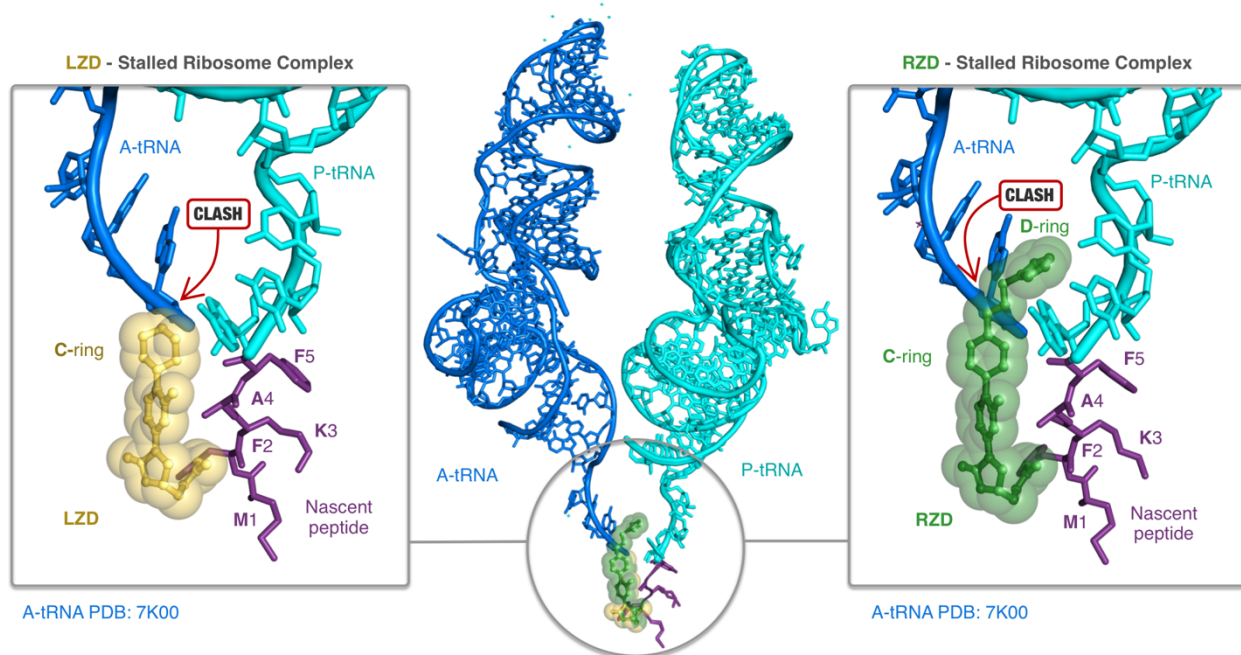


Figure 3.12 | Steric occlusion of A-site tRNA binding by oxazolidinone antibiotics. Linezolid (LZD, yellow) and radezolid (RZD, green) prevent binding of A-site tRNAs (blue, from PDB: 7K00). Prominent steric clashes between the A-tRNA and LZD C-ring and RZD C/D-ring are highlighted. Structural overlays were performed by alignment of 23S rRNA nucleotides.

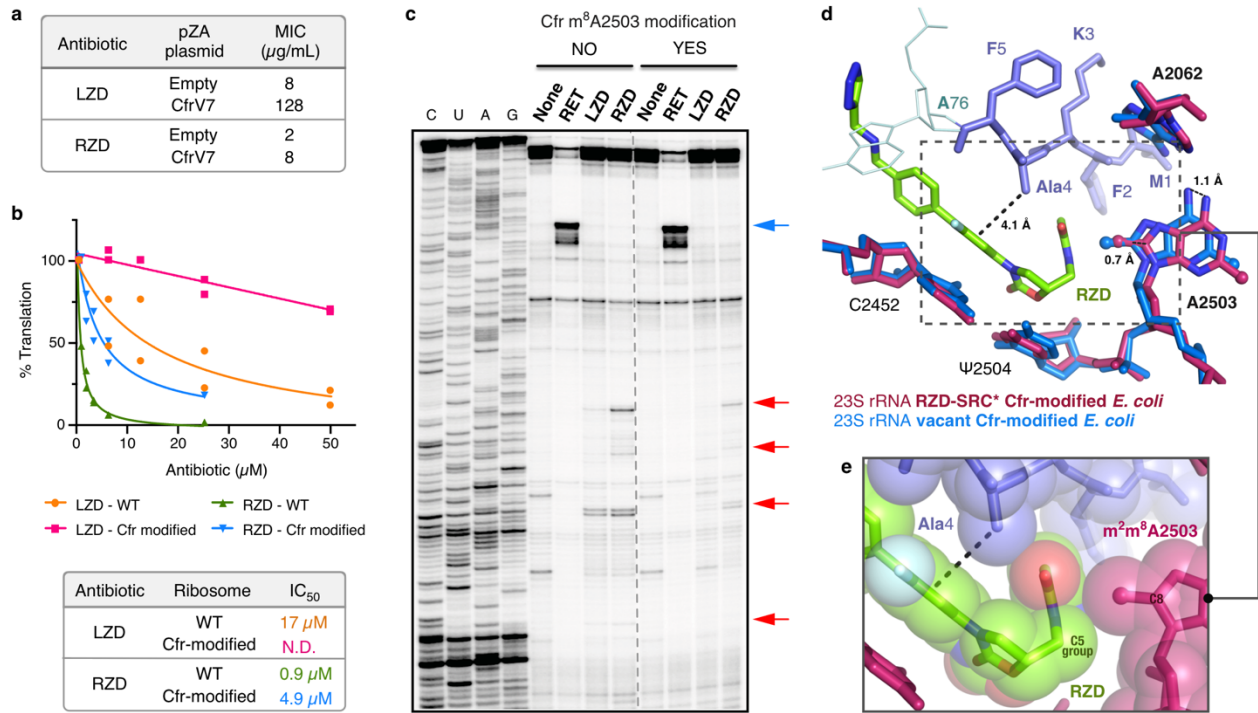


Figure 3.13 | LZD and RZD activity against Cfr-modified ribosomes. (a) Minimum inhibitory concentration of linezolid (LZD) and radezolid (RZD) required to inhibit growth of *E. coli* BW25113 *acrB::kan* transformed with either empty pZA plasmid or pZA encoding the evolved Cfr variant CfrV7, which achieves near-complete m^8A2503 methylation⁴³. MIC values were determined from two biological replicates. (b) *In vitro* activity of LZD and RZD against wildtype (WT) and Cfr-modified ribosomes determined by inhibition of sfGFP translation. Percent (%) translation calculated as the percentage of sfGFP translation at the tested antibiotic concentration compared to reactions containing no antibiotic determined from two independent experiments which are plotted as individual data points. N.D. indicates that the IC_{50} value was not determined. (c) Toeprinting analysis of LZD- and RZD-induced stalling of WT or Cfr-modified ribosomes within the 5' region of the sfGFP ORF. Drug-specific toeprint bands are indicated by red arrows. 'None' designates reactions lacking ribosome-targeting antibiotics. The control antibiotic retapamulin (RET) was used to stall ribosomes at the start codon indicated by the blue arrow⁶³. All antibiotics were added to a final concentration of 50 μM . Toeprinting experiments were performed at least twice with similar results. (d) Overlay of a vacant Cfr-modified *E. coli* ribosome⁴³ with the RZD-stalled, Cfr-modified *E. coli* ribosome performed by alignment of 23S rRNA nucleotides 2000-3000. (e) Close-up view of the penultimate alanine, RZD, and C8-methylated A2503 in sphere representation.

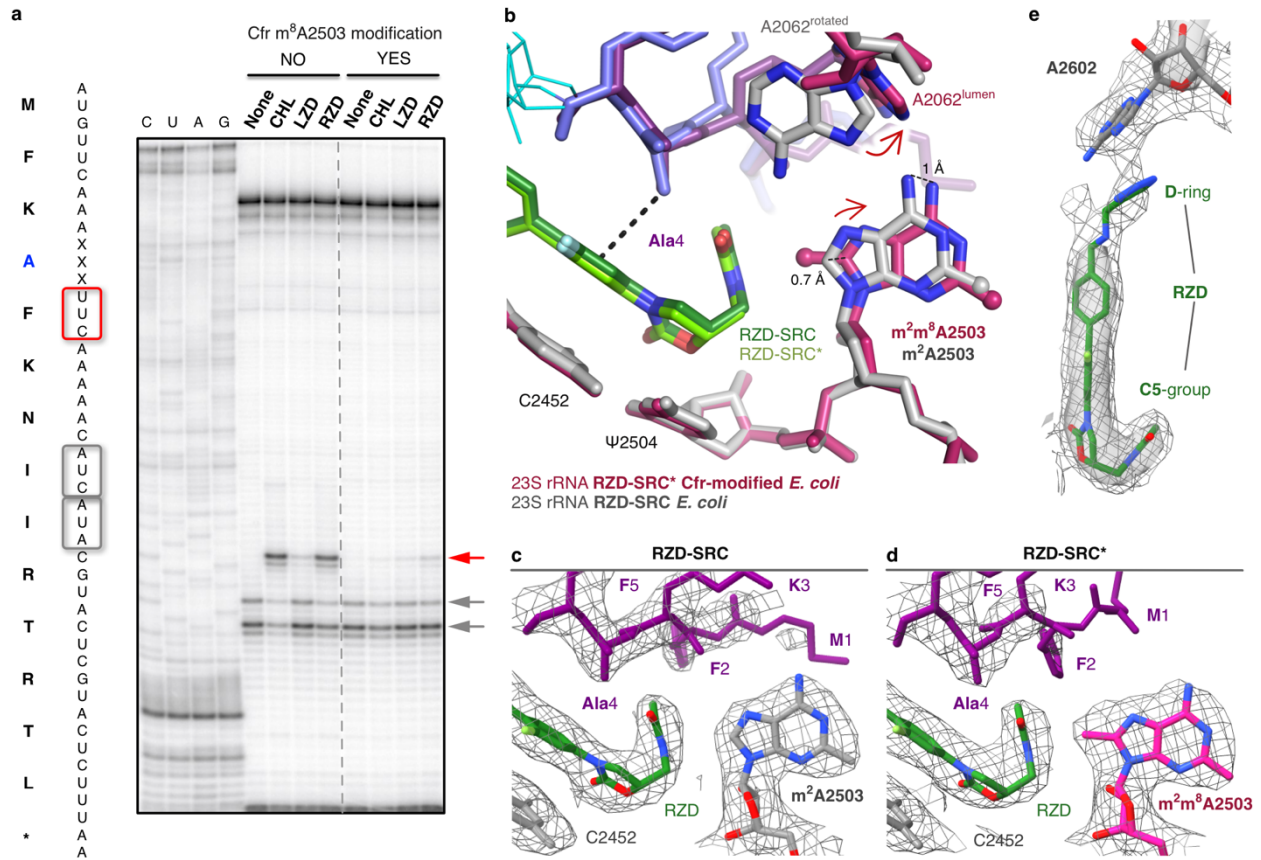


Figure 3.14 | The Cfr modification reduces radezolid-dependent ribosome stalling. (a) Toeprinting assays performed on the MFKAF stalling peptide sequence. Prominent stall sites observed in reactions containing chloramphenicol (CHL), linezolid (LZD), or radezolid (RZD) with WT ribosomes, but not with Cfr-modified ribosomes, are indicated by the red arrow. ‘None’ designates reactions lacking ribosome-targeting antibiotics. Due to the inclusion of the tRNA synthetase inhibitor mupirocin in all toeprinting reactions, any ribosomes not stalled at an upstream codon are forced to stall at the Ile codons designated by grey arrows. All antibiotics were added to a final concentration of 50 μ M. Toeprinting experiments were performed at least twice with similar results. (b) Structural rearrangements identified in the RZD-stalled complex with a Cfr-modified ribosome. Overlay was performed by alignment of 23S rRNA nucleotides 2000-3000. Coulomb potential density for A2503, RZD and nascent chain contoured at 3.0σ for (c) RZD stalled with WT ribosome (RZD-SRC) and (d) RZD-stalled with Cfr-modified ribosome (RZD-SRC*). (e) Retained interaction between the RZD D-ring and A2602 in the Cfr-modified ribosome. Coulomb potential density is contoured at 4.0σ in surface representation and 1.0σ in mesh representation. Figure panels (c)-(e) were prepared using unsharpened cryo-EM density maps.

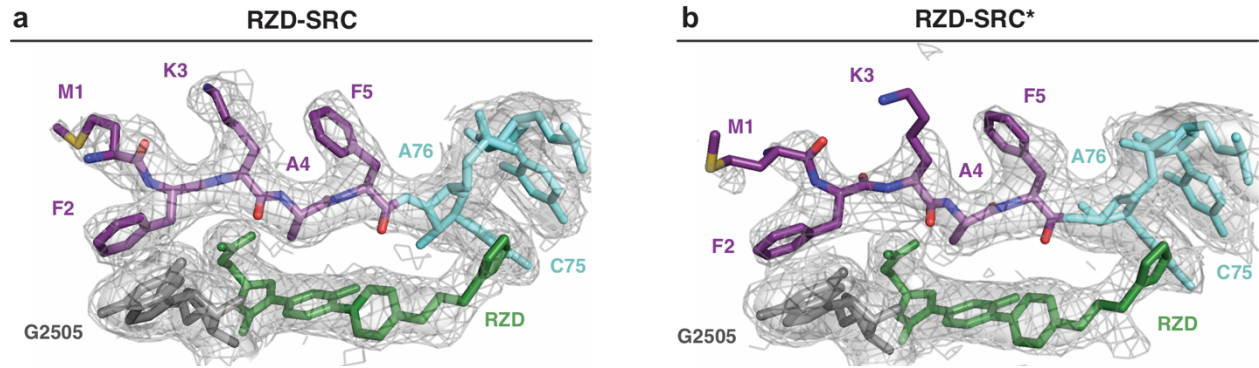


Figure 3.15 | Density for the nascent chain in RZD-stalled ribosome complexes. Density comparison for the alanine-containing MFKAF nascent peptide (purple) between RZD-stalled complexes with (a) WT and (b) Cfr-modified ribosome. RZD shown in green and G2505 shown in grey. Coulomb potential density is contoured at 4.0σ in surface representation and 1.0σ in mesh representation from unsharpened cryo-EM density maps and carved at 1.8 Ångstroms from the part of the model shown.

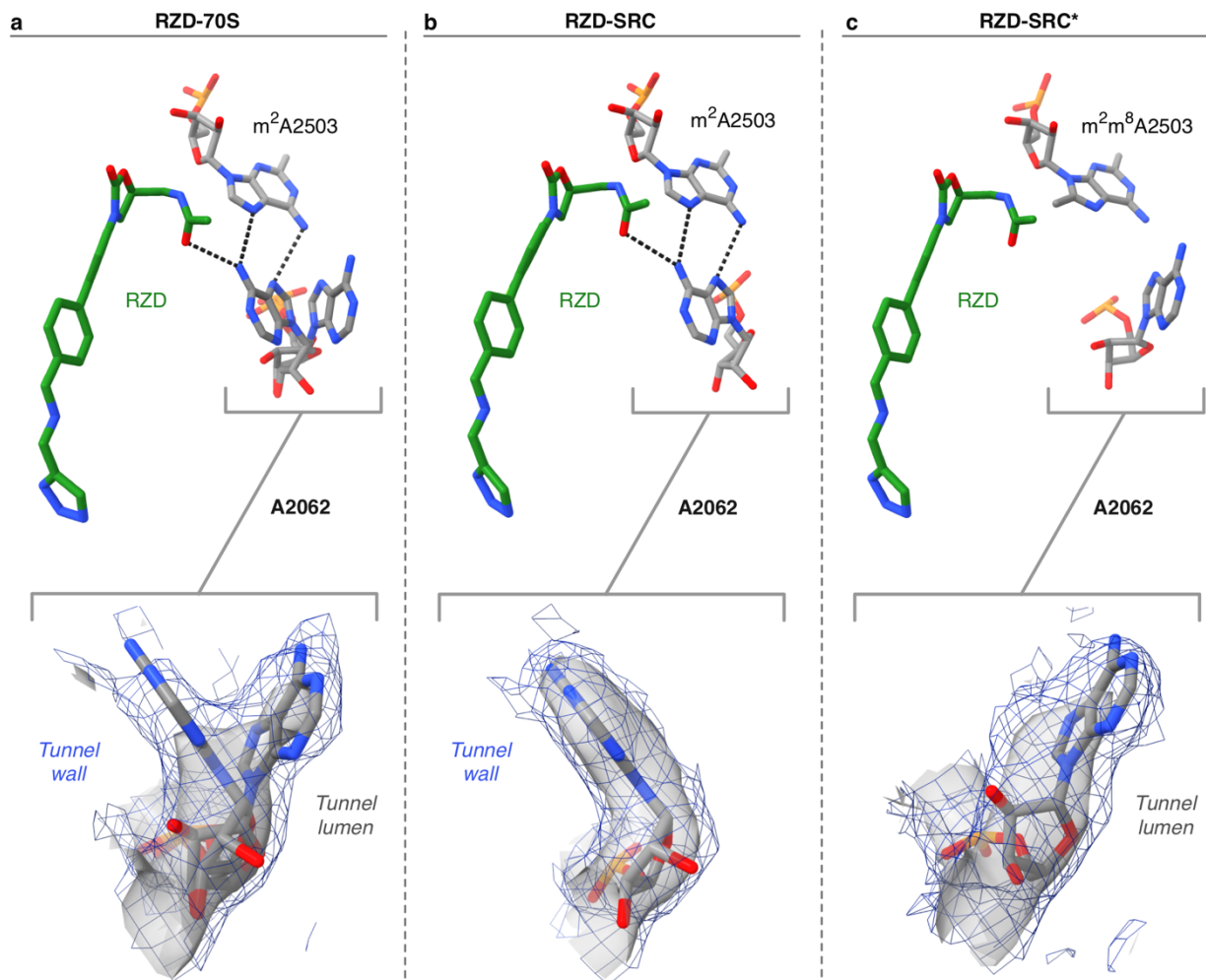


Figure 3.16 | A2062 conformations in the RZD-bound ribosome structures. (a) A2062 adopts both the lumen and the rotated, tunnel wall conformation in the RZD-only bound ribosome. In the rotated wall conformation, A2062 engages in H-bonding interactions with A2503 and RZD. (b) A2062 is only observed in the rotated conformation to H-bond with A2503 and RZD in the WT stalled complex. (c) A2062 is observed in the lumen conformation in the RZD-stalled complex with a Cfr-modified ribosome. Coulomb potential density is contoured at 4.0σ in surface representation and 1.0σ in mesh representation from unsharpened cryo-EM density maps.

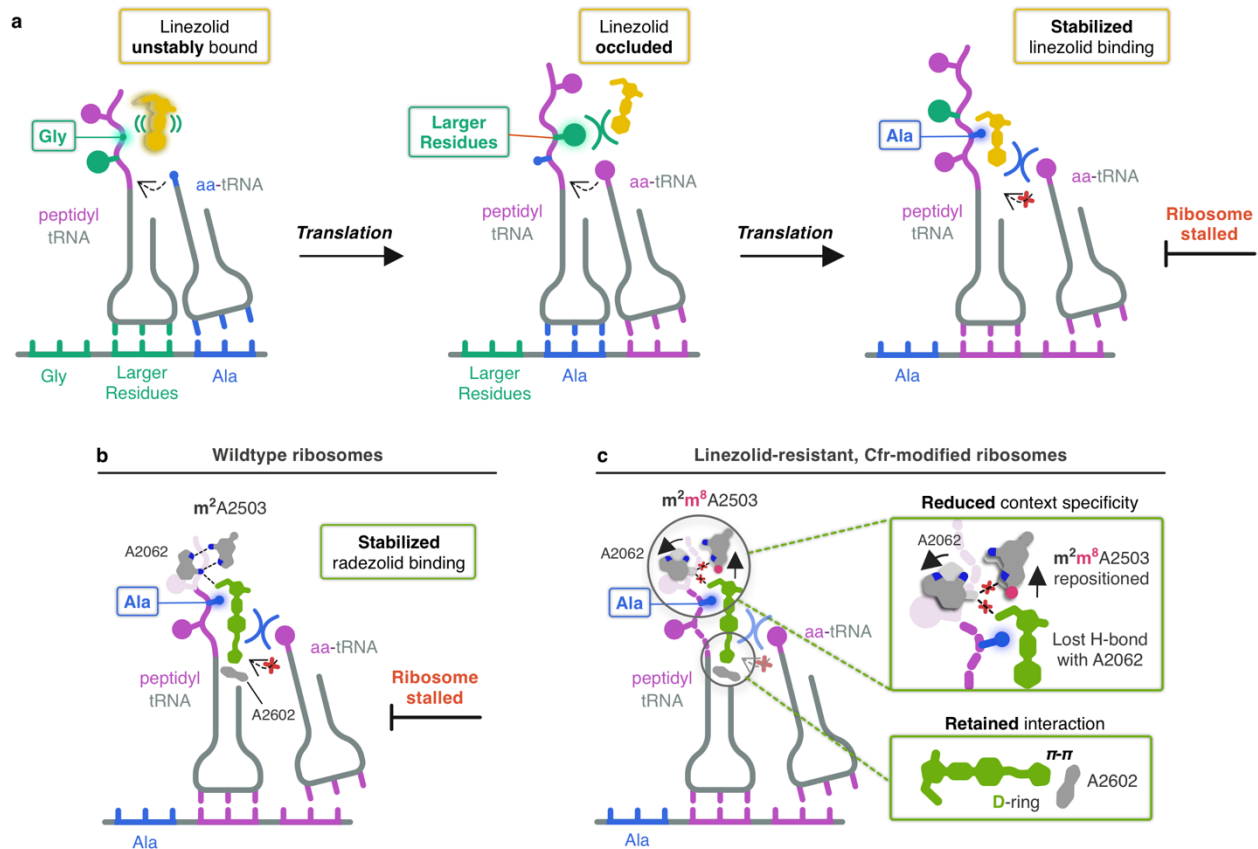


Figure 3.17 | Model for oxazolidinone context-specific inhibition of translation. (a) Linezolid (yellow) is either unstably bound or sterically occluded from binding to the ribosome when glycine (Gly) or larger residues occupy the penultimate position within the nascent chain. When alanine (Ala, blue) occupies the penultimate position, linezolid becomes stably bound to the ribosomal PTC A-site, enabling linezolid to better compete away incoming aminoacyl tRNAs (aa-tRNAs) and resulting in ribosome stalling. (b) Radezolid (green) also facilitates stalling of ribosomes with alanine in the penultimate position by enhancing radezolid binding to the PTC A-site. (c) Radezolid context-specificity is diminished with Cfr-modified ribosomes due to repositioning of C8-methylated A2503 (pink circle) and the lost interaction with A2062. Retained interaction between radezolid D-ring and A2602 provides rationale for why RZD can overcome Cfr-mediated resistance.

Table 3.1 | Cryo-EM data collection and statistics

Structure Name	LZD-SRC	LZD-70S	RZD-SRC	RZD-70S	RZD-SRC*
PDB	PDB: 7S1G	PDB: 7S1H	PDB: 7S1I	PDB: 7S1J	PDB: 7S1K
EMDB	EMDB: 24800	EMDB: 24801	EMDB: 24802	EMDB: 24803	EMDB: 24804
Data collection and processing					
Facility and Electron microscope	S ² C ² Titan Krios	S ² C ² Titan Krios	NCCAT Titan Krios	NCCAT Titan Krios	UCSF Titan Krios
Voltage (kV)	300	300	300	300	300
Camera	Gatan K3	Gatan K3	Gatan K2 Summit	Gatan K2 Summit	Gatan K3
Nominal Magnification	29,000	29,000	105,000	105,000	105,000
Electron dose (e-/Å ²)	67.8	67.8	52.8	52.8	69.0
Defocus range (µm)	0.3-0.8	0.3-0.8	0.5-1.5	0.5-1.5	0.3-0.8
Pixel size (Å)	0.8125	0.8125	0.8250	0.8250	0.8261
Energy filter slit width (eV)	n/a	n/a	20	20	20
Symmetry imposed	C1	C1	C1	C1	C1
Number of total micrographs	3644	3066	3566	1925	2211
Number of good micrographs	3004	2954	3534	1902	2141
Number of particles picked from good micrographs	332502	441587	292882	179529	369975
Number of particles used in final reconstruction	176779	360239	240596	146245	276799
Map refinement					
Model resolution (Å)	2.48	2.35	2.48	2.47	2.42
FSC threshold	0.143	0.143	0.143	0.143	0.143
Map sharpening B-factor (Å ²)	0.0	0.0	0.0	0.0	0.0
Refinement and model statistics					
Model composition					
Total atoms	240937	238267	240938	238218	240967
Hydrogens only	96780	95859	96769	95822	96780
Non-hydrogen atoms	144157	142408	144169	142396	144187
Protein residues	5661	5656	5661	5656	5661
Nucleotide residues	4638	4556	4638	4556	4638
Ligands	199	209	212	202	210
Clashscore, all atoms	3.64	4.63	4.32	5.58	5.46
Protein geometry					
MolProbity score	1.24	1.31	1.28	1.62	1.42
Rotamer outliers (%)	0.80	0.99	0.95	1.77	0.89
Cβ deviations >0.25 Å (%)	0.00	0.00	0.00	0.00	0.04
Ramachandran (%)					
- Favored	97.57	97.64	97.68	97.33	97.32
- Allowed	2.36	2.29	2.25	2.61	2.61
- Outliers	0.07	0.07	0.07	0.05	0.07
Nucleic acid geometry					
Probably wrong sugar pucker	0%	0%	0%	0%	0%
Bad backbone conformations	11%	11%	11%	11%	12%
Deviations from ideal geometry					
- Bonds (%)	0.002	0.002	0.002	0.002	0.003
- Angles (%)	0.345	0.362	0.366	0.387	0.382
EM Ringer Score	3.21	3.34	3.68	2.53	2.97

Table 3.2 | Primer sequences used in this study. Oligonucleotides were purchased from Integrated DNA Technologies and prepared with standard desalting procedures.

Primer name	Sequence
T7	5'-ATTAATACGACTCACTATAGG-3'
ORF_SD	5'-GAATGCTTTGAACATTTTTATTTCC-3'
T7_MFKAF _Fwd	5'-ATTAATACGACTCACTATAGGGCAACCTAAACTTACACACGCCCCG-3'
SD_MFKAF _Rev	5'-GAATGCTTTGAACATTTTTATTTCTTACCGGGCGTGTGTAAGTTTTAG-3'

References

1. Wilson, D. N. Ribosome-targeting antibiotics and mechanisms of bacterial resistance. *Nat. Rev. Microbiol.* **12**, 35–48 (2014).
2. Polacek, N. & Mankin, A. S. The Ribosomal Peptidyl Transferase Center: Structure, Function, Evolution, Inhibition. *Critical Reviews in Biochemistry and Molecular Biology* vol. 40 285–311 (2005).
3. Stevens, D. L., Dotter, B. & Madaras-Kelly, K. A review of linezolid: the first oxazolidinone antibiotic. *Expert Rev. Anti. Infect. Ther.* **2**, 51–59 (2004).
4. Birmingham, M. C. *et al.* Linezolid for the treatment of multidrug-resistant, gram-positive infections: experience from a compassionate-use program. *Clin. Infect. Dis.* **36**, 159–168 (2003).
5. Colca, J. R. *et al.* Cross-linking in the living cell locates the site of action of oxazolidinone antibiotics. *J. Biol. Chem.* **278**, 21972–21979 (2003).
6. Leach, K. L. *et al.* The site of action of oxazolidinone antibiotics in living bacteria and in human mitochondria. *Mol. Cell* **26**, 393–402 (2007).
7. Eyal, Z. *et al.* Structural insights into species-specific features of the ribosome from the pathogen *Staphylococcus aureus*. *Proc. Natl. Acad. Sci. U. S. A.* **112**, E5805–14 (2015).
8. Wilson, D. N. *et al.* The oxazolidinone antibiotics perturb the ribosomal peptidyl-transferase center and effect tRNA positioning. *Proc. Natl. Acad. Sci. U. S. A.* **105**, 13339–13344 (2008).
9. Ippolito, J. A. *et al.* Crystal structure of the oxazolidinone antibiotic linezolid bound to the 50S ribosomal subunit. *J. Med. Chem.* **51**, 3353–3356 (2008).
10. Marks, J. *et al.* Context-specific inhibition of translation by ribosomal antibiotics targeting the peptidyl transferase center. *Proc. Natl. Acad. Sci. U. S. A.* **113**, 12150–12155 (2016).

11. Choi, J. *et al.* Dynamics of the context-specific translation arrest by chloramphenicol and linezolid. *Nat. Chem. Biol.* **16**, 310–317 (2020).
12. Long, K. S. & Vester, B. Resistance to linezolid caused by modifications at its binding site on the ribosome. *Antimicrob. Agents Chemother.* **56**, 603–612 (2012).
13. Belousoff, M. J. *et al.* Structural Basis for Linezolid Binding Site Rearrangement in the *Staphylococcus aureus* Ribosome. *MBio* **8**, (2017).
14. Wilson, D. N., Hauryliuk, V., Atkinson, G. C. & O’Neill, A. J. Target protection as a key antibiotic resistance mechanism. *Nat. Rev. Microbiol.* **18**, 637–648 (2020).
15. Kehrenberg, C., Schwarz, S., Jacobsen, L., Hansen, L. H. & Vester, B. A new mechanism for chloramphenicol, florfenicol and clindamycin resistance: methylation of 23S ribosomal RNA at A2503. *Molecular Microbiology* vol. 57 1064–1073 (2005).
16. Long, K. S., Poehlsgaard, J., Kehrenberg, C., Schwarz, S. & Vester, B. The Cfr rRNA methyltransferase confers resistance to Phenicol, Lincosamides, Oxazolidinones, Pleuromutilins, and Streptogramin A antibiotics. *Antimicrob. Agents Chemother.* **50**, 2500–2505 (2006).
17. Giessing, A. M. B. *et al.* Identification of 8-methyladenosine as the modification catalyzed by the radical SAM methyltransferase Cfr that confers antibiotic resistance in bacteria. *RNA* **15**, 327–336 (2009).
18. Pandit, N., Singla, R. K. & Shrivastava, B. Current updates on oxazolidinone and its significance. *Int J Med Chem* **2012**, 159285 (2012).
19. Shaw, K. J. & Barbachyn, M. R. The oxazolidinones: past, present, and future. *Ann. N. Y. Acad. Sci.* **1241**, 48–70 (2011).
20. Swaney, S. M., Aoki, H., Ganoza, M. C. & Shinabarger, D. L. The oxazolidinone linezolid

- inhibits initiation of protein synthesis in bacteria. *Antimicrob. Agents Chemother.* **42**, 3251–3255 (1998).
21. Grant, T., Rohou, A. & Grigorieff, N. cisTEM, user-friendly software for single-particle image processing. *eLife* vol. 7 (2018).
 22. Wright, A. *et al.* Characterization of the Core Ribosomal Binding Region for the Oxazolidone Family of Antibiotics Using Cryo-EM. *ACS Pharmacol. Transl. Sci.* (2020) doi:10.1021/acspsci.0c00041.
 23. Zhou, J. *et al.* Design at the atomic level: design of biaryloxazolidinones as potent orally active antibiotics. *Bioorg. Med. Chem. Lett.* **18**, 6175–6178 (2008).
 24. Scaiola, A. *et al.* Structural basis of translation inhibition by cadazolid, a novel quinoxolidinone antibiotic. *Sci. Rep.* **9**, 5634 (2019).
 25. Yang, K. *et al.* Structural insights into species-specific features of the ribosome from the human pathogen *Mycobacterium tuberculosis*. *Nucleic Acids Res.* **45**, 10884–10894 (2017).
 26. Belousoff, M. J. *et al.* CryoEM-guided development of antibiotics for drug-resistant bacteria. *ChemMedChem* **14**, 527–531 (2019).
 27. Renslo, A. R., Luehr, G. W. & Gordeev, M. F. Recent developments in the identification of novel oxazolidinone antibacterial agents. *Bioorg. Med. Chem.* **14**, 4227–4240 (2006).
 28. Syroegin, E. A. *et al.* Structural basis for the context-specific action of classic peptidyl transferase inhibitors. *bioRxiv* 2021.06.17.448903 (2021) doi:10.1101/2021.06.17.448903.
 29. Vázquez-Laslop, N., Ramu, H., Klepacki, D., Kannan, K. & Mankin, A. S. The key function of a conserved and modified rRNA residue in the ribosomal response to the nascent peptide. *EMBO J.* **29**, 3108–3117 (2010).
 30. Arenz, S. *et al.* Drug sensing by the ribosome induces translational arrest via active site

- perturbation. *Mol. Cell* **56**, 446–452 (2014).
31. Koch, M., Willi, J., Pradère, U., Hall, J. & Polacek, N. Critical 23S rRNA interactions for macrolide-dependent ribosome stalling on the ErmCL nascent peptide chain. *Nucleic Acids Res.* **45**, 6717–6728 (2017).
 32. Li, W., Chang, S. T.-L., Ward, F. R. & Cate, J. H. D. Selective inhibition of human translation termination by a drug-like compound. *Nat. Commun.* **11**, 4941 (2020).
 33. Svetlov, M. S. *et al.* High-resolution crystal structures of ribosome-bound chloramphenicol and erythromycin provide the ultimate basis for their competition. *RNA* **25**, 600–606 (2019).
 34. Schmeing, T. M., Huang, K. S., Strobel, S. A. & Steitz, T. A. An induced-fit mechanism to promote peptide bond formation and exclude hydrolysis of peptidyl-tRNA. *Nature* **438**, 520–524 (2005).
 35. Toh, S.-M. *et al.* Acquisition of a natural resistance gene renders a clinical strain of methicillin-resistant *Staphylococcus aureus* resistant to the synthetic antibiotic linezolid. *Mol. Microbiol.* **64**, 1506–1514 (2007).
 36. Bonilla, H. *et al.* Multicity outbreak of linezolid-resistant *Staphylococcus epidermidis* associated with clonal spread of a *cfr*-containing strain. *Clin. Infect. Dis.* **51**, 796–800 (2010).
 37. Morales, G. *et al.* Resistance to linezolid is mediated by the *cfr* gene in the first report of an outbreak of linezolid-resistant *Staphylococcus aureus*. *Clin. Infect. Dis.* **50**, 821–825 (2010).
 38. Baos, E., Candel, F. J., Merino, P., Pena, I. & Picazo, J. J. Characterization and monitoring of linezolid-resistant clinical isolates of *Staphylococcus epidermidis* in an intensive care unit 4 years after an outbreak of infection by *cfr*-mediated linezolid-resistant *Staphylococcus aureus*. *Diagn. Microbiol. Infect. Dis.* **76**, 325–329 (2013).

39. Locke, J. B. *et al.* Linezolid-resistant *Staphylococcus aureus* strain 1128105, the first known clinical isolate possessing the *cfr* multidrug resistance gene. *Antimicrob. Agents Chemother.* **58**, 6592–6598 (2014).
40. Dortet, L. *et al.* Long-lasting successful dissemination of resistance to oxazolidinones in MDR *Staphylococcus epidermidis* clinical isolates in a tertiary care hospital in France. *J. Antimicrob. Chemother.* **73**, 41–51 (2018).
41. Yan, F. *et al.* RlmN and Cfr are radical SAM enzymes involved in methylation of ribosomal RNA. *J. Am. Chem. Soc.* **132**, 3953–3964 (2010).
42. Yan, F. & Fujimori, D. G. RNA methylation by radical SAM enzymes RlmN and Cfr proceeds via methylene transfer and hydride shift. *Proc. Natl. Acad. Sci. U. S. A.* **108**, 3930–3934 (2011).
43. Tsai, K. *et al.* Directed evolution of the rRNA methylating enzyme Cfr reveals molecular basis of antibiotic resistance. *bioRxiv* 2021.03.12.435202 (2021)
doi:10.1101/2021.03.12.435202.
44. Lawrence, L., Danese, P., DeVito, J., Franceschi, F. & Sutcliffe, J. In vitro activities of the Rx-01 oxazolidinones against hospital and community pathogens. *Antimicrob. Agents Chemother.* **52**, 1653–1662 (2008).
45. Locke, J. B. *et al.* Structure-activity relationships of diverse oxazolidinones for linezolid-resistant *Staphylococcus aureus* strains possessing the *cfr* methyltransferase gene or ribosomal mutations. *Antimicrob. Agents Chemother.* **54**, 5337–5343 (2010).
46. Shaw, K. J. *et al.* In vitro activity of TR-700, the antibacterial moiety of the prodrug TR-701, against linezolid-resistant strains. *Antimicrob. Agents Chemother.* **52**, 4442–4447 (2008).

47. Zhanel, G. G. *et al.* Tedizolid: a novel oxazolidinone with potent activity against multidrug-resistant gram-positive pathogens. *Drugs* **75**, 253–270 (2015).
48. Svetlov, M. S. *et al.* Context-specific action of macrolide antibiotics on the eukaryotic ribosome. *Nat. Commun.* **12**, 2803 (2021).
49. Vazquez-Laslop, N., Thum, C. & Mankin, A. S. Molecular mechanism of drug-dependent ribosome stalling. *Mol. Cell* **30**, 190–202 (2008).
50. Li, W. *et al.* Structural basis for selective stalling of human ribosome nascent chain complexes by a drug-like molecule. *Nat. Struct. Mol. Biol.* **26**, 501–509 (2019).
51. Stojković, V. *et al.* Assessment of the nucleotide modifications in the high-resolution cryo-electron microscopy structure of the Escherichia coli 50S subunit. *Nucleic Acids Res.* **48**, 2723–2732 (2020).
52. Wiegand, I., Hilpert, K. & Hancock, R. E. W. Agar and broth dilution methods to determine the minimal inhibitory concentration (MIC) of antimicrobial substances. *Nat. Protoc.* **3**, 163–175 (2008).
53. Orelle, C. *et al.* Identifying the targets of aminoacyl-tRNA synthetase inhibitors by primer extension inhibition. *Nucleic Acids Res.* **41**, e144 (2013).
54. Ohashi, H., Kanamori, T., Osada, E., Akbar, B. K. & Ueda, T. Peptide screening using PURE ribosome display. *Methods Mol. Biol.* **805**, 251–259 (2012).
55. Bundy, B. C. & Swartz, J. R. Site-Specific Incorporation of p-Propargyloxyphenylalanine in a Cell-Free Environment for Direct Protein–Protein Click Conjugation. *Bioconjug. Chem.* **21**, 255–263 (2010).
56. Zheng, S. Q. *et al.* MotionCor2: anisotropic correction of beam-induced motion for improved cryo-electron microscopy. *Nat. Methods* **14**, 331–332 (2017).

57. Emsley, P., Lohkamp, B., Scott, W. G. & Cowtan, K. Features and development of Coot. *Acta Crystallographica Section D Biological Crystallography* vol. 66 486–501 (2010).
58. Croll, T. I. ISOLDE: a physically realistic environment for model building into low-resolution electron-density maps. *Acta Crystallogr D Struct Biol* **74**, 519–530 (2018).
59. Adams, P. D. *et al.* PHENIX: a comprehensive Python-based system for macromolecular structure solution. *Acta Crystallogr. D Biol. Crystallogr.* **66**, 213–221 (2010).
60. Arenz, S. *et al.* A combined cryo-EM and molecular dynamics approach reveals the mechanism of ErmBL-mediated translation arrest. *Nature Communications* vol. 7 (2016).
61. Moriarty, N. W., Grosse-Kunstleve, R. W. & Adams, P. D. electronic Ligand Builder and Optimization Workbench (eLBOW): a tool for ligand coordinate and restraint generation. *Acta Crystallogr. D Biol. Crystallogr.* **65**, 1074–1080 (2009).
62. Pettersen, E. F. *et al.* UCSF ChimeraX: Structure visualization for researchers, educators, and developers. *Protein Sci.* **30**, 70–82 (2021).
63. Meydan, S. *et al.* Retapamulin-Assisted Ribosome Profiling Reveals the Alternative Bacterial Proteome. *Mol. Cell* **74**, 481–493.e6 (2019).
64. Collaborative Computational Project, Number 4. The CCP4 suite: programs for protein crystallography. *Acta Crystallogr. D Biol. Crystallogr.* **50**, 760–763 (1994).

Publishing Agreement

It is the policy of the University to encourage open access and broad distribution of all theses, dissertations, and manuscripts. The Graduate Division will facilitate the distribution of UCSF theses, dissertations, and manuscripts to the UCSF Library for open access and distribution. UCSF will make such theses, dissertations, and manuscripts accessible to the public and will take reasonable steps to preserve these works in perpetuity.

I hereby grant the non-exclusive, perpetual right to The Regents of the University of California to reproduce, publicly display, distribute, preserve, and publish copies of my thesis, dissertation, or manuscript in any form or media, now existing or later derived, including access online for teaching, research, and public service purposes.

DocuSigned by:

Mary Kaitlyn Tsai

DDDC667623714AD...

Author Signature

11/29/2021

Date